Università degli Studi di Cagliari

PHD DEGREE

Physics

Cycle XXXII

Impregnation of porous silicon matrices for technological applications

Scientific Disciplinary Sector(s)

FIS/01

PhD Student — Elisa Pinna

Coordinator of the PhD Programme — Prof. Paolo Ruggerone

Supervisor — Dott. Guido Mula

Final exam. Academic Year 2018 – 2019
Thesis defence: January-February 2020 Session

To myself and who was, is and always will be by my side.

Elisa Pinna gratefully acknowledges Sardinian Regional Government for the financial support of her PhD scholarship (P.O.R. Sardegna F.S.E. - Operational Programme of the Autonomous Region of Sardinia, European Social Fund 2014-2020 - Axis III Education and training, Thematic goal 10, Investment Priority 10ii), Specific goal 10.5.

Abstract

This PhD thesis presents a study of the filling of porous silicon matrices and has been done prevalently in the laboratory *PoroSiLab*, of the Department of Physics of the University of Cagliari.

Porous silicon (PSi) is a very versatile material, whose main feature is the large developed surface. This inner surface, generated by the presence of pores, makes PSi particularly suitable for applications needing pores impregnation. In this way, many new different systems can be formed, and their characteristics can be exploited for several technological applications. PSi, beneath its complex nature, is very attractive in many different technological fields, from energy storage and production, sensors and optoelectronic devices and biomedical applications. Many research efforts have been done for the optimization of these kind of devices, including the optimization of pores impregnation mechanisms, aiming at the improvement of the performances of the final structures.

In this PhD thesis I will report a study on the impregnation of PSi with different materials for a variety of technological applications. In particular, the impregnation process has been studied for organic and inorganic materials, with the aim of optimizing the process and, as a consequence, the samples properties.

In the first part of this study, the chemical impregnation of the PSi matrix with melanin will be presented. After a brief introduction on the past discoveries on the hybrid junction, I will present the results in the understanding of the mechanisms governing the penetration of melanin starting monomers and their polymerization into melanin, together with the improvement we achieved in increasing the lifetime of the hybrid structure in terms of production of photogenerated current. I will also present the results obtained using a different PSi matrix, that is a porous structure obtained by using metal-assisted chemical etching (MACE). The MACE approach has been used to limit the high Si reflectivity by a suitable surface structurations. The impregnation of MACE-formed structures with melanin is then aimed at an increase of the photovoltaic properties lead by the increased light power entering the MACE-based structures.

The second part of the project regards the PSi impregnation with inorganic materials using an electrochemical approach for the impregnation of the porous matrix with erbium and nickel. Erbium has been chosen because of its demonstrated photoluminescence (PL) properties when hosted in a silicon matrix; the interest on this topic has started to decrease when it has been found that erbium clustering limits the PL emission. In this thesis I will show by a wide multidisciplinar study that pores filling, instead of the standard pores doping approach, can be a promising route to overcome the erbium clusters formation and to enhance the PL intensity. The impregnation of PSi with nickel has a different goal and is aimed at the fabrication of a multiphase material that can be used to define a valid protocol for the analysis and accurate reconstruction of nanoporous materials with atom probe tomography (APT), a technique lacking of a reliable approach for the definition of accurate reconstruction parameters. The main characteristic of this particular pair of materials is that silicon and nickel have similar evaporation fields, which is essential to perform the analysis of porous composite materials with APT.
Despite the different materials and the various technological applications of the analyzed samples, the common feature of the work is the study of the impregnation processes. A good understanding of the impregnation process is the base for the optimization of the final device. The understanding and control of the parameters governing the filling of meso- and nano-pores is in fact a very complex matter that is unavoidably influenced by many environmental parameters (temperature, humidity...) that can be difficult to control properly. For these reasons, my PhD work has been aimed at the understanding of what parameters are fundamental for a successful pores impregnation and why. Although part of the parameters involved necessarily differ for an impregnation with organic and inorganic materials, many are nonetheless related for both kinds materials to size, shape, regularity of the pores distribution, and their knowledgeable control is therefore essential for a wide variety of application.
This work has been done within a collaboration with many national and international research groups. As previously mentioned, most of my work was done in the laboratory PoroSiLab. I was in charge of the fabrication

and impregnation of the PSi samples, of their characterization by means of reflectivity and absorbance analysis and of all the photocurrent measurements. The computational analysis presented in the text, aimed at understanding the polymerization of melanin monomers and the adhesion on a silicon surface, have been carried out by the groups of L. Colombo and G. Cappellini of the same university, while melanin monomers were synthesized at the University Federico II of Napoli by the group of M. d'Ischia. I also fabricated the PSi samples with the MACE technique during a four months international stage at CNRS-ICMPE laboratories in Thiais (France), where I also performed their impregnation with the organic material and all the analysis on those samples. I participated to the PL analysis of the Er-filled porous Si samples that have been carried out by the group of M. Saba of the University of Cagliari. The scanning electron microscope (SEM) images, also using back-scattering electrons (SEM-BSE) and energy dispersive X-Ray spectroscopy (SEM-EDS), of these samples have been taken by the group of A. Falqui at KAUST (Saudi Arabia). Electron tomography (ET) and micro-PL analysis on Er-doped samples and APT and ET on samples impregnated with nickel have been performed in the laboratories of the Université Grenoble Alps and CEA, LETI, MINATEC Campus. Our collaborators from INRIM (Torino) performed SEM analysis of PSi and allowed us to develop the Electrochemical Nanolithography (ENL) technique for samples fabrication, characterized by more regular and larger pores.
Most of the results of this thesis have been published in the following articles in international journals:

- E. Pinna, M. Mehrabanian, E. Redolfi Riva, E. Cara, G. Aprile, L. Boarino, G. Mula, Electrochemical Nanolithography on silicon: an easy and scalable method to control pores formation at the nanoscale, *Materials* **2019**, 12, 18, 2891

- A. Antidormi, G. Aprile, G. Cappellini, E. Cara, R. Cardia, L. Colombo, R. Farris, M. d'Ischia, M. Mehrabanian, C. Melis, G. Mula, A. Pezzella, E. Pinna, E. Redolfi Riva, Physical and chemical control of interface stability in porous silicon-eumelanin hybrids, *J. Phys. Chem. C* **2018**,

122, 49, 28405-28415

- E. Pinna, C. Melis, A. Antidormi, R. Cardia, E. Sechi, G. Cappellini, M. d'Ischia, L. Colombo, G. Mula, Deciphering molecular mechanisms of interface buildup and stability in porous Si/eumelanin hybrids, *Int. J. Mol. Sci.* **2017**, 18(7), 1567

- G. Mula, T. Printemps, C. Licitra, E. Sogne, F. D'Acapito, N. Gambacorti, N. Sestu, M. Saba, E. Pinna, D. Chiriu, P. C. Ricci, A. Casu, F. Quochi, A. Mura, G. Bongiovanni, A. Falqui, Doping porous silicon with erbium: pores filling as a method to limit the Er-clustering effects and increasing its light emission, *Scientific Reports* **2017** 7, 5957

- I. Mouton, T. Printemps, A. Grenier, N. Gambacorti, E. Pinna, M. Tiddia, A. Vacca, G. Mula, Toward an accurate quantification in atom probe tomography reconstruction by correlative electron tomography approach on nanoporous materials, *Ultramicroscopy* **2017**, 182, 112-117

The results obtained and discussed in this thesis have also been presented in the following national and international conferences and events:

- European School on Nanosciences and Nanotechnologies - ESONN (2018):
  - Poster: Nanostructured porous silicon for technological applications.

- Porous Semiconductors Science and Technology - PSST (2018):
  - Oral: A new paradigm for PSi:Er light-emitting structures
  - Posters: Deciphering molecular mechanism of interface buildup and stability in porous Si/eumelanin hybrids
  - Electrochemical nanolithography on highly-doped porous silicon

- XI International School On Hybrid and Organic Photovoltaics and IV School on Advanced Materials for Photonics, Electronics and Bioelectronics - ISOPHOS & MAPHEBIO (2019):

  - Poster: Organic-inorganic hybrids of eumelanin and porous Si: how to improve the junction stability

- 8th Young Researcher Meeting - YRM (2017):
  - Oral: Organic-inorganic hybrids of eumelanin and porous silicon: how to improve the junction stability
  - Poster: Porous silicon/polyaniline hybrid materials for photovoltaic applications

- 79th IUVSTA workshop (2017):
  - Poster: Accurate quantification in atom probe tomography reconstruction by correlative electron tomography approach on nanoporous materials

- E-MRS Spring Meeting (2016):
  - Oral: Organic-inorganic hybrids of eumelanin and porous Si: toward stable photocurrents

- Porous Semiconductors Science and Technology - PSST (2016):
  - Posters: Eumelanin-porous silicon hybrids: towards stable photocurrent
  - Atomistic characterization of the hybrid eumelanin-porous silicon interface: a molecular dynamics study

Contents

Part I

State of the art

Chapter 1

Porous materials impregnation

In this chapter, a general introduction to the main topic of this dissertation, that is the impregnation of a porous silicon (PSi) matrix, is presented. Section 1.1 will give the reader an overview of porous materials impregnation and the physical aspects related to that; then, in section 1.2, the impregnation issue is treated for the specific case of PSi.

1.1 Overview of porous materials impregnation

The impregnation of a porous matrix can be generally described by the physical laws of capillarity [1, 2], which occurs when a liquid flows in narrow tubes without the assistance of external forces like gravity, and sometimes even in opposition to that. Capillarity is the result of two forces, the adhesion of the liquid to solid surfaces and the cohesive surface tension of liquid molecules; these are in opposition one another since the former tends to spread the liquid and the latter tends to reduce the liquid-gas interfacial area. The final liquid-gas interface configuration is found through a balance between these forces. Capillarity is thus dependent on solid and liquid interfacial properties such as surface tension, contact angle, and solid surface roughness and geometry [3]. Surface tension derives from the fact that fluid molecules at the air-fluid interface are subjected to a net attraction force from bulk liquid molecules. Bulk molecules, in contrast, experience uniform cohesive forces

from whatever direction. As a result, a membrane-like fluid surface appears, and it tends to contract to reduce the amount of its excess surface energy. Surface tension depends on the liquid and can be modified by the addition of soluble substances. Temperature also affects surface tension, because the cohesive forces between molecules are reduced in case of thermal expansion: in general, therefore, the experimental conditions of impregnation are a very delicate factor. The impregnation of a surface also depends on the wettability of that surface. From this point of view, a significative parameter is the contact angle, that is the equilibrium angle formed between the solid-liquid interface and the liquid-gas interface. According to this definition, a solid is called *wettable* by the liquid when the contact angle is small (figure 1.1 (a)) and it happens when liquids molecules are attracted to solid surfaces more strongly than to the other liquid molecules. Conversely, a solid is called *not-wettable* by the liquid when the contact angle is large (figure 1.1 (b)) because the cohesive force among the molecules within the liquid is larger than the adhesive force of the solid. Another factor that affects impregnation is surface geometry. In fact, the final liquid-gas interface is the result of a balance between the forces that tend to spread the liquid and surface tension, which tends to minimize interfacial area within the pore. For these reasons, the final interface between the liquid and the gas phases is often curved. A hemispherical interface would be the ideal shape in case of regular solid matrices, while a not-spherical shape is much more common when the liquid is confined by irregular solid surfaces.

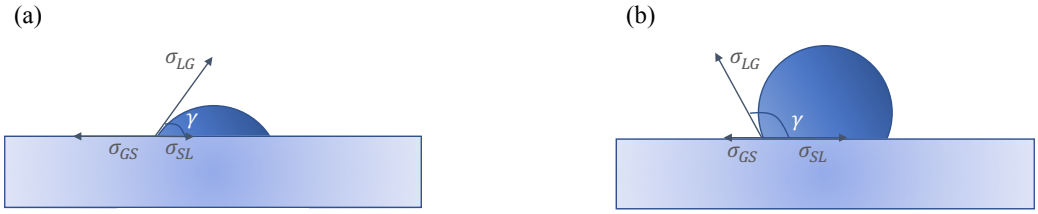

Figure 1.1: *Different solid-liquid-gas contact angles: (a) small contact angle ($\gamma < 90°$ defines a wettable solid); (b) large contact angle ($\gamma > 90°$ defines a not-wettable solid).*

1.2 A more specific case: porous silicon impregnation

PSi is at the base of this dissertation and the study of its impregnation is of particular interest since it permits to tune PSi properties or to develop composite structures with new interesting characteristics. In the second half of the 90s of the last century, for example, several groups tried to impregnate PSi to improve or modify its luminescence properties [4–6], but many other applications aimed at the investigations of PSi impregnation with different materials. Some years later, the filling of PSi has been studied for electronic devices, like the fabrication of an X-ray imaging pixel detector [7] or the realization of microchannels in heat sink technology [8]. Impregnation with magnetic materials has been proposed by the group of P. Granitzer and a relation between the structure and magnetic characteristics has been demonstrated [9–11]. New results on this topic have been found in the last years [12–14]. Impregnation of PSi with organic materials is another field of interest, both for exploiting the properties of the new composites [15–18] and to use the porous matrix as a template to prepare defined arrays of the organic compound [19–21]. These are only some examples, but many other cases can be found in literature [22–26]. Among the various ways to achieve PSi filling, chemical and electrochemical impregnation processes have been used in this dissertation, and a brief description of these methods will be given below.

Chemical pores impregnation consists in putting the PSi sample in direct contact with a solution of the material to be deposited inside the pores, and let the solvent to evaporate, without using any current. This technique is often used for the insertion of metals or polymers [27], but the success of the process depends on chemical and morphological properties of the surface. In fact, a freshly etched SiH_x-terminated PSi is hydrophobic and it should be chemically modified to optimize the impregnation with hydrophilic substances [28]. Another procedure used for polymer impregnation is to spread the polymer solution over the porous surface by spin-coating; in this case, viscosity and rotation speed are important parameters for the success of the pores impregnation. This technique has been used also in this dissertation for impregnation of PSi with melanin, and the results are presented in sections 5.1 and 5.3. In case of the insertion of metals, the process is usually the result of redox reactions where both the metal formation and the silicon atom oxidation occur. For this reason, the reaction is inhibited after the deposition of one or two monolayers, since the silicon atoms are all covered by the new material.

Electrochemical impregnation, instead, is a technique that involves electrochemical reactions inside the pores between silicon and the material dissolved in the solution. The impregnation results strongly depend on the morphological structure of the porous matrix: if for macropores is easy to obtain a homogenous in-depth filling [29], gradients are often observed in case of mesoporous and nanoporous materials [30]. This is probably due to pores shapes, especially when they are dendritic. In fact, an irregular pore shape may lead to pore obstruction due to an irregular electrodeposition of materials lead by inhomogeneous flow of the electrolyte within the complex dendritic pore net. Other reasons for pore-blocking could be an insufficient exchange of the electrolyte along the entire pore length or hydrogen bubbles formation during the reaction. In any case, in the work presented in reference [31] it has been shown that pores filling is also related on current density and on pulse duration, so that to obtain good results a careful optimization of the process is a mandatory preliminary step.

Chapter 2

Porous silicon matrices

In this chapter I will provide a general introduction on PSi and on the various techniques used for producing the porous matrices studied in this dissertation. In particular, after a brief introduction on PSi characteristics and properties in section 2.1, the theory of the anodic etching is presented in section 2.1.1, while section 2.1.2 is dedicated to the explanation of the so-called Metal-Assisted Chemical Etching (MACE).

2.1 Porous silicon

PSi discovery dates back to the 1950s at Bell Laboratories, when the scientists Arthur Jr. and Ingeborg Uhlir were studying an electrochemical technique for polishing and shaping the surfaces of silicon and germanium in order to use them in microelectronic circuits. They noted that, under appropriate electrochemical conditions, some black, brown or red films on the surface of the substrates were formed [32]. Since they were not interested in that effect, they adjusted the experimental conditions to prevent this effect and reported the unusual result in a Bell labs note.
For several decades PSi discovery remained shelved, until the beginning of the 90s, when the interest in this material arose thanks to the independent discovery, by the scientists L. Canham and V. Lehmann, of its photoluminescence (PL) in the visible band, that is at energies significantly higher than

silicon bandgap energy (1,1 eV) [33]. The origin of this optical property is still under debate: two possible explanations are the quantum confinement effect, that arises when the pores are large enough to leave nanometer-scale crystalline silicon skeleton around them [34, 35], or the presence of several emission centers in the PSi inner surface like $Si-H_n$ or Si−OH [36]. After PL discovery, a widespread research activity started for developing silicon-based optoelectronic devices, but the low electroluminescence efficiency eventually led to a decrease of interest for this material. The very peculiar characteristics of this material, as the huge developed inner surface or the possibility to easily tune pores length and dimensions, inspired the use of PSi for many other technological applications that did not need intense PL emission, as in the sensor, biomedical, electronics and optics fields. Many research groups are still working in this research domains.
One of the main characteristics of porous materials is of course their porosity, defined as the void percentage of the sample. Porous materials can be classified according to their pores average diameter x:

- Micropores: $x < 2$ nm;
- Mesopores: $2 < x < 50$ nm
- Macropores: $x > 50$ nm

Pores dimensions, in terms of their average diameter, length, shape, are strictly affected by the electrochemical parameters used to perform the etching process. In particular, the etching time controls the pores length, while the current density and the solution composition affect the pores diameter. The doping type and level of the original crystalline silicon substrate also play an important role in determining the pores dimensions; in fact, keeping constant the other electrochemical parameters, the higher is the dopant concentration of n-type silicon wafer, the smaller are the pores that one can form with this substrate; the opposite is true for p-type silicon wafer: the higher is the dopant concentration, the larger is the pores diameter.

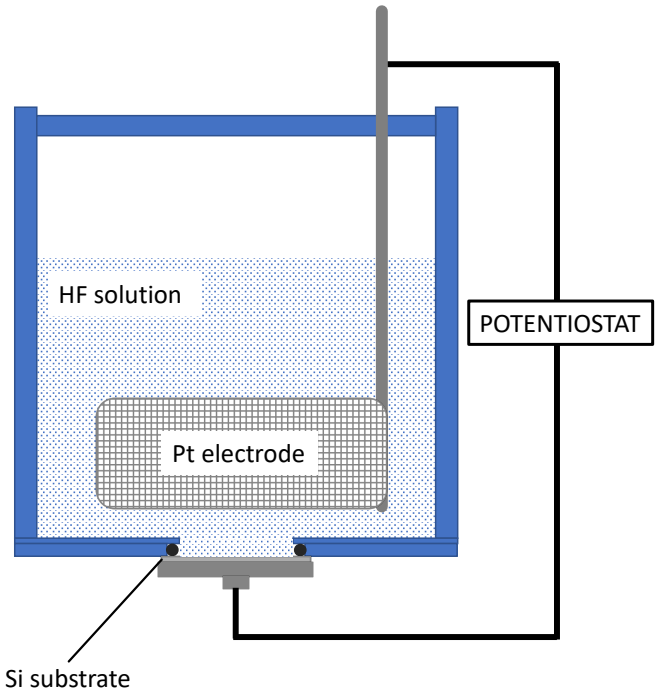

Figure 2.1: *Detailed scheme of the apparatus used for the electrochemical preparation of a PSi layer.*

2.1.1 Anodic etching

One of the most diffused methods used to produce PSi is anodic etching, alternatively called electrochemical etching. This method requires an apparatus as the one schematically represented in figure 2.1. The electrochemical system consists in an electrochemical cell where the silicon substrate represents the anode (working electrode), while the cathode (counter electrode) is a grid made of platinum. The mostly used electrolyte is an aqueous HF solution, which has the double function of etching the silicon when the current is applied, and removing the surface oxide layer, that naturally forms on the surface, before the electrochemical process starts. Silicon, in fact, is very reactive with the oxygen present in air and water; since the oxide layer freshly formed is an insulant from the electrical point of view, it modifies the original properties of the semiconductor and prevents the porous formation.

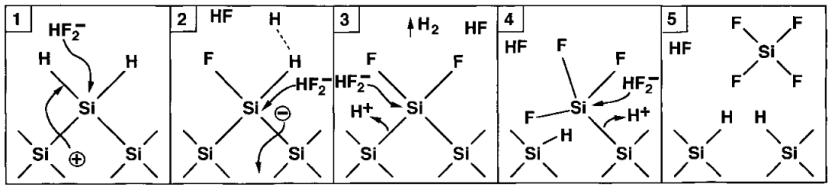

Figure 2.2: *Reaction scheme for the divalent model of the porosification process [37].*

On the base of the electronegativity values of the elements, the enthalpy of Si−F is higher than the enthalpy of Si−O, so the HF solution easily dissolves the oxide layer, according to the following reaction:

$$SiO_2 + 6HF \rightarrow SiF_6^{2-} + 2H^+ + 2H_2O$$

Once the oxide layer has been removed, superficial silicon is now passivated by Si−H bonds and the porosification process can occur. The charge transfer reaction that led to the removal of the surface silicon atoms is a divalent mechanism (figure 2.2). The dissolution process starts when a hole that travels inside the crystal reaches the interface between silicon and the electrolyte. This favors the nucleophilic attack of the silicon atom by bifluoride ions ($HF_2{}^-$), and the new Si−F bond is formed. At this point, another nucleophilic attack can occur on the same Si atom, with the injection of an electron as a result: this leads to the formation of a second Si−F bond and to the emission of a gaseous H_2 molecule. Because of the polarity of the Si−F bonds, the electron density of the remaining two silicon backbonds is weakened, and facilitates the dissolution of the Si atom by HF. The overall reaction of the divalent porosification process is the following:

$$Si + 4HF_2^- + h^+ \rightarrow SiF_6^{2-} + 2HF + H_2 + e^-$$

PSi formation can occur only for particular condition of the electrical parameter, as it shows the graph in figure 2.3, that connects the current density

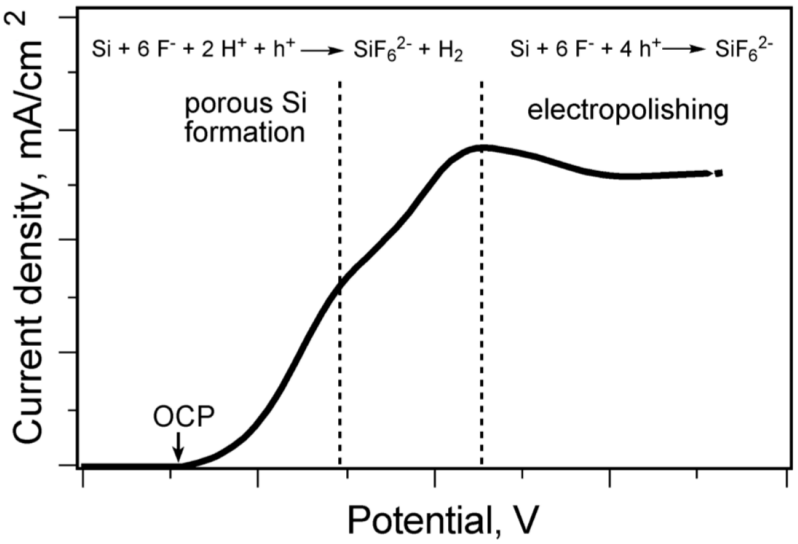

Figure 2.3: *Evolution of Si electrochemical etching depending on the current density and the applied tension between the electrodes [38].*

flowing in the cell with the potential applied between the electrodes.

Three different regions can be distinguished:

- the first region, corresponding to low values of the applied potential, is the effective region where the PSi formation occurs, with the only restriction that the applied potential must be higher than the open circuit potential (OCP), otherwise no current can circulate between the electrodes;
- in the second region the silicon porosification continues and the porous layer becomes very fragile;
- the third region is the so-called "electropolishing-region", where it happens that the porous layer is no more there because the silicon atoms are uniformly removed from the layer.

2.1.2 Metal-assisted chemical etching

Metal-assisted chemical etching is an alternative way to produce PSi without using any external current or voltage. The first demonstration of this method for Si etching dates back to 1997, when PSi was fabricated starting from an Al-coated silicon substrate immersed in a solution of HF, HNO_3 and H_2O [39]. Reports on the use of metal-assisted chemical etching are also present for GaAs, GaN and SiC [39]. This method uses the combined action of noble metals like Al, Ag, Au, Pd, Pt, Fe or Au−Pd alloys, and a solution of hydrofluoric acid and a mild oxidizing agent (such as H_2O_2, HNO_3, $KMnO_4$ or $HClO_4$). The metals are deposited as films or nanoparticles in the silicon surface and act as catalysts in the pores formation, accelerating the etching effect of the oxidizing agents. Depending on the conditions, the corrosion can occur either immediately below the metal catalyst [40, 41], giving a very good spatial control, or also everywhere around it [42, 43]. Generally speaking, the mechanism of the etching method can be described as follows [44]. Suppose to have a MACE system where a silicon substrate is coated with a gold catalyst film, and H_2O_2 has been used as the oxidizing agent. In this system, a hole is injected from the metal into the silicon, oxidizing it according to the following reaction:

$$H_2O_2 + 2H^+ \xrightarrow{Au} 2H_2O + 2h^+$$

The oxidized material reacts with hydrofluoric acid to form soluble silicon hexafluoride and gaseous hydrogen. The etching reaction is reported hereafter, while figure 2.4 represents the graphic scheme of the process.

$$Si + 4HF_2^- + 2h^+ \rightarrow SiF_6^{2-} + 2HF + H_2$$

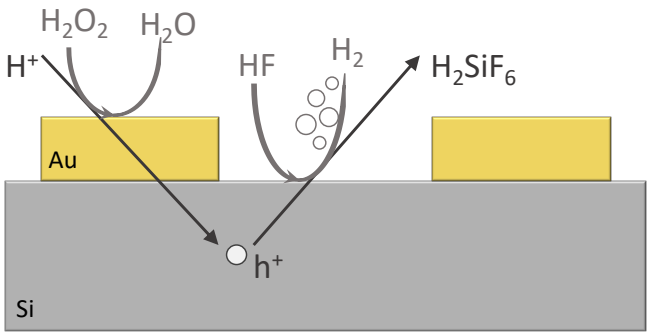

Figure 2.4: *Graphic scheme of silicon etching according to metal-assisted chemical etching.*

Chapter 3

Organic and inorganic materials to fill a porous matrix

In this chapter an overview on the materials that have been used to impregnate the PSi matrix is presented, with a focus on their characteristics and properties that led to their choice for this research. In section 3.1 some information on the origin and the main properties of melanin is given; section 3.2 reports the main characteristics of erbium, esccpecially when it is used to produce a silicon-based photoluminescent structure; finally section 3.3 describes the main properties of Ni with respect to the application studied here.

3.1 Melanin: an organic material for hybrid photovoltaic heterojunctions

Melanin is a light-absorbing polymer commonly known as the dark pigment that gives the colour to human skin, but it is also regarded by researchers as one of the most enigmatic biopolymers existing in nature [45]. Several classifications have been proposed for melanins; R. A. Nicolaus in 1964 suggested a classification of melanins into three main groups [46]: eumelanins, pheomelanins and allomelanins. The first two groups include animal pigments, while the latter includes dark non-nitrogenous pigments found in plants, fungi and bacteria. A more recent definition has been proposed in 1995 by G.

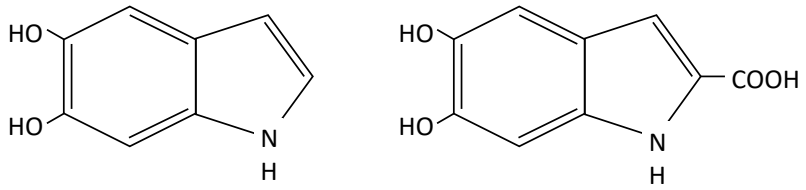

Figure 3.1: *Chemical structures of the two main monomers of eumelanin, DHI and DHICA, that have been used in this dissertation.*

Prota [47] as the pigments formed by oxidation of tyrosine and related metabolites within the cells. Both eumelanin and pheomelanin are present to various degree in human skin and hair [48], but their origins are different. It is commonly accepted that eumelanin is a heterogeneous macromolecule composed of the two main monomers DHI (5,6-dihydroxyindole) and DHICA (5,6-dihydroxyindole-2-carboxylic acid) (figure 3.1), while pheomelanin is another heterogeneous macromolecule derived from a more complex monomer containing sulphur [49].

The two monomers DHI and DHICA can oxidize further, and each molecule can also exist in various redox states, increasing the grade of disorder in the polymeric structure [50]. The relative amount of the two monomers depends upon whether considering natural or synthetic eumelanin [51]: it has been demonstrated that the latter contains around 10% DHICA while the natural version up to 50%. But, despite the huge knowledge about eumelanin monomers, the shape of the polymerized melanin molecule is still under debate, mainly due to the fact that it is insoluble in water over a broad pH range, and that the constituent subunits are irregularly arranged and not easy to purify [52]. The most accredited theory assumes that eumelanin is composed of stacked oligomeric protomolecules, consisting of about 4 to 6 indolequinone

units, as large as 15 to 20 Å and with an interplanar distance of 3.4 Å; this theory has been demonstrated through scanning electron microscopy measurements by the group of G. W. Zajac [53]. In this study, the focus is on eumelanin and on its optical and conductive properties, since this organic material has been used as an absorbent material for photovoltaic applications. Particularly interesting is the absorption spectrum of a eumelanin film; as it is visible from figure 3.2, it is a broad-band, continuous and monotonic absorption spectrum, more like an inorganic material than an organic one. In fact, the curve can be fitted with a single exponential (as in the insert) and the total absence of any peaks corresponding to transitions between distinct electronic states and/or satellite vibronic states is visible. For this characteristic, it has been proposed to describe melanin with a banded semiconductor model, according to which every monomer has discrete energy levels; as the monomers link together to form polymers, the energy levels become denser and denser and close up to form continuous energy bands. There exist the HOMO (Highest Occupied Molecular Orbital) and LUMO (Lowest Unoccupied Molecular Orbital) orbitals, that correspond to the top of valence band and the bottom of conduction band in organic semiconductors, respectively.

The most diffused theory to explain eumelanin absorption spectrum is related to scattering; reference [55] reports that the natural pigment in particle form must be characterized by Mie and Rayleigh scattering. The latter depends from radiation wavelength as λ^{-4} and occurs when particles dimensions are much lower than incident wavelength (e.g. tens of nanometers); according with computational calculations [56] it should cause the stiff increase of the spectrum for $\lambda < 300\,\text{nm}$. The former, instead, happens when radiation interacts with particles in the micron-range; it has no dependence on wavelength, but can contribute to the melanin absorbance spectrum since it superimposes a broad background on any absorption spectrum. However, it is worth to say that the broad spectrum evolves during the oxidative coupling of precursors such as DHICA or DHI [57], when the oxidative breakdown of the pigment occurs [58], or when low molecular fraction are isolated [59]. In this disser-

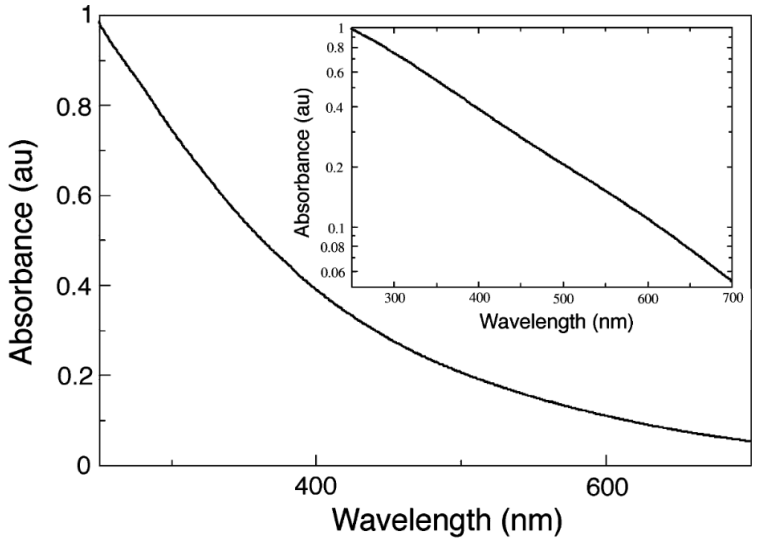

Figure 3.2: *Monotonic, broad band UV-Visible absorption spectrum of a synthetic film of eumelanin. In the insert, the fit with a single exponential and the absence of distinct chromophoric peaks are visible [54].*

tation, a contribution in the understanding of the polymerization of these molecules and a study of a hybrid diffused heterojunction made of eumelanin and PSi are presented [60, 61].

3.2 Erbium: an inorganic material for silicon-based photoluminescence devices

Erbium is one of the 17 elements that constitute the class of rare earths, all of them characterized by three valence electrons. These elements come predominantly from USA and China and, after their extraction, separation and purification, they are commercialized as oxides, carbonates, chlorides, fluorides, borides, hydroxides or as pure metals or alloys. The application fields span from the production of computer and television screens, to optical fibers, transistors [62] and rods for nuclear reactors [63]. Erbium is an interesting material for the optical luminescent properties of its ions Er^{3+} when hosted

in a non-centrosymmetric site, that are useful as active materials for laser. In fact, Erbium-doped crystals can be used as optical amplifiers [64], where ions are excited and then immediately decay from the excited state emitting light at around $\lambda = 1.5\,\mu m$. For this reason, erbium could be used for the production of optical fibers, whose most effective transmission window is in that wavelength range. Since optical fibers are prevalently made of silica (SiO_2), it would be convenient to industrialize hybrid devices made of Er and silica, in order to put together the luminescent emission of the former with the transmission properties of the latter. Silicon structures like silicon-rich-oxide (SRO) are the most studied for these applications and are mainly fabricated by chemical-vapor-deposition [65–67], where gaseous compounds like SiH_4 and N_2O are conveyed onto a hot silicon substrate, forming a silicon layer rich in oxygen. These structures can be doped with rare earths (Er, Yb, Tb...) by various methods as for instance ion implantation [68]. The activation of the rare earth ions is obtained through a thermal treatment, which serves for dopants diffusion inside the silicon structure. Their light emission properties at room temperature have been demonstrated in reference [69]. Other interesting structures are Er-doped silica nanoparticles produced by co-sputtering [70] or ion implantation [71, 72], that showed PL emission thanks to the strong coupling between Si nanoparticles and ions Er^{3+} resulting from excitation transfer from the broad-band absorbing silicon to the narrow-band rare-earth emission. Thanks to the interaction between silica nanoparticles and erbium ions, it is possible to excite these latter indirectly, which means that it is not mandatory to use a pump wavelength corresponding to any of the principal Er^{3+} absorption bands [73]. The excitation exchange mechanism between silicon nanocrystals and erbium ions has been theoretically studied [74, 75] and can be generally schematized as in figure 3.3: an initial optical absorption produces an exciton within the silicon that is then exchanged and goes to excite and immediately deexcite the rare-earth ions. There is also an upconversion step in which a rare-earth ion already in the $^4I_{13/2}$ metastable state is promoted to higher states by further interaction with an excited silicon nanoparticle.

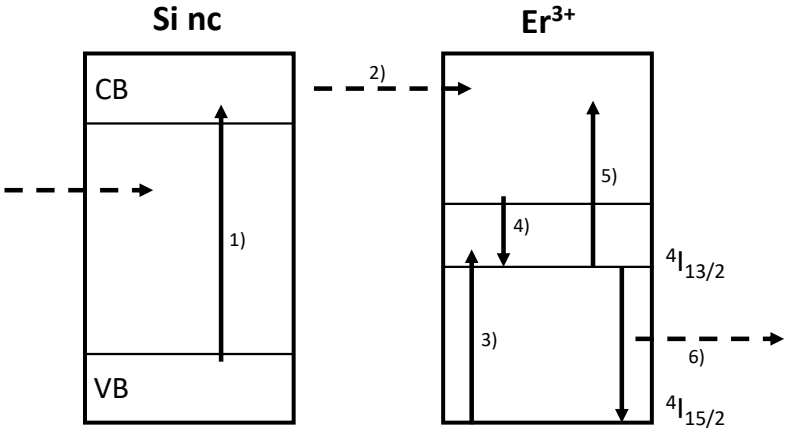

Figure 3.3: *Schematic mechanism for excitation exchange between silicon nanocrystals and erbium ions. The process is schematized with numbered arrows as follows: 1) an electron-hole pair is created by absorption of a photon; 2) excitation exchange; 3) promotion of an electron from the ground state of erbium to an unspecified excited state; 4) decay to the metastable state; 5) upconversion; 6) emission of a photon with* $\lambda = 1535\,\mathrm{nm}$ *[76].*

An alternative to silicon-rich-oxide for the developing of erbium-doped light-emitting devices is PSi. Several works can be found in literature on this topic [77–81], but the interest decreased after the discovery of erbium clustering effect that limits the PL emission [82]. Previous studies on Er-doped PSi samples led us to the understanding of several aspects of the electrochemical doping process [30, 83–86]. In this dissertation the electrochemical doping process has been more thoroughly analysed, and it brought about a new approach on the PSi:Er structures fabrication [87]. The details and the results will be discussed in section 6.

3.3 Nickel: an inorganic material for a better understanding of porous matrices impregnation

Nickel is a transition metal, with atomic number 28 and it appears like a silvery-white metal with a slight golden tinge. Pure nickel can be very reactive when in the form of powder, because the reactive exposed area is maximized, or much less when in larger pieces, because the external surface is passivated by the formation of a stable oxide layer. Because of this inert behaviour, nickel has been largely used for electroless plating [88], coating of chemistry equipment [89], and manufacturing alloys that retain a high silvery polish [90]. Another important application of this material is as a catalyst in many chemical reactions, which are of interest both preparatively and industrially [91]. Nanoporous nickel has attracted great attention for its applications in photonic materials [92], electrochemical capacitors [92] and electrocatalysts for hydrogen [93–96] and oxygen evolution reactions [97–100]. Nanoporous nickel production requires electrochemical dealloying of Ni-Cu systems under specific experimental conditions. The reason why nickel has been used in this dissertation has no root in any industrial or chemical application, but is the attempt of improving a protocol for analysis and accurate reconstruction of nanoporous materials by atom probe tomography (APT) [101] based on the expertise acquired studying the electrochemical mechanisms of PSi pores filling with Er. In fact, nickel has been chosen to fill PSi samples because it has an evaporation field close to that of Si, so this multi-phase material behaves sufficiently like a single-phase material during the evaporation process at the basis of APT measurement to allow a correct analysis of the results.

Part II

Methods

Chapter 4

Fabrication and measurement methods

This chapter describes the technical details about materials and methods employed during fabrication, characterisation and measurements described throughout the dissertation. The fabrication procedures of the PSi substrates are treated in section 4.1, and include both the electrochemical etching and the metal-assisted chemical etching. The methods adopted for the characterisation of the substrates from the structural and morphological point of views are reported in section 4.3. The measurements of photocurrent and PL of the various analyzed samples are finally described in section 4.4.

4.1 Fabrication of the substrates

4.1.1 Electrochemical etching

PSi samples were prepared at the PoroSiLab of the University of Cagliari starting from monocrystalline n-type phosphorous doped (100)-oriented silicon wafers from Sil'tronix (Archamps Technopole, Archamps, France), cleaved in 1.5 cm per side squares. Two kinds of samples can be distinguished depending on the pores dimensions:

- samples with pores diameter from 10 to 20 nm

- samples with pores diameter from 40 to 60 nm

For the first type, Si wafers with a resistivity in the range from 3 to 7 mΩcm were used, and the electrochemical etching has been carried out in the dark using a solution of HF/H_2O/EtOH 15:15:70 in volume. A constant current density of 200 mA cm^{-2} was applied for 25 s. The thickness of the resulting porous layer was then around 1.3 µm.
For the second type of samples, a slightly lower dopant concentration was needed (resistivity from 15 to 18 mΩcm) in order to obtain larger pores. The porous layers fabricated with these substrates were etched following a preliminary lithographic step that has been developed as a part of my thesis work and for which a patent application has been submitted [102]. The method, called **Electrochemical Nanolithography (ENL)**, is a lithographic process aimed at the fabrication of controlled roughness on the Si surface using only standard electrochemical processes. Thanks to this controlled roughness, ENL allows the control of pores density, size homogeneity and distribution order by simply adjusting the electrochemical parameters used during the ENL step. ENL consists in the fabrication of a sacrificial double layer that serves to leave indentations in the silicon surface after being dissolved with aqueous NaOH solution. Surface indentations act as seeds for the formation of a new porous layer, whose morphological characteristics depend on the parameters chosen for their fabrication, while the pore density, distribution order and size homogeneity are controlled by ENL. A detailed explanation of the process will be reported in the results section, in paragraph 5.2. The electrochemical parameters used in this dissertation for the sacrificial double layer of the ENL samples were:

- HF/H_2O/EtOH 25:25:50 solution, 600 mA cm^{-2} for the first layer;
- HF/H_2O/EtOH 22:22:56 solution, 800 mA cm^{-2} for the second layer;

The third final layer has been produced using the same electrochemical parameters of the second layer since this set of parameters was well adapted to the fabrication of pores with characteristics suitable for this study. The duration of the etching has been calibrated in order to produce the same

thickness as that of the samples fabricated with the standard electrochemical etching, that is about 1.3 µm.
For both the PSi layer types, the potential source was a PARSTAT 2273 potentiostat from Princeton Applied Research (Oak Ridge, TN, USA). To perform the electrochemical etching, a conventional home-made two-electrode cell was used: the Si substrate represented the working electrode and was located at the bottom of the cell, while a platinum cylindrical grid placed close to the bottom of the cell constituted the counter electrode. The electrical contact with the Si consisted in an inox disc, and the exposed geometrical area of the electrode was about 0.6 cm^2 (diameter 0.9 cm). The various components of the cell are schematically shown in figure 2.1 of section 2.1.1.

4.1.2 Metal-assisted chemical etching

Metal-assisted chemical etching is the alternative technique for PSi fabrication that has been used at CNRS-ICMPE labs located in Thiais, France. In this case, double-polished crystalline (100)-oriented silicon wafers, with thicknesses in the range 250 µm to 280 µm, have been used. The wafers, that were n-type highly phosphorous-doped, with a resistivity in the range 1 to 5 mΩcm, have been cleaved in squares 1 cm side substrates and cleaned for 20 min with piranha solution (96-97% H_2SO_4/30% H_2O_2 3:1 in volume) to remove organic traces. After being rinsed with abundant ultrapure water, the samples have been immersed for 5 minutes in HF 1 M to remove surface oxides and to hydrogenate the Si surface. To activate the metal-assisted chemical etching, a pattern of metal nanoparticles must be deposited, since the metal acts as a cathalytic agent in the etching process by the oxidizing solution. Metal nanoparticles have been produced in two different ways:

- by immersing the sample in a aqueous solution of 1 mmol H_2PtCl_6 and 90 mmol HF for 2 min;
- by sputtering the sample with a 10 nm layer of Ag and then annealing it for 20 min at 275 °C in Ar atmosphere.

The etching has been performed just after the metallization by immersing the samples for 20 min in an HF/H_2O_2 aqueous solution, where [HF]=1,21 M and $[H_2O_2]$=0,21 M, so setting a ratio:

$$\rho = \frac{[HF]}{[HF] + [H_2O_2]} \tag{4.1}$$

of 0,75 for all the etching procedures.

4.2 Impregnation of the substrates

All the impregnations of PSi matrices have been carried out at the PoroSiLab. Different materials have been used to impregnate the samples: the chemical filling of the pores with melanin is described in 4.2.1, while the electrochemical impregnation processes with erbium and nickel are treated in 4.2.2 and 4.2.3, respectively.

4.2.1 Porous silicon filling with melanin

Polymerization of melanin inside the samples pores was carried out using Ammonia-Induced Solid State Polymerization (AISSP) procedure reported in [103]. The impregnation starts by dissolving a given amount of DHI monomer in a given volume of EtOH. In this dissertation, the effect of several concentrations has been explored: 8, 16 and 24 $\mathrm{mg\,mL^{-1}}$. Then, a drop of the monomer solution is deposited on the sample and distributed uniformly on the porous top surface by spin coating for 3 minutes. This has the double effect of favoring the penetration of the DHI solution within the pores and of forming a homogenous thin organic layer on the top of the sample. Once impregnated, the samples were exposed to NH_3 atmosphere for the AISSP oxidation of the molecules and therefore for the polymerization of DHI. The duration of this process was 15 minutes.

4.2.2 Porous silicon doping with erbium

PSi samples were electrochemically doped with erbium using an ethanoic 0.11 M solution of $Er(NO_3)_3\ 5\,H_2O$ salt. Before the beginning of the process, the samples were let in contact with the solution for one minute under slow stirring, in order to facilitate the solution exchange at the external surface of the PSi layer. The electrochemical doping was carried out in constant current mode, applying 1 mA for different times, depending on the amount of erbium it was supposed to deposit in the PSi matrix. The chosen doping times were 30, 100, 150, 200, 250 and 300 s, corresponding to Er amounts of 1.2, 4.0, 6.0, 8.0, 10.0, 12.0 %, respectively. Since there is always a gradient in the erbium content inside the porous matrixes, these values refer to the content towards the external surface. Once the electrochemical impregnation is finished, the cell must be immediately empty in order to prevent the Er-ions to go back to the bulk solution; then, after removing the sample from the cell, it must be carefully and quickly rinsed with distilled water, again to avoid the removal of the erbium from the pores.

4.2.3 Porous silicon filling with nickel

The electrochemical filling of PSi with nickel has been performed using the so-called "Watts bath" containing $NiCl_2$ 45 g L^{-1}, $NiSO_4$ 300 g L^{-1} and H_3BO_4 45 g L^{-1}. To achieve an optimal filling of the pores, the electrochemical Ni deposition process was performed by pulsed electrodeposition: current density pulses at -1.6 mA cm^{-2} were applied for 5 s separated by a 5 s delay at zero current for 120 cycles.

4.3 Structural characterization

Structural and chemical characterization of the samples have been done in research centers other than University of Cagliari. In particular, SEM and SEM-EDS analysis on Er-doped PSi samples have been carried out at KAUST thanks to the collaboration with the group of A. Falqui, while the same kind

of analysis on MACE nanostructured PSi filled with melanin has been done at CNRS-ICMPE (Paris) by the group of S. Bastide; the structural analysis of ENL samples, both in plane view and in cross section, have been performed with the SEM at INRIM by the group of L. Boarino. All the details about SEM analysis are reported in section 4.3.1. Both Er-doped and Ni-filled PSi samples have been analyzed by tomography at Minatec of Grenoble, as reported in 4.3.2.

4.3.1 SEM

Er-doped PSi samples were analyzed by using a Zeiss Merlin scanning electron microscope, equipped with a Schottky field emission gun, a Raith pattern generator, an Oxford EDS X-Max SDD detector with an area of 80 mm^2 and the AzTecEnergy EDS analysis software. To collect both the EDS elemental maps and spectra, the microscope operated at an acceleration voltage of 15 kV and a beam current of 5.5 nA. EDS quantitative analysis was performed by using a ZAF standardless method. The X-Ray peaks chosen for both the EDS mapping and quantitative analysis were the O K, Si K and the Er L, respectively. The same microscope has been used to collect SEM image of the samples surface and that of the PSi layers in cross sectional view, using the secondary electron (SE) signal. In this case, the microscope acceleration voltage was 4 kV and the beam current 300 pA. SEM images and SEM-EDS analysis of MACE samples filled with melanin were obtained with a Merlin FEG microscope from Zeiss, equipped with AZtec systems (EDS Advanced, HKL Advanced Nordlys Nano, Oxford Instruments). The morphological characterization of ENL samples was carried out using a Field Emission Gun SEM (FEI Inspect F).

4.3.2 Electron tomography

ET analysis have been carried on PSi with erbium as a collection of a series of scanning transmission electron microscopy (STEM) images. In particular, needles with a diameter of few hundreds nanometers have been extracted by the samples using a focused ion beam (FIB) FEI Strata instrument.

The extraction from the sample has been performed after being protected with a layer of tetraethyl orthosilicate, glued at the top of a tip and finally inserted in the transmission electron microscope (TEM). The acquisitions have been performed either on a FEI Titan Ultimate TEM or on a FEI Themis TEM, working in scanning mode (STEM) with a high angle annular dark field (HAADF) detector, in order to both prevent from the diffraction that could limit the reliability of the sample volume reconstruction and enhance the contrast due to the atomic number difference between Si and Er. The acceleration voltage during the acquisition was 80 kV to limit the damage to the PSi structure. During the acquisition, the samples were tilted over a 180° tilt range, with a constant tilt step of 1°. The 181 acquired images (projections) have been analyzed with a dedicated algorithm to reconstruct the needle volume, after a fine alignment between the needle projections and the tilt axis, according to the procedure reported in [104]. Moreover, a non-rigid alignment has been used to correct the possible sample deformation that may occur during the needle tomography series acquisition and may lead to deformation-related artifacts during the 3D-reconstruction [105]. A Matlab-based custom-made software has been used for projection denoising, alignment and reconstruction of the samples volume.

4.4 Samples measurements

4.4.1 Photocurrent measurements

Photocurrent measurements on PSi samples with melanin were carried out to evaluate the device properties. In order to perform these measurements, a metallic contact was prior deposited on the samples top surface: in particular, a semitransparent gold layer was sputtered with an Emitech K450 on a portion of the impregnated surface, concentrically; the back contact, was obtained with a little drop of silver paste directly on the bulk silicon, previously scratched in order to remove the native oxide layer. To illuminate the samples, a white light source (tungsten halogen lamp) was focused on the samples surface by means of an optical fiber and of a microscope objective to a circular

area with a diameter of 0.4 cm. Both dark and white light photocurrent measurements have been done, and a series of long-pass filters was used to observe the spectral response in the UV-Vis range (305 nm to 830 nm). The measurement of the produced photocurrent was done using either a Keithley (Keithley Instruments, Cleveland, OH, USA) 6487 or 2450 SMU multimeter according to the experimental needs.

4.4.2 Photoluminescence measurements

Continuous-wave photoluminescence

PL measurements on Er-doped PSi samples have been carried out at room temperature in continuous wave mode. A diode-pump solid-state laser, with an excitation wavelength of 532 nm, an excitation power of 770 mW and a spot size of about 200 µm has been used. The optical emission from the samples was dispersed by a 30 cm focal length Acton spectrometer, equipped with a 75 groves/mm grating blazed at 1200 nm; the detector was an InGaAs Andor line CCD.

Time-resolved photoluminescence

Time-resolved PL measurements on the same kind of samples, instead, have been done employing a pulsed regenerative amplifier as light source (Quantronix Integra, 100 fs pulse duration, 1 kHz repetition rate, 1 mJ energy/pulse, 800 nm in wavelength). For the detection, the same spectrometer used for continuous wave measurements has been used, but the light was directed to a second output port equipped with a Hamamatsu InGaAs fast photomultiplier, used in current mode and whose signal detected with a Tektronix GHz oscilloscope.

Spatially-resolved photoluminescence

Micro-PL measurements and mappings were done at room temperature using a Horiba LabRAM HR spectrometer. A laser of 2 mW power and 633 nm wavelength was focused with a 100x Leica objective (numerical aperture 0.9). The spectrometer was equipped with a 150 grooves/mm grating and an InGaAs array. Due to long acquisition times, a background spectrum was

systematically subtracted.

Part III

Results and discussion

Chapter 5

Porous silicon impregnated with melanin

In this chapter, the results obtained on a hybrid heterojunction between PSi and eumelanin are presented. In particular, we will describe in 5.1 the adopted strategies to improve the interface stability between eumelanin and PSi in 10 nm-diameter PSi samples. Section 5.3 is dedicated to the enhancement of the junction stability that has been obtained thanks to the introduction of a new method of PSi fabrication, whose pores diameter is about 50 nm. Finally, in section 5.4 is reported the attempt to produce a similar hybrid heterojunction using eumelanin to fill nanostructured porous silicon obtained by MACE.

5.1 Thin-pores samples with eumelanin

This hybrid heterojunction with photovoltaic properties has been proposed in 2012 by Mula et al. [106] using n-type PSi and eumelanin. The latter is a natural pigment characterized by a relatively high proton-based electrical conductivity [54] and a dark colour, and it behaves like a p-type semiconductor; for those reasons, a p-n junction can be produced if eumelanin is inserted into the n-type PSi. An increase of the optical absorption range with respect to Si and to the bare PSi has been found after the insertion of the organic

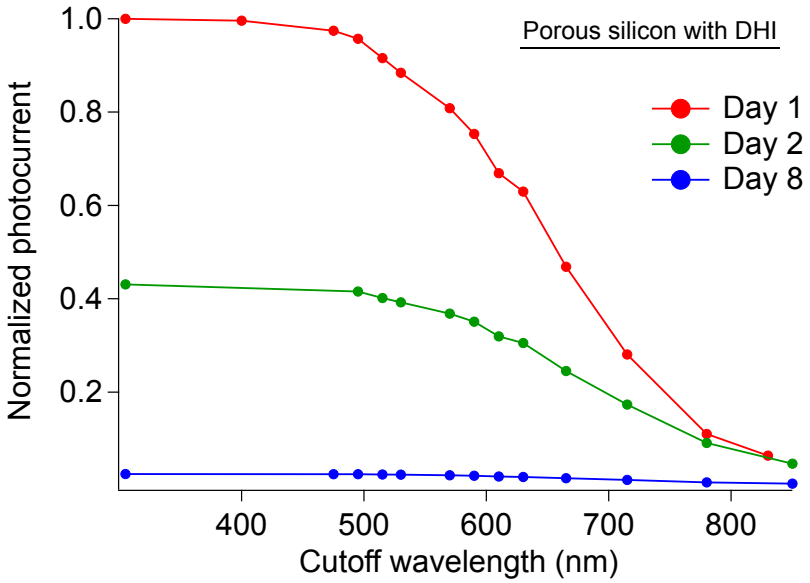

Figure 5.1: *Normalized photocurrent measurements on one eumelanin-impregnated PSi sample, obtained in three different days.*

material in the PSi matrix. In particular, the effect of the eumelanin presence is visible in the near-infrared region, where the absorption capability of silicon is weak. Some improvement in the optimization of this hybrid heterojunction have been made [107], but several issues remained to be solved. Among them, temporal stability is one of the first that needs to be addressed. To have more efficient and stable PSi-eumelanin devices, it is important to have a better understanding of the molecular mechanisms that occur during the polymerization process and to improve the adhesion between organic and inorganic parts in the interface.

To investigate the junction temporal stability, the photocurrent produced by a eumelanin-impregnated PSi sample has been measured for several days, according to the methodology described in 4.4.1. Figure 5.1 shows the typical behaviour of a thin-pores PSi sample impregnated with eumelanin. From now on, this type of sample will be referred to as *standard sample*. The graph shows that, after one day from the sample fabrication, the measured photocurrent is reduced by more than one half with respect to the first measurement, and

it is around zero after one week. The possible explanations for this behaviour could be likely linked to phenomena taking place during the polymerization, the organic/inorganic interface formation and/or within the polymer itself once the polymerization process is finished. These can affect both the polymer conductivity and the Si/polymer interface resistance. In order to achieve a better understanding of the mechanisms involved in the hybrid material fabrication steps and to improve the junction durability, we investigated the PSi/eumelanin interface and the polymerization process. The insufficient formation of stable chemical bonds between PSi and eumelanin can lead to the formation of an unstable interface; in fact, a typical phenomenon that happens during polymerization is the volume contraction with respect to the volume occupied by the initial monomers. This is a general problem that can has relevant consequences for the applications involved, for example in case of orthodontic resin [108]. In this eventuality, a partial detachment between the organic and inorganic parts of the junction could occur, leading to a reduction of photocurrent generation. To investigate what parameter was more relevant in the interface formation and lifetime, we modified several parameters, namely the amount of SiO_2 at the interface, the monomer distribution in the impregnation solution and finally the average pore diameter. This latter aspect required a dedicated study for an optimal fabrication process and will be described in paragraph 5.2. The first step was a light electrochemical oxidation of the porous inner surface, since the presence of SiO_2 is expected to favour the chemical bond of DHI to the surface thanks to a better affinity of the organic monomer with silica. It is reported in literature that a thin oxide layer can enhance the photovoltaic properties in hybrid silicon/organic devices [109–113]. This oxidation has to be carefully calibrated since, if in excess, it would block the charge transfer between the two materials, canceling the photovoltaic behaviour. Since the electrochemical oxidation process is mainly governed by the transferred charge, we chose a constant current approach using a $-2\,\mathrm{mA}$ current and a 0.1 M KNO_3 ethanoic solution. The oxidation grade was calculated as follows: an oxidation of 50 at% (measured by SEM-EDS) is obtained in a constant current process for a process duration corresponding to the time needed to reach the maximum applied voltage of

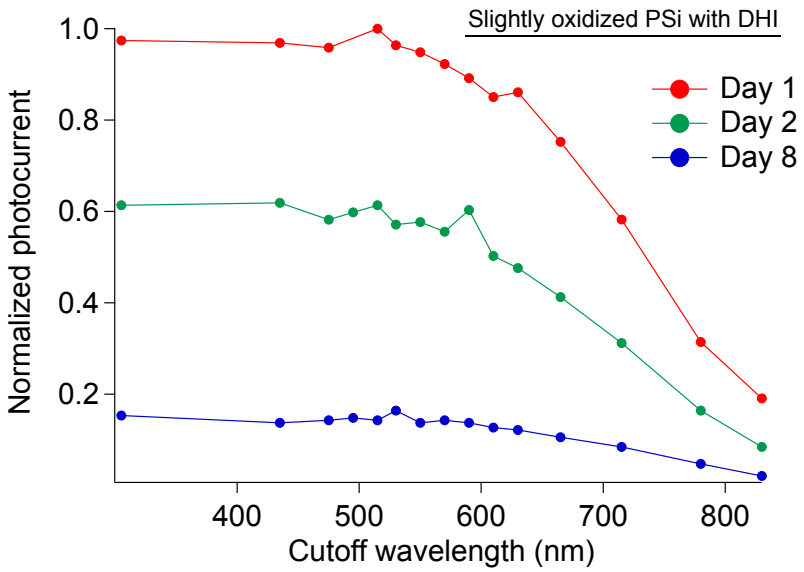

Figure 5.2: *Normalized photocurrent measurements on one slightly oxidized eumelanin-impregnated PSi sample, obtained in three different days. The oxidation of the PSi matrix has been done electrochemically before the impregnation with eumelanin.*

the available potentiostat (10 V). Using this reference, the oxidation of the inner PSi samples in this case was about 3%; direct measurement of the oxide thickness on the pore walls has not been done because, given the complex structure of the pores, it is a result hard to achieve even with state-of-the-art techniques and beyond the scope of this research. In figure 5.2 we report the typical behaviour of a hybrid sample where a slight oxidation has been performed before the impregnation. A small improvement in the junction stability is visible: in the first two days the photocurrent drops by 40%, while it was 60% in the case of the standard samples. Moreover, one week after the sample fabrication, photocurrent was still 15% of the initial value, while in the previous case the photocurrent values after one week were almost zero. This result implies that while the interface clearly plays a role and is affected by the chemical details during the fabrication process, it does not seems to be the key parameter in our methodology.

The second approach used to improve the temporal stability was based on

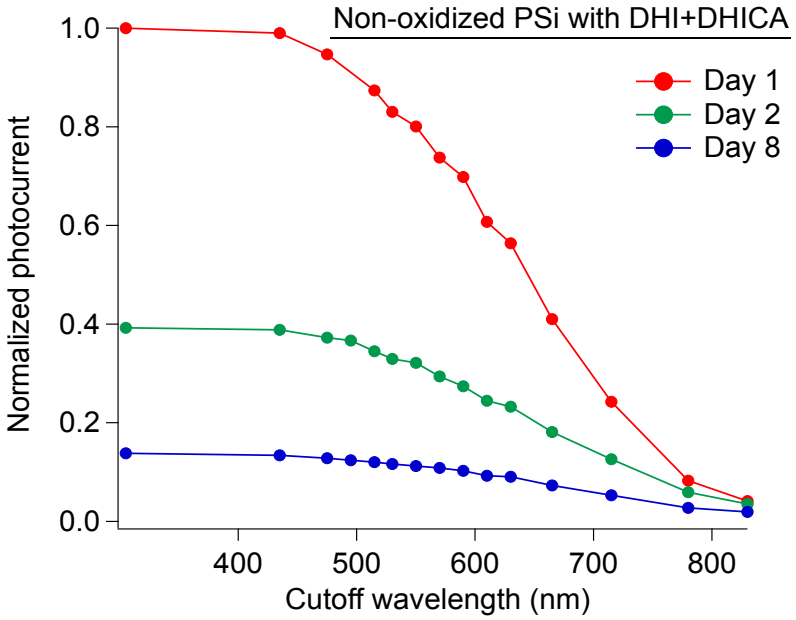

Figure 5.3: *Normalized photocurrent measurements on one PSi sample filled with a mixed solution of DHI and DHICA, obtained in three different days.*

the modification of the organic part of the junction. In particular, a solution containing DHI and DHICA in equal parts was used to impregnate the PSi matrices. The reason at the base of this choice was once again to improve the chemical bonds between the two parts of the hybrid junction. Since DHICA has a molecule similar to DHI but with a carboxylic group $-COOH$, this additional part can act as an anchor with the porous walls through oxygen bridges, as it happens in other hybrid photovoltaic systems [114]. The typical behaviour of the samples impregnated with the DHI/DHICA mix is presented in figure 5.3.

Despite the expectations, the addition of DHICA to the monomer solutions did not lead to a stabilization of the junction. The only difference with respect to the case of the standard sample was the slight improvement in long term photocurrent values: after eight days from the sample realization, it was possible to measure low but not zero photocurrent, as was the case of oxidized samples (figure 5.2). Once again, even if the parameter we modified shows

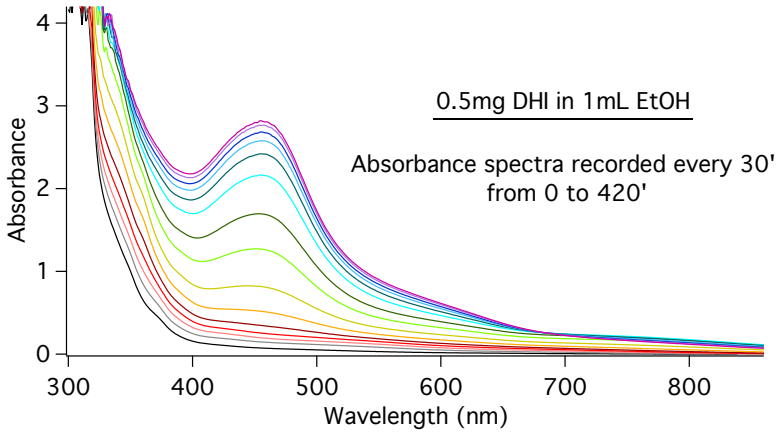

Figure 5.4: *Absorbance spectra evolution of a solution made with* 0.5 mg *of DHI dissolved in* 1 mL *EtOH.*

some positive effect on the improvement of the junction photovoltaic lifetime, it still does not give a strong indication of being a key parameter.

Since the two parameters we checked did not give satisfactory results in terms of lifetime improvement, it was evident that we needed to resort to a wider strategy to solve the issue. We therefore decided to investigate the polymerization process using a combined experimental and computational approach. This part has been done in collaboration with two computational groups of the Physics Department of the University of Cagliari: the team of G. Cappellini contributed to the understanding of melanin optical properties, while L. Colombo's group studied its electronic and structural characteristics. Polymerization of DHI is still a matter of debate and many research groups are working on deciphering the chemical structure of the eumelanin molecule that is formed during polymerization [115–120]. In the optic to shed light on the DHI polymerization process, the evolution of the absorbance spectra of an air-equilibrated solution of DHI in EtOH was measured and compared with the absorbance simulated spectra of several tetramers that literature reports as the most probable models for the polymerization of DHI.

In particular, the absorbance of three different concentrated solutions was studied:

- 0.25 mg DHI dissolved in 1 mL of EtOH
- 0.50 mg DHI dissolved in 1 mL of EtOH
- 1.00 mg DHI dissolved in 1 mL of EtOH

and the spectra were recorded every 30 min from the preparation of the solution to 420 min, except from the third one that was studied for 360 min because the absorption was very strong from the beginning and made impossible to record absorption spectra for delays longer than 360 min. Since the evolution of the absorbance spectra was the same for all the different concentrations, it has been decided to report here only the absorption spectra of the 0.5 mg mL^{-1} concentrated solution, because it has the best signal-to-noise ratio (figure 5.4). In order to emphasize the absorbance evolution of the different peaks, the absorbance variation at three different wavelengths was studied (figure 5.5):

- 330 nm, that is the position of a shoulder in the UV range;
- 460 nm, that is the position of the most visible peak;
- 780 nm, that is the position of the broad peak in the NIR range.

In particular, in figure 5.5 (a) the absorbance variation with respect to its initial value at the given wavelength and normalized with respect to the maximum increase for each curve is reported; in figure 5.5 (b) is shown the absorbance increase in each step, normalized with respect to the maximum positive value for each curve. From the analysis it is clear that the peaks at different wavelengths have different behaviours: the band at 330 nm increases faster than the other two, and the peak at 780 nm reaches its maximum and starts to decrease while other bands are still increasing. Moreover, if the peaks at 330 nm and 780 nm reach their maximum approximately at the same time, the peak at 460 nm reaches its maximum a little later. This evolution can be associated to the polymerization process of the DHI that is occurring in the ethanoic solution.
To better understand these results, it is useful to make a comparison with what is reported on reference [120] about DHI polymerization in aqueous buffer:

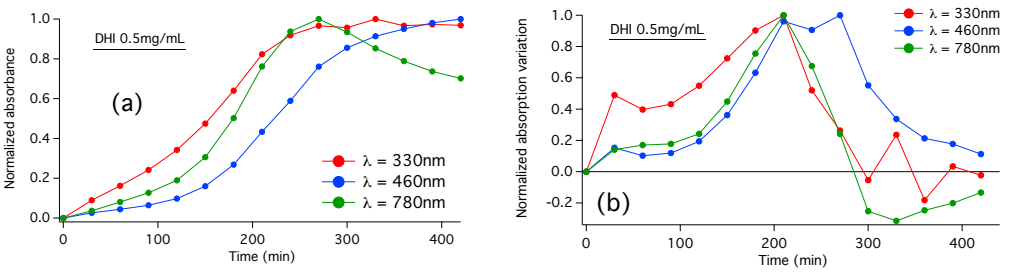

Figure 5.5: *Analysis of the absorbance evolution for three different significant wavelengths. (a) Normalized absorbance evolution. (b) Absorbance increase every* 30 min*, normalized to the maximum positive value for each curve.*

under such condition, during the polymerization of DHI there is the formation of broadly visible chromophores at around 560 nm, that was attributed to a mixture of dimers or higher level oligomers. In the same way, it is possible to say that the three bands shown in the experiments reported herein correspond to the formation of dimers or oligomers from the DHI monomers. Then, we can conclude that DHI polymerizes also in an air-equilibrated organic medium and that there is the formation of some more defined chromophoric species with respect to the same process in an aqueous medium. It could be possible that the species that absorbs at 780 nm is an unstable precursor of the one that absorbs at 460 nm, but no further experiments have been done to demonstrate this hypothesis. The fact that the main chromophore persists more in ethanol than in water could be related to the stronger solvation effects in organic solvents, which limits the aggregation and precipitation of dark material.

The experimental results have been compared with tetramer models that have been taken from literature as the possible molecules that form during the polymerization of DHI. Actually, the possible variety of isomers that populate each oligomer level is extremely wide [54,57,121,122], and they can also differ in their redox state. This means that, for each DHI monomer unit, it can exist the catechol form as well as the 2-electrons oxidation state (5,6−indolequinone, IQ) and its tautomers, the quinoneimine (QI) and the quinonemethide (QM) [123]. The structural variety of the molecules contributes to the molecular disorder of

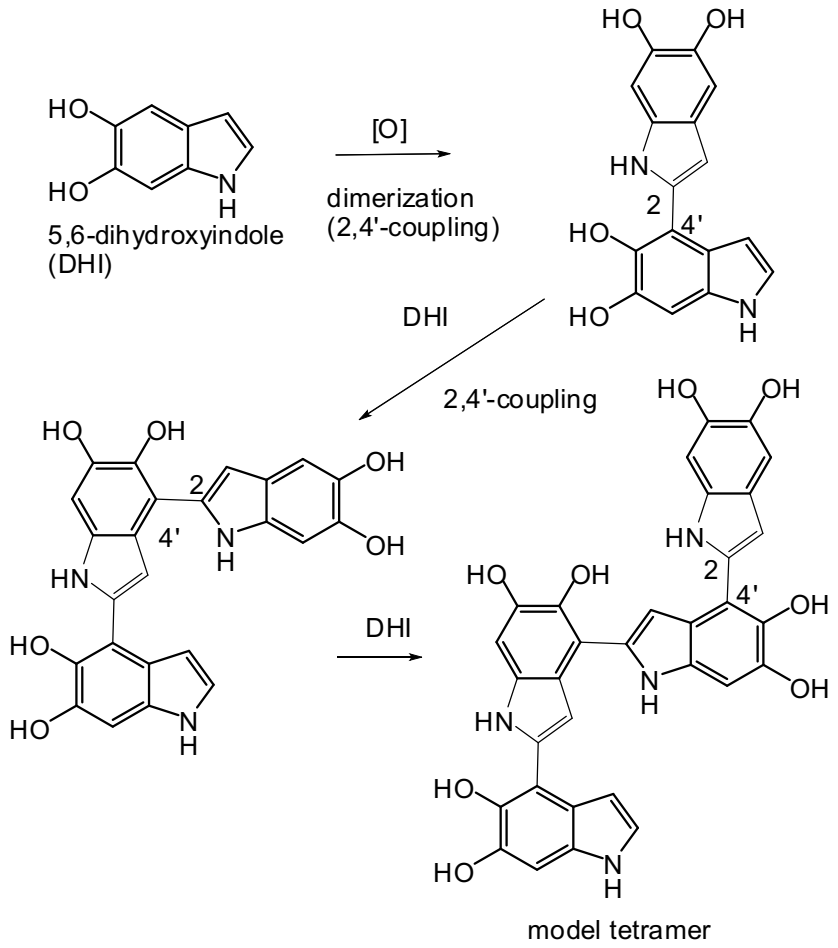

Figure 5.6: *Polymerization scheme where the oxidative coupling of DHI leads to isolated 2,4' dimer and 2,4':2',4" trimer and model tetramer (Model 1) [60].*

eumelanin, while the different oxidation levels of each molecule contribute to its electronic disorder. Since disorder from both molecular and electronic origin contribute to the overall properties of eumelanin, disorder control is a good approach to gain control over the eumelanin polymerization process [122]. The model tetramer used for the computational part of this research is 2,4':2',4":2",4'"-tetraindolyl (Model 1) and the polymerization path that brings to that model is reported in figure 5.6.

According to this scheme, the formation of the final tetramer is the result of the progressive coupling of a DHI monomer with the 2,4'-dimer, obtained by

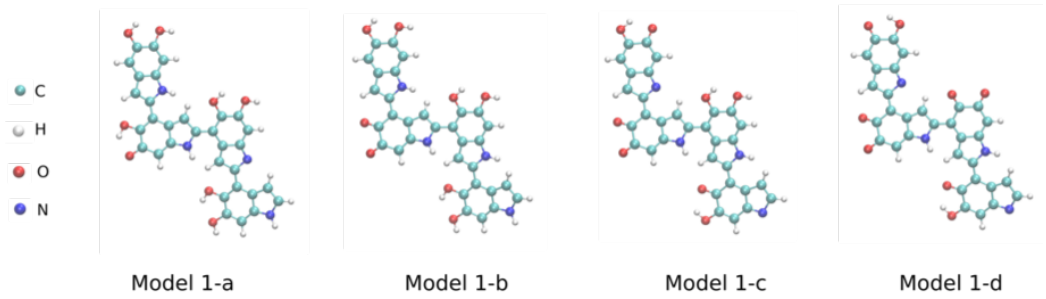

Figure 5.7: *Different oxidation states of the model tetramer called Model 1. The characteristics are the following: Model 1-a (2-electron oxidation, 1 C=O group); Model 1-b (2-electron oxidation, 2 C=O groups); Model 1-c (6-electron oxidation, 4 C=O groups); Model 1-d (8-electron oxidation, 6 C=O groups).*

the oxidation of the monomer, and then with the 2,4':2',4"-terindolyl trimer. Among the possible tetramers proposed in literature for eumelanin building block, it has been chosen Model 1 as the result of a compromise between the need for a sufficient level of molecular complexity and the computational costs associated with higher oligomers. Moreover, the absence of specific symmetry properties and its origin from major isolated DHI-based oligomers have been considered to make this choice. Density-Functional Theory, using the plane-wave Quantum Expresso package with the PBE (Perdew, Burke and Ernzerhof, [124, 125]) exchange correlation function, has been used by L. Colombo's group to investigate the formation and stacking energies of Model 1 as a function of its oxidative states (figure 5.7). The four different oxidation states correspond to two tautomers of the putative two-electron oxidation product, one tautomer for the six-electron oxidation product and one tautomer for the eight-electron oxidation product.

The formation energies and the stacking energies of all the four molecules have been calculated in vacuum and for two different solvents, where the choice of methanol as a solvent was guided by the need to be closer to the experimental condition of dissolving DHI in ethanol. The results are reported in table 5.1.

	Formation energy (eV)			**Stacking energy** (eV)		
Model	vacuum	methanol	water	vacuum	methanol	water
1-a (one =O)	-0.56	-0.12	0.67	-1.52	-1.08	-0.89
1-b (two =O)	-0.26	0.35	0.74	-1.22	-1.01	-0.78
1-c (four =O)	-1.20	-0.07	0.92	-1.75	-1.22	-0.88
1-d (six =O)	-1.46	-0.20	0.91	-2.01	-1.76	-1.21

Table 5.1: Formation and stacking energies of tetrameric Model 1 in the four oxidation states of figure 5.7 and for three different environments (vacuum, methanol and water).

Formation energies (FE) have been calculated as the difference between the tetramer energy and the sum of the monomeric energies, according to the formula 5.1:

$$FE = E_{tetramer} + 3E_{H_2} - \sum_{monomer} E_{monomer} \tag{5.1}$$

where E_{H_2} is the energy of the molecular hydrogen released in the reaction. The results show that formation energies in vacuum are always lower than in solvents and that they vary depending on the solvent used as polymerization environment, taken into account by considering the dielectric permittivity of the medium. In particular, a decrease of molecular stability when passing from methanol ($\epsilon = 32.7$) to water ($\epsilon = 80.1$) has been found, so that one structure is not stable in methanol and none of them is stable in water. Stacking energies (SE) have been calculated because stacking is the hypothesized aggregation method for DHI polymerization to form the final eumelanin molecule. Using formula 5.2:

$$SE = E_{2tetramers} - 2E_{singletetramer} \tag{5.2}$$

negative values have been found for every model and for all the environments, demonstrating that these molecules naturally tend to bind to each other via $\pi - \pi$ stacking. Moreover, the adhesion energy (AE) on a flat (100)-oriented silicon surface has been calculated for the Model 1 in the four oxidation states, according to the formula 5.3:

$$AE = E_{system} - \sum_{components} E_{components} \tag{5.3}$$

where E_{system} and $E_{components}$ are the energy of the composite system and the energy of the single components (non-interacting surface and molecule), respectively. The results are reported in table 5.2 and, once again, the higher is the number of C=O groups, the stronger is the adhesion between the molecule and the Si surface, probably because there are a more efficient π-electron overlap and a greater polarization by resonance effects.

	Adhesion energy (eV)
Model 1-a (one C=O)	-5.37
Model 1-b (two C=O)	-6.73
Model 1-c (four C=O)	-7.85
Model 1-d (six C=O)	-10.99

Table 5.2: Adhesion energies of tetrameric Model 1 in the four electronic configurations of figure 5.7.

Since for Model 1-d the lower stacking energy has been obtained, it means that the higher is the oxidation state of the molecule the higher is the probability of stacking during the polymerization process, at least among the oligomers that have been analyzed in this research. For this reason, Model 1-d has been also used to calculate the absorption spectra to be compared with the experimental curve and to understand if structures related to the model tetramer may be responsible for the optical behaviour of DHI oxidation reported in figure 5.4. The comparison between the experimental absorption data for DHI polymerization in EtOH and the calculated one for Model 1-d is presented in figure 5.8.

Even if at first sight the appearance is strongly different, some common features must be evidenced. Unfortunately, the maximum peak found for Model 1-d does not correspond to a maximum in the experimental absorption, but the affinities are several. First of all, Model 1 exhibits three peaks at very close wavelengths to the three peaks previously taken into account for

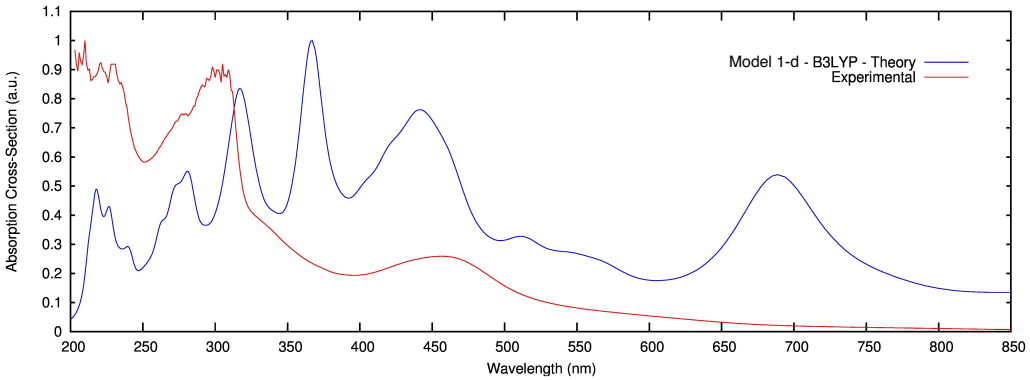

Figure 5.8: *Comparison between calculated spectra for Model 1-d (blue line) and the experimental absorption of a* $0.25\,\mathrm{mg\,mL^{-1}}$ *ethanoic solution of DHI (red line) after* $600\,\mathrm{min}$.

the analysis of the absorbance evolution with time, even if the intensities are not in the same proportion. Moreover, the spectral shape of Model 1-d in the UV and in the central part of the visible range is very similar to the experimental one. In table 5.3 is reported a more detailed list of the local maxima, minima, and shoulders found in the experimental curve and in the calculated one for Model 1-d. Furthermore, these results are compared with those of one of the most studied hypothetical model porphyrin-type cyclic tetramer (PT) proposed by Kaxiras and coworkers [126, 127], in order to validate the computational methodology.

N.	Exp. (nm)	Model 1-d (nm)	PT (nm)
1	210 (LM)	217 (LM)	213 (LM)
2	220 (LM)	226 (LM)	220 (S)
-	-	-	226 (Lm)
3	230 (LM)	238 (LM)	240 (LM)
4	250 (Lm)	249 (LM)	259 (LM)
5	277 (S)	263-275 (S)	270 (LM)
6	298 (LM)	281 (LM)	292 (S)
-	-	292 (Lm)	305 (Lm)
7	305 (LM)	317 (LM)	319 (LM)
8	322 (S)	330 (S)	325 (S)
9	340 (S)	340 (S)	340 (S)
-	-	367 (LM)	355 (Lm)
-	-	-	384 (S)
10	400 (Lm)	392 (Lm)	-
-	-	-	410 (LM)
-	-	-	453 (Lm)
12	456 (LM)	445 (LM)	-
-	-	-	485 (LM)
13	500 (S)	511 (LM)	-
-	-	-	550 (S)
14	612 (S)	575 (S)	617 (LM)
15	700 (S)	690 (LM)	700 (S)
-	-	-	800 (LM)

Table 5.3: Comparison of the position in wavelength of the main structures of the absorption curves studied in this dissertation: the experimental data (Exp.), the absorption of Model 1-d and the one of the porphyrin-type tetramer (PT). In the table, "N." stands for the ordinal of the spectral structure, "LM" stands for local maximum, "Lm" stands for local minimum and "S" stands for shoulder.

Considering a certain degree of tolerance in identifying the position of the peaks, 14 out of 15 possible matches have been found between the experimental data and the Model 1-d, while only 6 correspondences have been found for the PT model. This point is very important because it allows to support the hypothesis that Model 1 tetramer could be one of the possible final molecule derived by DHI polymerization [128].

The modern investigation techniques and the complexity of the materials

involved do not allow to look more deeply at the interface of the PSi-melanin heterojunction. To make up for the absence of experimental techniques, the polymer behaviour at the interface with a Si surface has been studied with a computational approach by our collaborator of L. Colombo's group of the University of Cagliari. The aim of the computational study was to elucidate how the interface affects polymer structural features, reaching an atomic resolution that is hardly obtainable in experiments. The computational technique that has been adopted is the model potential molecular dynamics (MPDP), since it allows the analysis of the adhesion of eumelanin on silicon, building a realistic system of tens of nanometers. Starting from the results obtained in the analysis of the process of formation and adhesion of a single tetrameric molecule on silicon with different oxidation states reported above, the following study is focused on the two tetrameric protomolecules with the best formation and adhesion energies. The two molecules, shown in figure 5.9 and mentioned hereafter as model 1 (left side of Figure 5.9) and model 2 (right side of Figure 5.9), are respectively the experimentally characterized molecule from Panzella et al. [128] and the structure from Kaxiras et al. [126]. The model 2 has never been isolated experimentally, but it has been used here as a representative example of a possible flat oligomer in the eumelanin polymer, as opposed to the linear and more flexible model 1.

The analyzed physical system was formed by a silicon (100) 25×25 substrate and a number of 5400 protomolecules of either model 1 or model 2. The atoms were 311 600 in total for each sample. At first, the molecules were randomly placed in a region above the substrate and then let them move toward it with an initial velocity of $0.001\,\text{Å}\,\text{fs}^{-1}$. The system was then let to evolve for 106 time-steps until all the molecules were deposited. Finally, a further 106 time-steps constant-temperature run was performed in order to estimate the system stability at finite temperature. During this last step, the density profile and root-mean-square displacement were sampled. This multi-step approach is intended to reproduce the experimental spin coating procedure used to generate uniform hybrid films [129], that we used also in this dissertation (section 4.2.1). The substrate temperature was kept at room

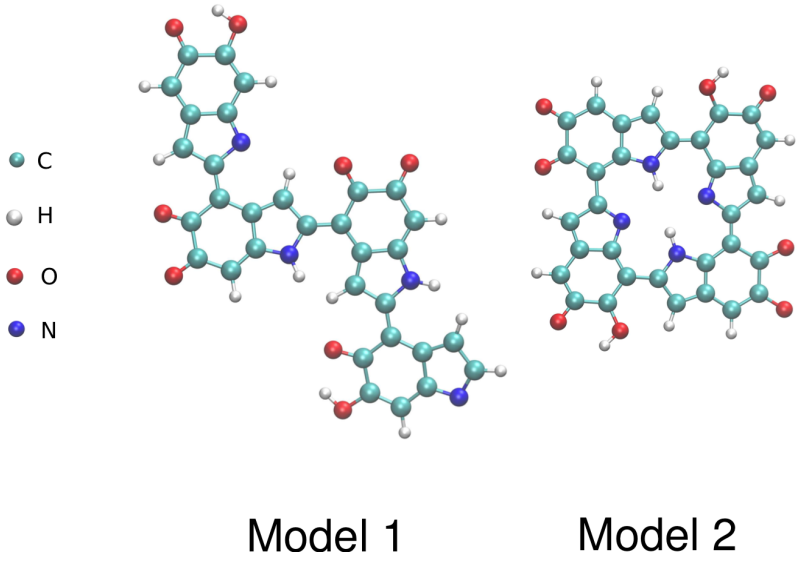

Figure 5.9: *Eumelanin tetramers used for the computational study: Model 1, on the left, taken from [128], and Model 2, taken from [126] works.*

temperature (300 K), and the silicon layer was fixed in order to mimic an infinitely deep substrate. An image of the two studied systems is shown in figure 5.10.

To prove the samples stability, the root-mean-square displacement of the molecules with respect to the substrate obtained at the end of the stabilization of the system has been calculated for each model. In both cases, an almost constant value is quickly reached: this demonstrates the overall stability of the system at 300 K at least for 500 ps, that is probably due to the combination of the strong covalent bonding between the single molecules and the substrate and the strong dispersive intermolecular attractive interaction. In particular, the surface coverage was estimated to be larger than 75% in both cases, and the average distance between adjacent molecules was around 0.32 nm. Besides sample stability, the possible effect of the Si substrate on the final polymeric film has been investigated by calculating the polymer density as a function of the distance from the silicon interface. The results are reported in figure 5.11: continuous lines are the calculated densities for the two analyzed samples, while dotted lines correspond to the mass density equilibrium values

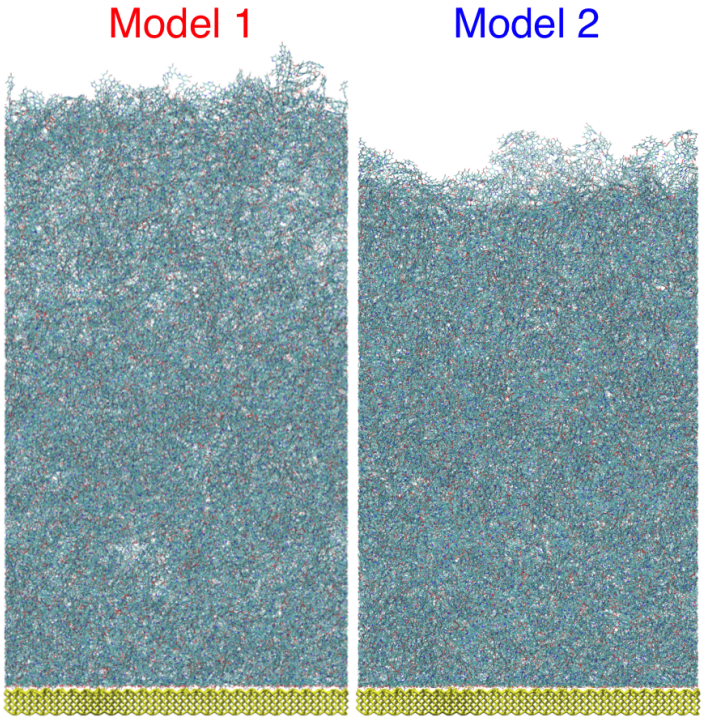

Figure 5.10: *Schematic representation of the eumelanin-silicon interface formed upon the deposition process described in the text.*

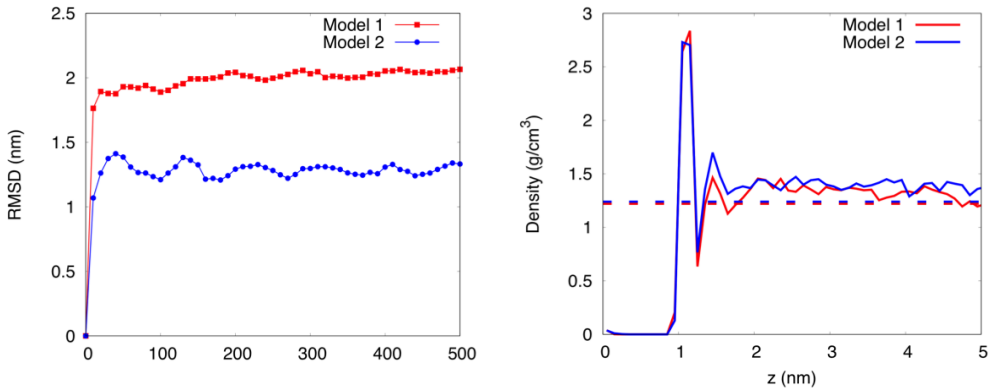

Figure 5.11: *Time evolution of the root-mean-square displacements for the two models considered (left-side); polymer mass density profile as a function of the distance perpendicular to the interface where $z < 1.2\,nm$ corresponds to the silicon substrate (right-side).*

without the substrate. From the graph it is visible that polymer density increases dramatically for $z < 1.3\,\text{nm}$, which is close to the silicon substrate: it is probably due to the strong interaction between molecule and substrate. For $1.3\,\text{nm} < z < 5\,\text{nm}$, the density is generally larger than bulk, and this means that the presence of the silicon substrate unavoidably affects the local properties of the polymeric film in a non-negligible spatial region as large as 4-5 nm beyond the interface.

The pores of the standard samples have an average diameter in the range 10-15 nm; according to the computational results shown in figure 5.11, then, the majority of the polymer volume inside the pore is strongly affected by the silicon interface. The comparison of the computational results with the characteristics of our samples is important to find a possible explanation for the fast degradation that we showed above in terms of photocurrent production. This phenomenon could have origin in the polymerization of DHI inside the pores. It is known that, during the polymerization process, there is the production of hydrogen peroxide [130, 131]; unfortunately, the H_2O_2 is a strong oxidant for the Si surface, so it gradually transforms the pores inner surface in an insulating layer, decreasing and eventually stopping the photocurrent generation. Differences in the polymer density may affect

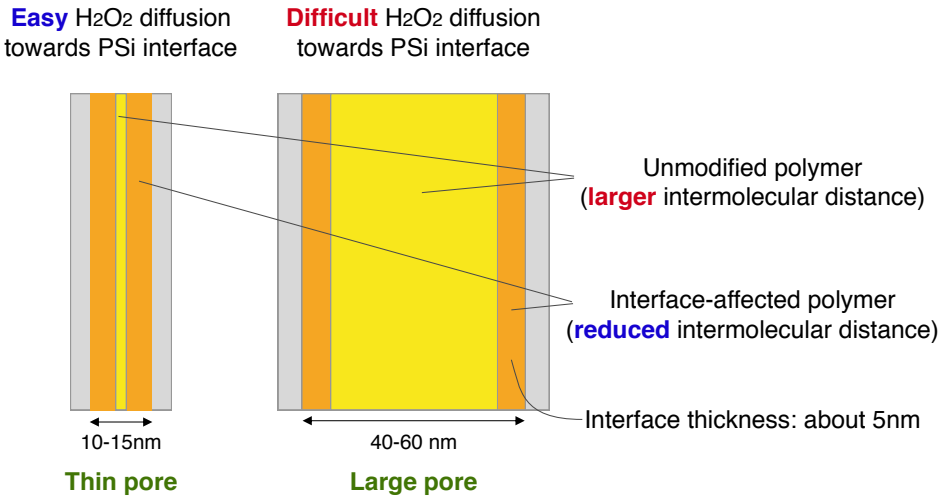

Figure 5.12: *Scheme of the different eumelanin structures within the silicon pores depending on the pores diameter.*

the H_2O_2 diffusion inside the pores during the polymerization process. If considering our standard samples, whose pores are quite thin, it could be that the hydrogen peroxide molecules diffuse quickly toward the interface between silicon and eumelanin. As a consequence, the oxidation of the silicon walls is fast and we observe it as a rapid degradation of the photocurrent properties. On the contrary, we can hypothesize that a significative increase of the pores diameter should modify the polymer behaviour. A schematic of the proposed interpretation of the polymer behaviour is shown in figure 5.12. For samples with larger pores, in fact, the diffusion of the H_2O_2 molecules toward the organic/inorganic interface may be slower, because they tend more to stay where the polymer density is lower. As a consequence, the oxidation of the silicon walls and the consequent degradation of the photovoltaic properties of the sample would be slower.

5.2 Electrochemical Nanolithography for larger pores fabrication

To verify the assumption that pores diameter would affect the polymer behaviour, we fabricated PSi samples with larger pores, and repeated the study on the stability of the samples impregnated with melanin made with thin-pores samples. Moreover, a porous structure with larger pores should improve the mobility of the solution and could help to improve the pores impregnation with the organic material. However, obtaining porous silicon samples with larger pores is not trivial, since pores diameter depends on the electrochemical parameters, like anodic etching current and HF concentration of the etching solution, but also to the Si doping level. Three parameters must be taken into account to fabricate larger pores. Besides pores dimensions, also a more regular porous structure would be important for our scope. For this reason, we started to think of a process to produce larger and less dendritic pores with respect to the standard samples and also to control pores order and size homogeneity. In reference [132] it has been demonstrated that increasing the formation current density of a single porous layer it is possible to increase pores diameter and to improve the pores size distribution (figure 5.13 a-b). At the same time, as much as the pores diameter increases, a parallel decrease of the pore-distance is registered, and if the crystalline Si skeleton is too thin, the electrical conductivity is too low to use this system for electrical applications. Moreover, the demonstrated improvement in pores size distribution is limited to a specific pores dimension.

Then, the simplest way to control pores size distribution for pores of different dimensions would be to fabricate a patterning of the top surface in a way similar to what lithography usually does. However, standard optical lithography has the physical diffraction limit of about 100 nm, that is above the mesopore range. Other techniques are usually used to obtain patterned samples in the sub-100 nm limit (e.g. electron beam lithography or focused ion beam lithography), but they are highly sophisticated and very expensive, so not easily accessible. Several works can be found in literature about surface

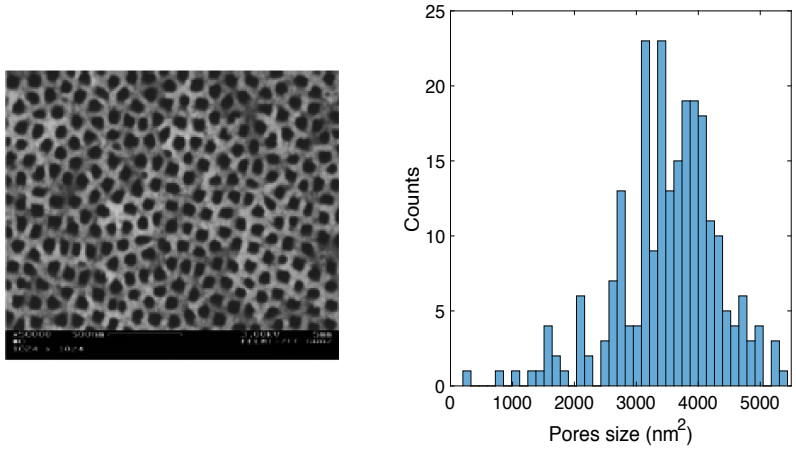

Figure 5.13: *Plane-view SEM image (a) and pores size distribution (b) of a PSi sample reported from reference [132]. The average pores diameter is around* 60 nm*, with a well-peaked distribution, but the pore distance is strictly linked to the formation electrochemical parameters.*

patterning using easier strategies, but all of them have some problems in scalability to large scale processes or in achievable precision. The use of polymeric nanoparticles [39, 133] or block-copolymers [39, 134], often used in combination with metal deposition followed by MACE [135] or with Reactive Ion Etching (RIE) [136], for example, are affected by problems related to the maximum achievable depth [137, 138] or to the difficulties in controlling the etching depth [139, 140]. Some other alternative ways to achieve a nanometric surface patterning can be an electrochemical process with the use of nanoelectrodes to reach a highly precise pattern [141], or the deposition of an aluminum layer for the formation of a lithographic patterning thanks to the porosification of the alumina layer on the surface [142]. The difficulties in the first case would be the need of a specific electrode for every different pattern, which makes it hardly scalable to large surfaces, while in the second case it is not obvious that the same method can be applied to pattern a surface of whatever material.

The idea of ENL was born from the need to find an easy and accessible way to pattern a Si surface, to control dimension homogeneity, order and

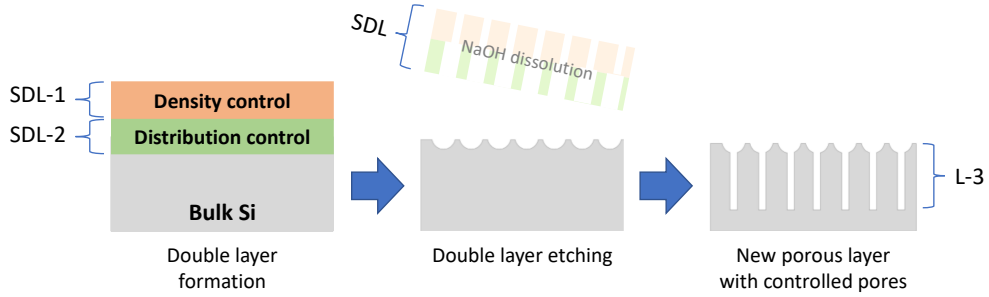

Figure 5.14: *Scheme of the ENL process.*

density of a final porous layer. At the base of this electrochemical process there is the evidence that Si etching starts from random surface irregularities, that are always present even if the surface is polished [38]. In fact, in those positions there is a local charge accumulation due to an enhancement of the local electric field, that permits the etching process to start. In analogy to what happens for the fabrication of macropores [143], the realization of an indentation pattern forces the pores to form from those sites.

A scheme of the complete ENL process is reported in figure 5.14: it consists in two electrochemical etchings that produce a sacrificial double layer (SDL) designed to control separately the pores density and size distribution in a third porous layer (L-3). The first layer (SDL-1) defines the pores density, since the number of pores of this layer depends on the random surface irregularities that are present on the surface. The second layer (SDL-2) is fabricated immediately under the first one. The number of the pores is the same as SDL-1, since they start from the bottom of the previous layer, but the electrochemical parameters are chosen so that SDL-2 pores are larger than SLD-1 ones. The reason of this choice is that the pores of the second layer are induced to re-arrange by the proper electrochemical parameters, and this influences their order and their size distribution. This double layer is then dissolved with aqueous NaOH solution, paying attention to not dissolve the bottom of the pores. In fact, we want to obtain a nanostructured surface whose microscopic defects serve as seeds for the formation of the pores in L-3.

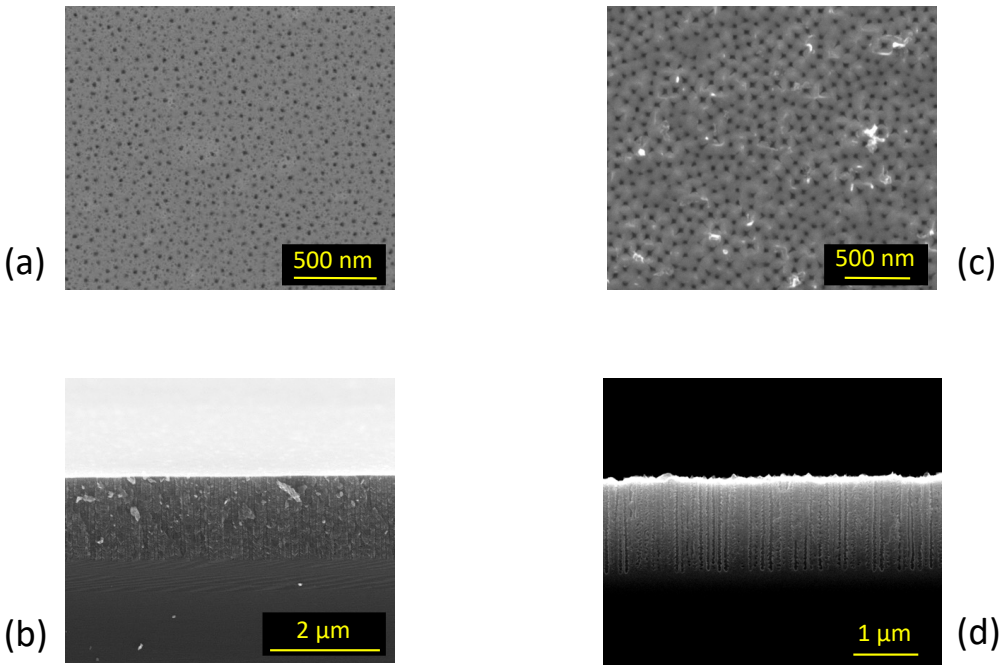

Figure 5.15: *Comparison between SEM images of a standard PSi sample (a-b) and the third layer of a sample obtained by applying the ENL process (c-d). In particular, top views are shown in (a) and (c) panels, while the cross sections are reported in (b) and (d).*

Before to demonstrate the details of the process, it could be useful to show a comparison between SEM images of a standard PSi sample (a-b) and a sample produced by using ENL (c-d) (figure 5.15). In particular, in top views (a) and (c) it is possible to observe the differences in pores order and in their dimension homogeneity, while from cross sections (b) and (d) the difference in pores structure is visible in their length.

SEM images, both in cross section and in plane view, have been used to analyze the ENL samples to demonstrate the power of the new fabrication technique as compared with the standard electrochemical etching. In particular, the plane views have been analyzed with the software ImageJ to demonstrate the ability of ENL to control pores order and their size distribution. Cross

sections, instead, have been used to measure the pores density, by counting all the visible pores on several images taken in different regions and with different magnifications. It was not possible to perform the same measurement on plane views because of the presence of several small openings that will not become pores, especially in case of standard PSi samples. The ImageJ analysis is done by modifying the image on a black/white one by adjusting the threshold image contrast so to separate one part of the image (the holes) from the other (the surface). Since the small openings and the pores have similar aspects on the images, different sets of parameters for the image analysis give different results and there is no possibility to obtain a coherent measurement. We were interested in measuring the pores density to demonstrate that the electrochemical parameters chosen to produce SDL-1 control the pores density of L-3, independently from SDL-2 formation parameters. As previously mentioned, the pore density of SDL-2 is tightly related to the pore density of SDL-1 because the former starts from the bottom of this latter. Given that L-3 formation starts from the surface indentations remaining from SDL-2 pores, L-3 pore density depends directly on SDL-1 one.

To demonstrate this property, a set of three ENL samples has been prepared: the electrochemical parameters have been kept the same for the second and the final third layers, changing only the formation conditions of SDL-1 in each sample. Moreover, a set of three standard samples has been prepared with three different current densities, so that a direct comparison with the ENL samples could be shown. The results are shown in figure 5.16: the red curve, referred to the left and bottom axes, represents the behaviour of the L-3 pores density as a function of the SDL-1 formation current density, while the blue curve (right and to axes) represents the behaviour of the standard samples. From this latter curve it is visible the well-known dependence of pores density on the PSi formation current density [132]; despite the different axes, a similar behaviour is shown also for the red curve. In both cases there is a decrease of the pores density when the formation current density increases: in fact, the higher is the current density the larger are the pores, and the only way to exist is to decrease their density since they occupy a larger volume. The

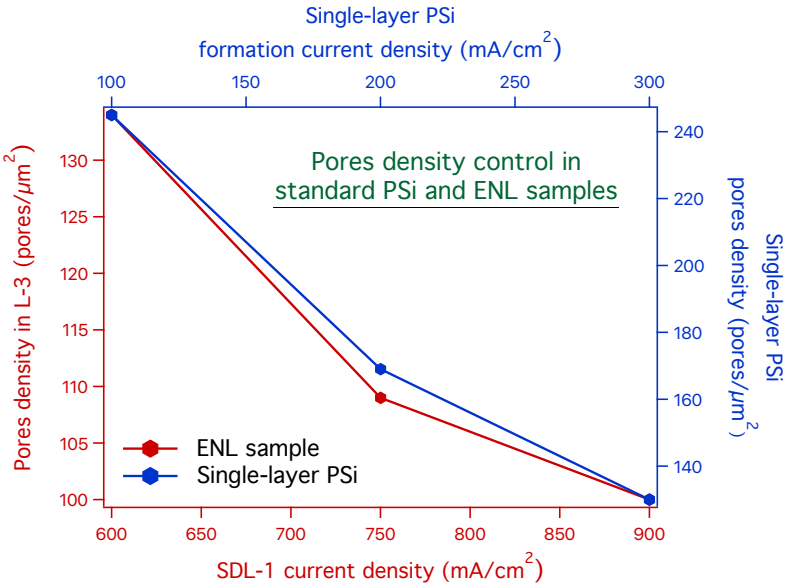

Figure 5.16: *Pores density evolution in standard PSi samples (blue curve and axes) and in ENL samples (red curve and axes). A similar behaviour is visible for both types of samples, with a clear dependence of pores density on the formation current density. The main difference is that different current densities make variations in the single porous layer produced in case of standard PSi, while for ENL samples the variation of the formation parameters in SDL-1 produces different pores density in the L-3.*

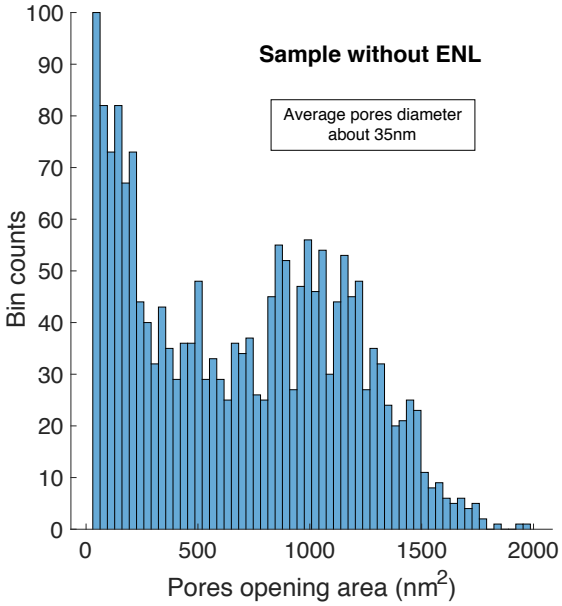

Figure 5.17: *Pores size distribution of a standard PSi sample.*

main difference between the two behaviours is that, if for standard PSi the variation of the formation parameters makes variations in the single porous layer produced, for ENL samples we vary the formation parameters in SDL-1 layer and we measure the different pores density in the L-3 layer. So we demonstrated our initial assumption.

Another characteristic of ENL is the control over the size distribution and order of the pores of L-3. In case of standard PSi samples, the average dimension of the pores depends on the formation current density, but the distribution is quite broad because there is unavoidably the formation of pores with much smaller or larger diameters with respect to the average value. In figure 5.17 there is an example of pores size distribution for a standard sample, where the average diameter is 35 nm but a bimodal distribution is visible, with a high number of small pores represented with the intense peak at around 100 nm^2. We can demonstrate that ENL allows a better control of pore-size distribution in the final L-3 pores. In reference [132] they demonstrated an improvement in size-distribution of the pores by increasing the formation current density, but it was tightly dependent on a specific pores

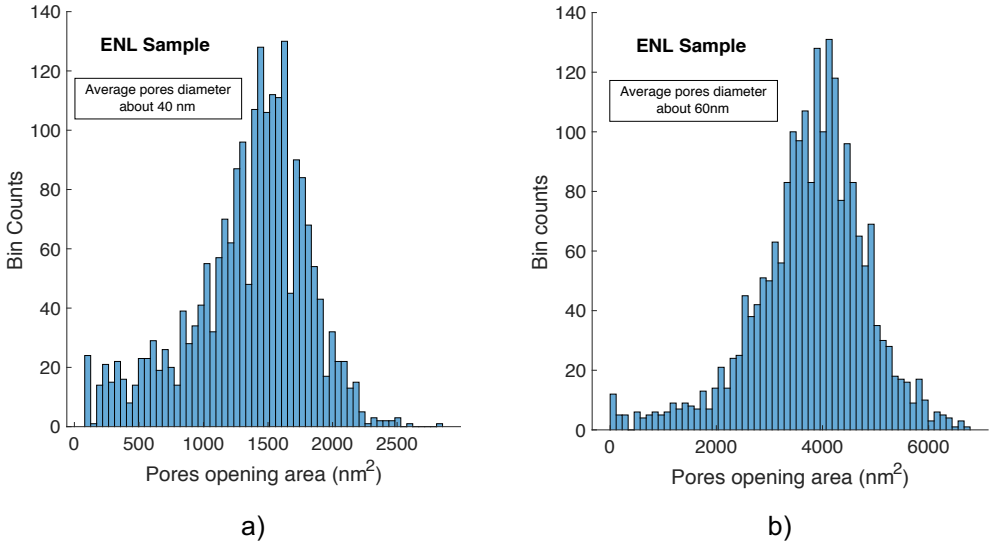

Figure 5.18: *Distribution of the pores opening size for two samples produced using ENL protocol. The samples have been fabricated with two different average pores diameter, about* 40 nm *(left) and about* 60 nm *(right), and they both show an improvement in size homogeneity with respect to standard samples.*

dimension (refer to figure 5.13). In this case we can demonstrate that ENL protocol allows to obtain a good pores size-distribution independently from pores dimension, that is on the specific L-3 formation parameters [144]. The histogram in figure 5.18 shows the size-distribution of two ENL samples with different pores average dimensions, obtained by changing the L-3 formation current density. If we compare the histogram of figure 5.17 with those of figure 5.18 we can notice that ENL allows to obtain a size distribution well centered on the average pores diameter, independently from pores dimension. The ENL surface patterning, then, prevents also the appearance of small-openings pores.

The choice of electrochemical formation parameters for SDL-2 has an effect on the order of the L-3 pores. To demonstrate it, a new set of samples has been prepared keeping constant the electrochemical formation parameters for SDL-1 and L-3 and changing the formation conditions for SDL-2 only.

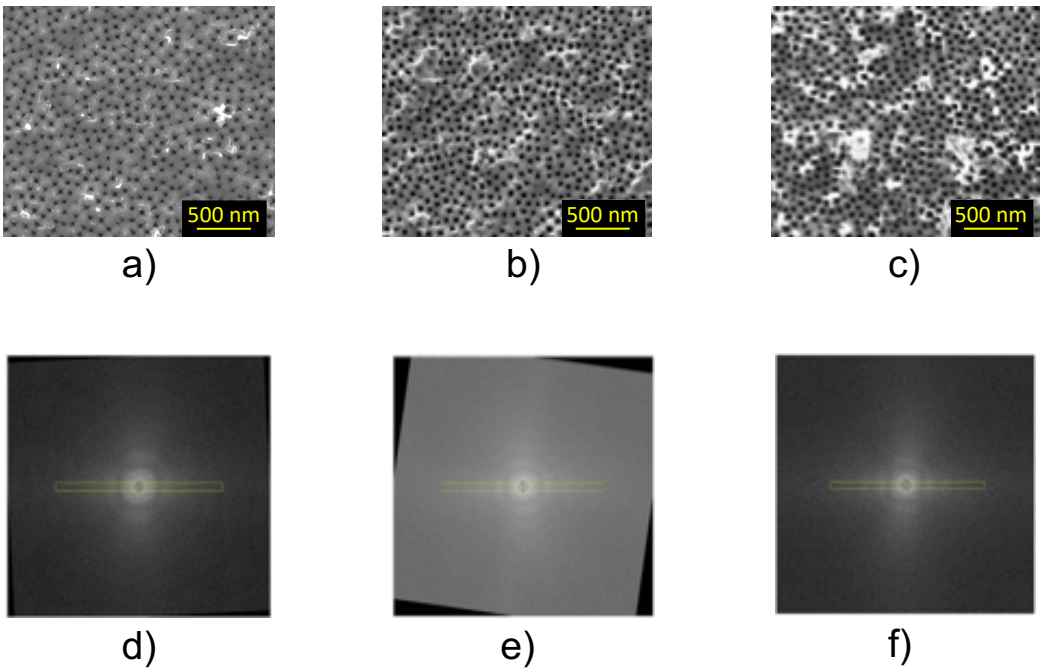

Figure 5.19: *SEM images (a-c) of three PSi samples prepared with identical formation parameters for SDL-1 and L-3 layers, but with increasing current density for SDL-2 from left to right images. In the same order as SEM pictures, the FFT images (d-f) are shown immediately below and have been calculated on squared areas of the respective SEM images. The yellow rectangles on the FFT images, identical for all samples, served to calculate the FFT profiles shown in figure 5.20. The FFT (e) has been rotated to align the rectangle and the order-related fringes appearing on the FFT images, so that all the analysis were coherent.*

In figure 5.19, the SEM images (a-c) of three ENL samples are shown, and the Fast Fourier Transform (FFT) images are reported in the panels below (d-f). The order of the FFT images corresponds to the order of the SEM images, and the three samples have been produced using formation current densities for SDL-2 increasing from left to right. The yellow rectangle on each FFT image, identical for all the samples, has been used to calculate the FFT profile shown in figure 5.20, in the same order as SEM images of figure 5.19. Our hypothesis is that increasing the pores diameter by increasing the formation current density leads to a higher order of pores morphology, due to a self-ordering effect. If this is true, higher levels of pores order correspond to a higher number of peak couples on FFT profiles, which represent the reproducibility of the interpore distance on the analyzed area. The black vertical lines on each profile of figure 5.20 indicate the most visible peaks: since their number increases with increasing the formation current density of SDL-2, we can state that our hypothesis is demonstrated.

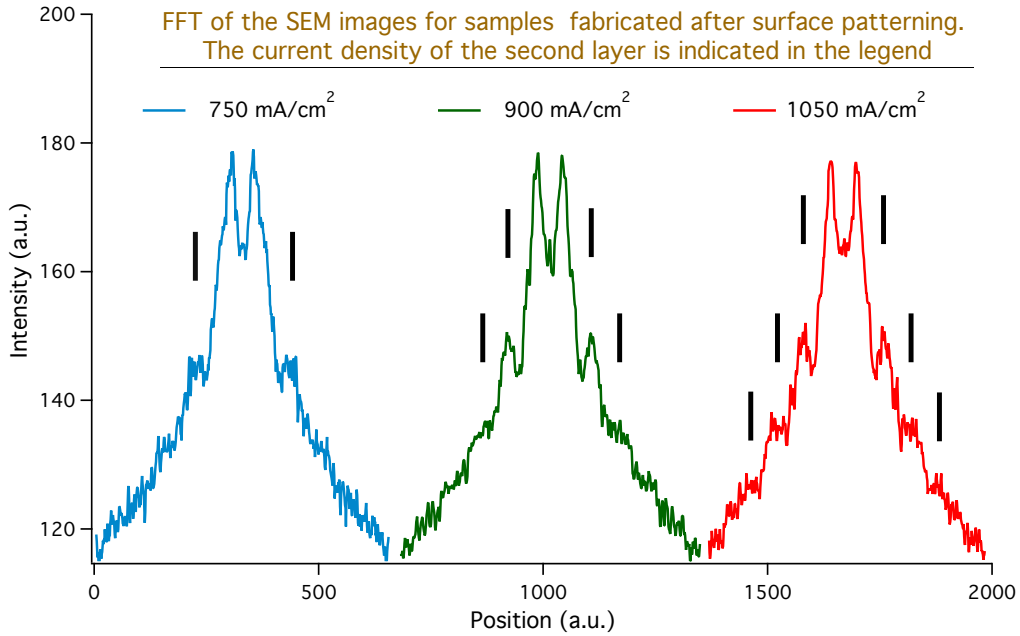

Figure 5.20: *FFT profiles obtained from the FFT images of figure 5.19, using the yellow rectangles, as described in figure 5.19 caption. The order of the curves is the same as the SEM images, and the formation current density of SDL-2 of each sample increases from left to right. The green and red curves have been translated along the x-axis for readability, while the blue curve is on its original position. The black vertical lines on each curve indicate the presence of clearly visible peaks, related to the pores distribution ordering.*

5.3 Large-pores samples with eumelanin

The new porous matrices produced by using the ENL process described in 5.2 have been used to be impregnated with melanin in order to investigate the effect of the pores size on the polymer behvior. According to the hypothesis made at the end of section 5.1, the polymer inside the pores should behave differently depending on pores dimension, and this could influence the temporal stability of the samples in terms of photocurrent production. The technical details of samples fabrication through ENL process are reported in section 4.1.1. The final step of samples fabrication has been a treatment with a diluted 0.1 M NaOH solution for 60 s in order to enlarge the pores diameter and reduce the surface asperities inside the pores: plane view SEM images reveal that there is an increase in the pores opening from about 34 nm to about 60 nm while, from the cross-section analysis, a reduction of the dendrites length is also visible after the NaOH treatment. The impregnation of the pores with the eumelanin solution has been done according to the procedure described in 4.2.1, and the effect of three different monomer concentrations has been investigated: $8\,\mathrm{mg\,ml^{-1}}$, $16\,\mathrm{mg\,ml^{-1}}$ and $24\,\mathrm{mg\,ml^{-1}}$. The lower concentration is the same that has been used in 5.1 for thin-pores samples, while the others have been chosen because the enlargement of the pores may affect the solution mobility and a new optimization of the impregnation process could be necessary.

In figure 5.21 are shown the first results obtained with the new PSi matrix: white-light photocurrent has been measured for several days for the ENL samples impregnated with three different DHI concentrations, and they have been compared with the white-light photocurrent produced by an empty sample and with that of a 10 nm-diameter sample impregnated with an $8\,\mathrm{mg\,ml^{-1}}$ concentrated DHI solution. First of all, no significant difference as a function of the DHI concentrations was noted, but an enhancement of the white-light photocurrent generation with respect to the empty and to the impregnated PSi with thinner pores is quite clear. Moreover, an improvement in the temporal stability of the samples is also evident, since photocurrent values after 10 days from the samples fabrication were more or

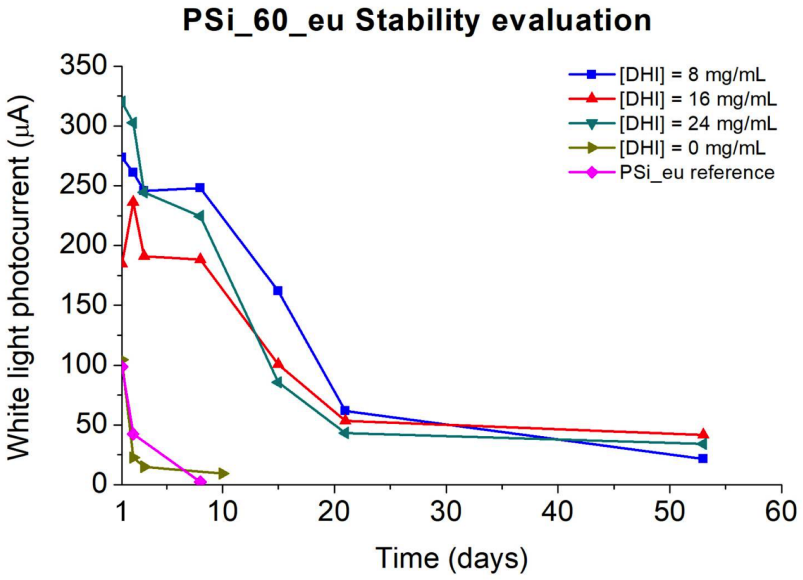

Figure 5.21: *Temporal evolution of white-light photocurrent of samples obtained with ENL procedure and impregnated using three different DHI concentrations:* $8\,\mathrm{mg\,ml^{-1}}$, $16\,\mathrm{mg\,ml^{-1}}$ *and* $24\,\mathrm{mg\,ml^{-1}}$. *These curves are also compared with the white light evolution of an empty PSi sample made with ENL procedure, and with that of a standard PSi sample impregnated with an* $8\,\mathrm{mg\,ml^{-1}}$ *concentrated DHI solution.*

less the same as the first day, differently from what happens in case of thinner pores samples (section 5.1). After a slower decay with respect to the samples with thinner pores, still measurable photocurrent values were recorded after 20 days, and they remain quite constant in the following weeks. Another significant improvement compared to the past is the reproducibility of the photocurrent intensity from sample to sample. As it is visible from figure 5.21, for large pores samples photocurrent values are independent of the details of the fabrication process and are very similar to one another, while for thin pores there were huge variations spanning over orders of magnitude (100 nA to 700 µA).

In figure 5.22 the spectral behaviour of the samples shown in figure 5.21 is reported, again measured for many days in order to observe the temporal evolution. The comparison with the spectral behaviour of an empty PSi

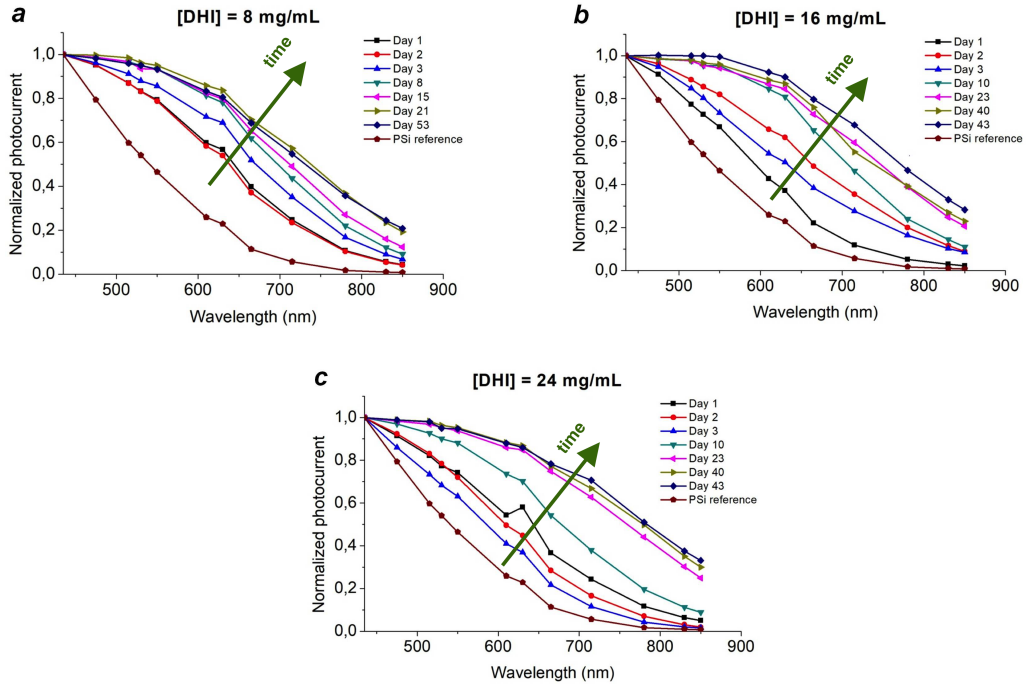

Figure 5.22: *Time evolution of the spectral behaviour of the samples impregnated with different DHI concentrations:* $8\,\mathrm{mg\,ml^{-1}}$, $16\,\mathrm{mg\,ml^{-1}}$ *and* $24\,\mathrm{mg\,ml^{-1}}$. *The spectral behaviour of an empty PSi matrix is also shown for reference in bordeaux in each panel, and the green arrows roughly indicate the evolution of the photocurrent spectra with time.*

sample is reported in each panel. As it is visible from these graphs, an increase of the eumelanin-induced spectral absorption is a common feature for all the samples, due to the polymerization of DHI inside the pores. The interesting characteristic, that is common for all the samples and that was not visible for samples with thinner pores, is that the effect of eumelanin seems to increase over time, as the green arrow indicates; moreover, the photocurrent generation stops to decrease with time and tends to stabilize after about 20 days. In analogy to what happens to the absolute photocurrent, also the stabilization of the spectral response occurs after about 20 days, as evidenced in figure 5.21. This stabilization was not observed for samples with thinner pores, so there is a clear dependence between sample characteristics and pores dimension. These results in terms of photocurrent stability demonstrate the accuracy of the hypothesis that we made thanks to the computational study on polymer behaviour depending on pores dimension (section 5.1). We can eventually state that the introduction of larger pores does improve the stabilization of the hybrid junction, because the H_2O_2 produced during the polymerization process diffuses slower toward the silicon walls with respect to thinner pores samples. This result is in agreement with other literature works that demonstrate the pore diameter dependence on the final properties of a porous device [145, 146].

5.4 MACE nanostructured porous silicon with eumelanin

One of the strategies for improving the efficiency of a photovoltaic device is the optimization of light absorption. The addition of melanin itself is aimed at enhancing the photoconductivity of the final device: its absorption properties, in fact, allow to increase the absorption coefficient for thin layers and this should, in principle, permit to reduce the final thickness of the photovoltaic device. Moreover, part of the light that impinges on a photovoltaic device is reflected by the surface itself, so it cannot contribute to the production of photovoltaic energy. Minimizing that loss, a larger part of the incident

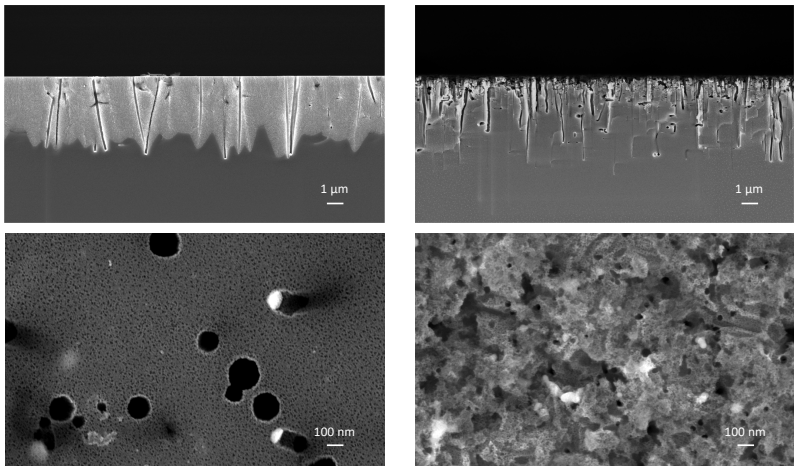

Figure 5.23: *SEM images in cross-section and plane-view of samples obtained by MACE using Pt (left-side) and Ag (right-side) metal nanoparticles.*

photons can be used to produce electron-hole pairs, and then also the efficiency of the device can be positively affected. Many research efforts are devoted to improve the anti-reflection properties of solar cells [147–152] and PSi itself has been studied also for that purpose [153–155]. Besides through electrochemical etching, PSi can be produced with an electroless technique called metal-assisted chemical etching (MACE), as explained in section 2.1.2.

Thanks to the fact that the interface between porous and bulk silicon assumes a very typical pyramidal shape, the reflectivity of these samples is orders of magnitude lower than the one of standard PSi obtained with the electrochemical etching. Combining together the antireflection properties of the MACE PSi samples with the absorption properties of eumelanin, it would be possible, in principle, to optimize the photovoltaic properties of such hybrid heterojunction and to produce thinner device. Present technology, in fact, is affected by the need of using thick layer of absorbing material to compensate the problem of indirect bandgap of Si, that limits its photovoltaic efficiency. In this paragraph, a preliminary study on the realization of a hybrid heterojunction made with MACE PSi filled with eumelanin is presented. This study has started in 2016 in collaboration with the group of S. Bastide

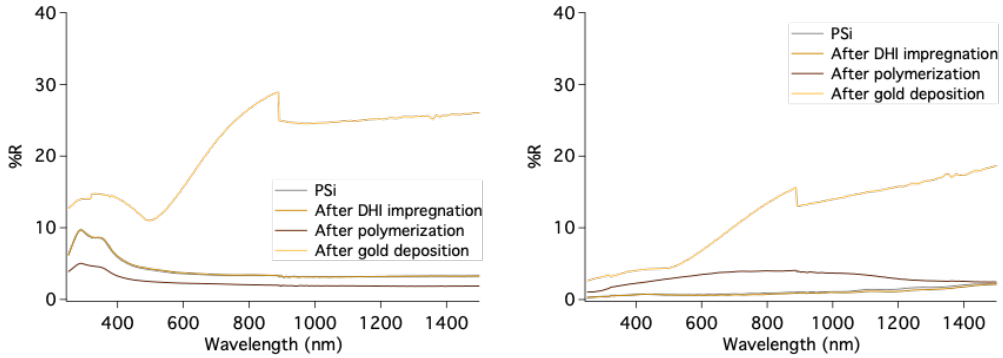

Figure 5.24: *Specular reflectivity of the different phases of the samples realization, both for Pt samples (left side) and Ag samples (right side).*

of CNRS-ICMPE in Thiais (France) and has culminated with my stage in those laboratories for four months in 2018; samples fabrication and their analysis with SEM has been done in France, while samples impregnation with melanin and their optical analysis have been performed both in Thiais and in Cagliari. Two different metal nanoparticles have been used as catalytic agents for MACE: silver and platinum. In figure 5.23 SEM images of the two types of samples have been presented, both in-plane view and in cross-section: left-side images are of a sample prepared using Pt nanoparticles as metal catalyst, while right-side images are of a sample prepared with Ag. Both types of morphologies have been studied, since it was not possible to know in advance which configuration would be better: Pt-samples have a flat upper surface but the diffused porosity among the nanoparticles channels is very narrow, so it could be a problem for the organic solution to penetrate; on the other hand, Ag-samples have more diffused larger pores, but the upper surface is very rough, and that could be a problem for the deposition of the gold contact on top.

All the samples have been impregnated according to the procedure described in 4.2.1 and have been analyzed with a UV-Vis-NIR spectrophotometer to monitor all the phases of the sample preparation: after the sample realization, after the impregnation with the monomer solution, after the polymerization process and after the deposition of the gold surface contact (figure 5.24). As

visible from these graphs, the polymerization process (dark brown curves) can have either the effect of decreasing (left case) or increasing (right case) the samples reflectivity with respect to the reflectivity of the sample freshly impregnated with the monomer solution (light brown curves). The decreasing of the reflectivity, reported in case of impregnated samples obtained with Pt nanoparticles, is an expected behaviour when an absorbing material like eumelanin is inserted in the PSi matrix. On the contrary, a possible explanation of the behaviour reported for the Ag samples could be related to the morphological aspect of the samples surface, that are more rough with respect to the surfaces of the previous samples. In this case, the flattening of the surface due to the deposition of the eumelanin solution could be the explanation of the increase of the sample reflectivity. The decrease of the sample roughness could be more relevant than the insertion of an absorbing material on the final optical properties. To verify the impregnation of the PSi matrix with the organic solution, the samples have been analyzed by SEM-EDS. The atomic percentage of carbon with respect to silicon has been measured at the top and at the bottom of the porous layer for both the matrices. The results are reported in table 5.4 and they show a typical gradient from the top to the bottom in the pores impregnation.SEM-EDS analysis showed good results that confirm the impregnation of the pores with melanin; however, it has not been possible to characterize the samples from the photocurrent point of view. In fact, even if a weak photocurrent response was visible for some of the samples, their values were too low and too noisy to be measurable and analyzed. One of the problems to be solved that prevents photocurrent measurements is the surface roughness, especially for samples made with Ag nanoparticles. This issue limited the possibility to deposit a thin and homogenous metallic layer as a top contact to collect the separated charges at the interface of the junction. With such a roughness, the percolation threshold to have a uniform gold contact on the top surface by sputtering is reached for a longer deposition time with respect to a flat surface.

	Pt sample		**Ag sample**	
	C (at.%)	Si (at.%)	C (at.%)	Si (at.%)
top	20,55	79,45	33,67	66,33
bottom	12,79	87,21	23,72	76,28

Table 5.4: SEM-EDS analysis of the MACE PSi samples filled with eumelanin, in order to verify the impregnation of the porous matrix with the organic solution. Data show a gradient in the presence of carbon from the top to the bottom of the sample for both the configurations.

A thick metal layer as a top contact implies an increase of the sample reflectivity, and so a decrease of the percentage of the light that arrives to the hybrid junction to produce excitons. An attempt with the deposition of an organic contact made of PEDOT has been done as well, but the high roughness prevented again its adherence to the sample top surface. In case of samples produced with Pt nanoparticles, which have a flatter surface than the previous ones, photocurrent problems cannot be related to the impossibility to fabricate a top contact. In this case, the problem could be related to the pores dimension: the pores that branch out from the channels formed by the nanoparticles have openings of few nanometers. Probably the monomer solution is able to penetrate the porous matrix through the large channels but not through the tiny pores, and this prevents the formation of a working hybrid junction between the two materials. Since this was a preliminary study, many aspects still need to be optimized. Future research on this material will include, for instance, optimization of the metal nanoparticle size and the etching parameters.

Chapter 6

Porous silicon impregnated with erbium

In this chapter, the results obtained on the study of PSi samples impregnated with erbium are presented. In particular, section 6.1 reports a little background on the previous studies on Er-doped PSi samples, where the limit in PL emission due to erbium clustering is highlighted. In section 6.2, instead, an alternative idea to overcome the erbium clustering issue and to enhance the Er-related PL emission is presented through a multidisciplinary study that involves electrochemical, morphological and optical techniques.

6.1 A little background on Er-doped PSi: photoluminescence intensity issue

PL production from pure silicon devices is prevented by the fact that silicon has an indirect bandgap; radiative recombination between an electron-hole pair in this type of semiconductor, in fact, can occur only in case of absorption or emission of a phonon. To overcome this limitation, hybrid silicon-based devices have been proposed [156], but they are generally quite complex and expensive solutions. Another possibility could be to exploit the PL emission of PSi, discovered at the beginning of the 1990s, probably due to quantum confinement effect on its crystalline structure [157, 158], or the doping of

PSi itself with rare earths. In fact, it has been demonstrated that rare-earth doped PSi structures can emit light at $\lambda = 1.5\,\mu m$ [159–165], that falls in the transparent transmission wavelengths window of silica optical fibers [166]. The origin of the erbium PL comes from electron intra-$4f$ transitions of the incomplete shell; this transition switches from forbidden to partially allowed when the ion Er^{3+} passes from the free ion state to being hosted in a non-centrosymmetric site [167–169]. Many efforts have been done in rare-earth doping of silicon structures [170, 171], including also the co-doping with erbium and ytterbium [172, 173], but unfortunately not enough high yield PL has been obtained so far [82, 174]. It has been demonstrated that erbium clustering plays a major role in preventing the production of efficient Er-doped luminescent devices. The alternative paths that have been followed by researchers to overcome this limit were either the use of erbium-doped Silicon Rich Oxide (SRO) structures [175–181] or the lowering the erbium doping levels [82]. Several works have been made on the study of the electrochemical doping of PSi samples [30, 83–86] in order to understand the origin of the low PL intensity. In particular, in reference [85] it has been reported that the evolution of the applied voltage of the electrochemical doping shows different shapes depending on the current intensity used to perform the process. More precisely, for low currents a single transient is evident, and the voltage absolute value monotonically increases as the process goes on; for higher currents, instead, a double transient appears in the voltage evolution, meaning that two different Er deposition processes are involved. The study of the initial phases of the electrochemical doping by means of GEIS (Galvanostatic Electrochemical Impedance Spectroscopy) permitted to propose a possible interpretation of this behaviour. Actually, two processes are induced by the applied electric field during Er deposition: one is the migration of the Er^{3+} ions present in the electrochemical solution towards the inner pores surface, the other is the transfer of the charge from the ions to the solid structure. When using high electric fields, which means high current values, the flux of the Er^{3+} ions is more intense and leads to a consistent ions accumulation near the PSi top surface up to the formation of a jelly-like layer. This does not happen in case of low doping current and

this difference can explain the different behaviours of the voltage evolution in the two regimes. Moreover, the applied current intensity also influences the final erbium content deposited on identical PSi samples, keeping constant the transferred charge. In fact, structural characterization of the samples with SEM-EDS microscopy permitted to measure the Er percentage, at various depths, in nominally identical samples doped with high (0.5 mA) and low (0.05 mA) current intensities. The measurements showed that the Er percentage in the first case (high current intensity) is higher with respect to what has been measured in the second case (low current intensity). Given the higher efficiency of the process in high current regime, this condition has been used to perform the study reported in this dissertation.

Starting from these discoveries, a more detailed study on the electrochemical doping process of PSi samples has been carried out and presented here. The first step of the study was the electrochemical impregnation of a PSi sample with an erbium quantity of around 1%. The sample has been fabricated according to the procedures reported in 4.1.1, while the impregnation of the pores with erbium has been done through the electrochemical process described in 4.2.2. The 1% doping level corresponds to the amount of erbium that is typically inserted in erbium-doped light-emitting PSi samples and for which erbium clustering appears. On such a sample, ET analysis has been carried out in Grenoble following the procedures described in 4.3.2. The results are shown in figure 6.1. Both in sagittal and in axial slices the erbium clusters are visible as white spots randomly spread on the walls of the pores. In fact, since ET is very sensitive to the atomic number Z, erbium appears much brighter than silicon because its Z is much higher than that of Si.

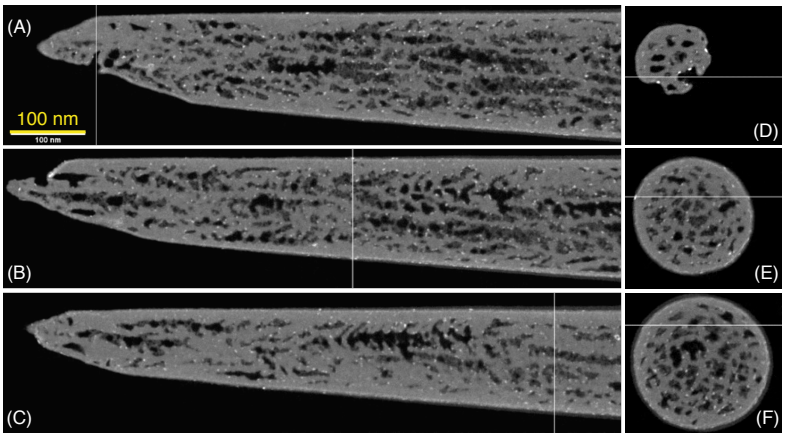

Figure 6.1: *ET images, both in sagittal slices and in axial slices, of an Er-doped PSi sample with an erbium percentage of 1%, calculated by SEM-EDS mapping. Axial sections are extracted in correspondence of the white lines reported in panels (A), (B) and (C); at the same way, sagittal images are taken in correspondence of the white lines of panels (D), (E) and (F).*

6.2 A new approach: pores filling for photoluminescence improvement

The scope of the work proposed here is to have a deeper understanding of the electrochemical doping process; in fact, the optimization of this crucial phase of samples preparation would permit to better understand the PL origin and to enhance the final properties of this composite material. The strategy that has been adopted here to overcome the erbium clusters issue goes in the opposite direction with respect to the idea proposed by Prtljaga et al. in reference [82]: instead of reducing the erbium amount to prevent the clusters formation, the strategy to greatly increase the doping quantity inside the pores has been explored. Several PSi samples have been prepared, following the electrochemical procedure described in 4.1.1, and then electrochemically filled with erbium in galvanostatic regime, as explained in 4.2.2, with doping levels of 1.2, 4.0, 6.0, 8.0, 10.0, 12.0% (table 6.1).

Er doping time (s)	Er concentration (%)
25	1
30	1.2
100	4
150	6
200	8
250	10
300	12

Table 6.1: Equivalence between duration of the Er doping and the Er concentration, measured through SEM-EDS for 1.3 µm thick samples doped using a constant doping current of 1 mA.

In figure 6.2, the voltage evolution for a 12% electrochemical doping process is presented. Three different transients in the voltage evolution are visible and indicated with green references in the graph: as already mentioned in reference [85], to each transient corresponds a different phase in pores doping process. To activate the Er-luminescence, in both crystalline [182,183] and PSi layers [184,185], a thermal treatment must be mandatory; in this case, samples have been subjected to an annealing process at 700 °C in N_2 inert atmosphere, with the scope to have an efficient Er activation without significantly changing the pores structure. In fact, if 700 °C is relatively low compared with the optimal temperature for PL performance of Er silicate and Er oxide [186,187], it is also good for preservation of the PSi matrix [188] and to avoid the induction of structures that would be similar to silicon-rich-oxide. Both structural and optical characterizations have been performed on the samples as a function of the erbium doping level, from 1.2%, that is the standard doping level also mentioned in the previous paragraph, up to 12%, that corresponds to a surface accumulation of Er ethanolate gel visible by naked eye.

Er-doped PSi samples have been characterized from the structural point of view in Grenoble by ET. In figure 6.3, ET images of two Er-doped PSi samples are presented: panels (A) to (F) refer to a as-prepared 1.2% doped sample, while panels (G) to (L) refer to an annealed 8% doped sample. In these

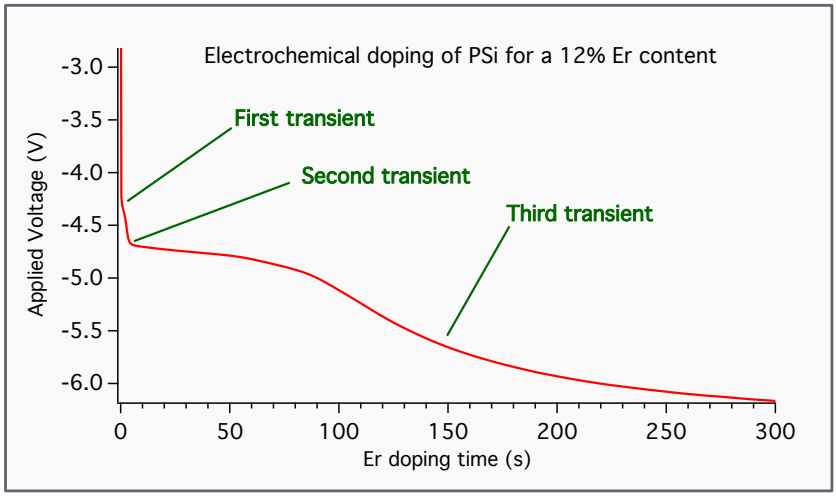

Figure 6.2: *Evolution of the applied voltage during the electrochemical doping of a PSi sample with erbium. The non-constant voltage evolution is a clear evidence of different phases in pores filling process.*

images, erbium appears as a white material and a decreasing gradient in Er concentration is visible from the top to the bulk silicon in both samples, in agreement with previous SEM-EDS measurements [83]. Especially in the first sample, some homogeneous nanometric Er clusters are visible on the pores walls, and they tend to aggregate and to form a continuous Er layer closer to the top surface. It is important to note that axial images show that some of the pores are completely empty, but this behaviour is similar to what has been observed for other electrochemical filling processes [189,190]. The same feature is visible for the sample with 8% but to a lesser extent. This second sample has, in fact, many pores completely filled up to a depth of 800 nm. Differently from the sample with 1.2% dopant, this sample is annealed, but the shape of the filled pores remained quite unmodified with respect to the structure of a not-annealed sample. This fact is in accordance with the hypothesis made before about the choice of 700 °C as annealing temperature, and it is remarkable because our aim was to study a PSi structure filled with Er-rich material, so it was important to avoid a complete diffusion of the Er into the crystalline Si matrix. Moreover, looking at the axial slices (B) and (H), some filled pores show a dark center: it means that the pore filling is a process

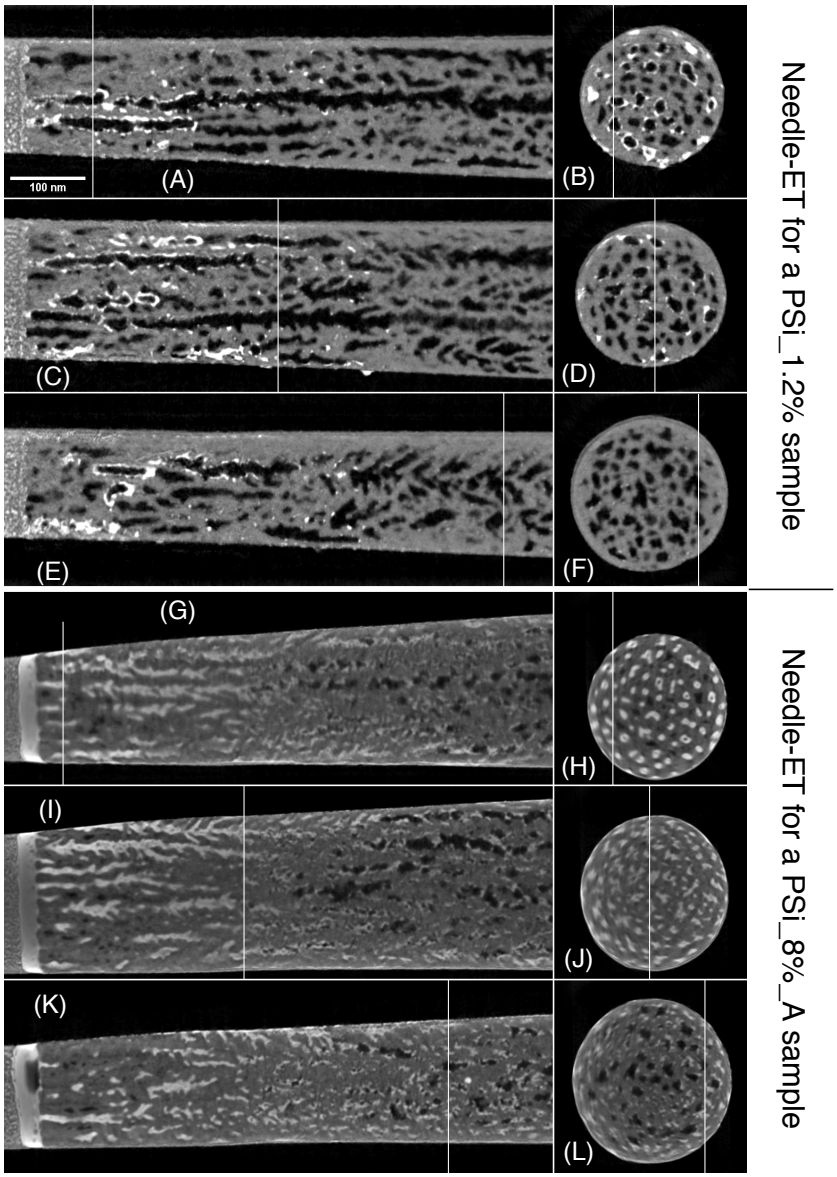

Figure 6.3: *ET of Er-doped PSi samples: panels (A) to (F) refer to a not-annealed* 1.2% *doped sample, while panels (G) to (L) refer to an annealed* 8% *doped sample. Panels on the left are different sagittal slices, while panels on the right are different axial slices in the 3D reconstructed volume. Localization of the sagittal slices is represented by a white line on the corresponding axial slices and vice versa. The top surfaces of PSi samples are on the left-hand side of the figure. The filling of the pores by the Er deposition is evidenced by the white signal from the PSi pores.*

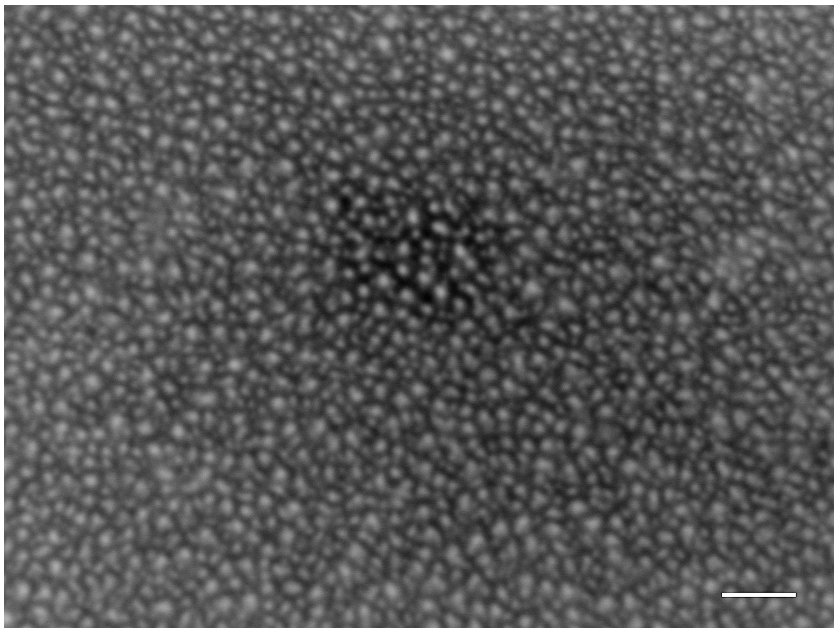

Figure 6.4: *SEM-BSE image of an annealed PSi sample with 8% Er.*

that starts from the pores surface and proceeds towards the center. This is an important information that permits to understand how the impregnation works and to give a better interpretation of the voltage evolution during the electrochemical doping. Another morphological characterization of these samples has been done by the group of A. Falqui at KAUST (Saudi Arabia) using SEM-BSE technique. In figure 6.4, a top view SEM-BSE image of an annealed PSi sample with 8% Er is reported and several things can be noted. Given the high sensitivity of SEM-BSE to the elements atomic number, the Er-filled pores appear like white spots, while dark spots are empty pores, in analogy with ET observations. Moreover, some areas with diffused brightness can be noticed, and these indicate a surface coverage that appears when most of the pores are completely filled.

The samples have also been analyzed in collaboration with the group of M. Saba of the University of Cagliari to explore their PL properties. In figure 6.5 are shown the PL intensity results for samples with different doping levels after the annealing treatment. Each spectrum is normalized with respect to the maximum intensity of the silicon emission ($\lambda < 1200\,\mathrm{nm}$) for easier

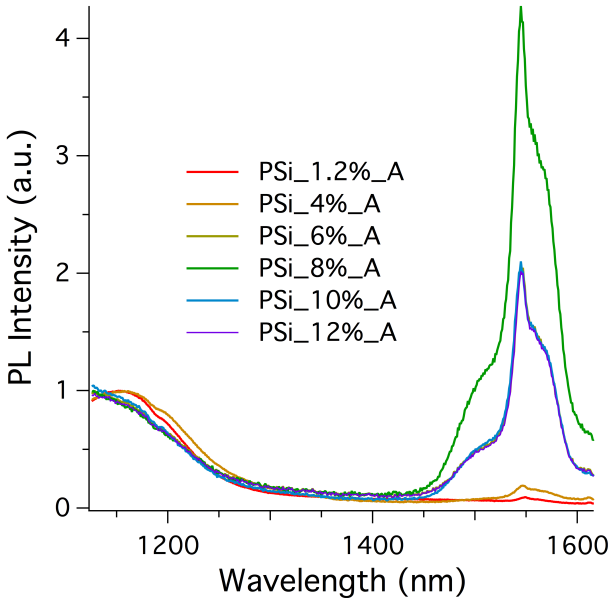

Figure 6.5: *Normalized PL results from annealed PSi samples with different Er content.*

comparison. Looking at the peak at $\lambda = 1540\,\text{nm}$, it seems that the higher is the Er content, the higher is the PL intensity. A maximum is reached for doping level of 8%, and then a slight reduction and saturation of the maximum PL value is observed for higher doping levels.

On the samples that showed a significant PL emission, time-resolved PL measurements have been also performed, again in collaboration with the group of M. Saba. These measurements have been performed on 6, 8, 10 and 12% after the annealing treatment and were intended to reveal any different optical properties of the composite material. The results are presented in figure 6.6: the red curve, that is referred to the sample with 6% Er, is characterized by two decay times: a faster one ($\tau_1 = 3.6\,\mu\text{s}$) and a slower one ($\tau_2 = 20\,\mu\text{s}$), and they have been obtained by fitting the experimental data with a biexponential curve. All the other samples have a single fast decay time quite similar to τ_1 and they are all characterized by an Er-rich film on the top surface, as demonstrated in [83]. The magenta curve, instead,

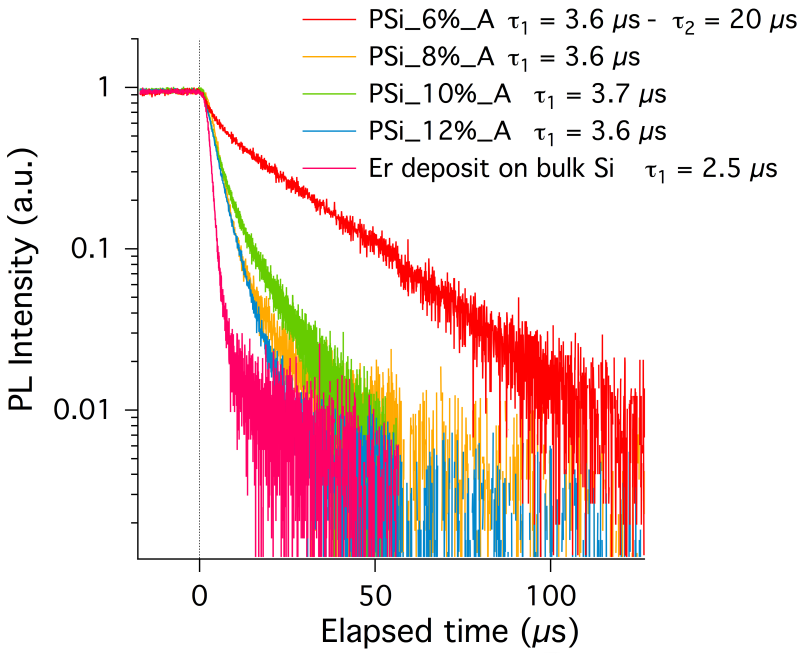

Figure 6.6: *Time-resolved PL results from annealed samples with different Er content and the relative decay times obtained by fitting the curves with exponential functions. The purple line with the shorter decay time is referred to a bulk Si wafer with a thick Er-rich layer deposited on top using the same solution and doping current used for the doping of the porous samples.*

represents the behaviour of a relatively thick Er layer deposited on a bulk Si sample using the same electrochemical deposition process but for a longer duration (2000 s). This different sample has a faster decay time of $\tau = 2.5\,\mu$s, while the time resolution of the set-up, measured as the apparent duration of a sub-picosecond laser pulse, was around 1 ns.

In order to understand if the emitted light came predominantly from few hotspots or homogeneously from all the sample surface, micro-PL measurements have been evaluated. In figure 6.7 (a) micro-PL measurements of an annealed PSi sample with 8% Er is shown, while in (b) is reported the corresponding bidimensional mapping: the intensity of each point on the map has been taken as the integrated intensity over the red area in the corresponding spectrum. Looking at the results, PL emission is quite homogenous in all the

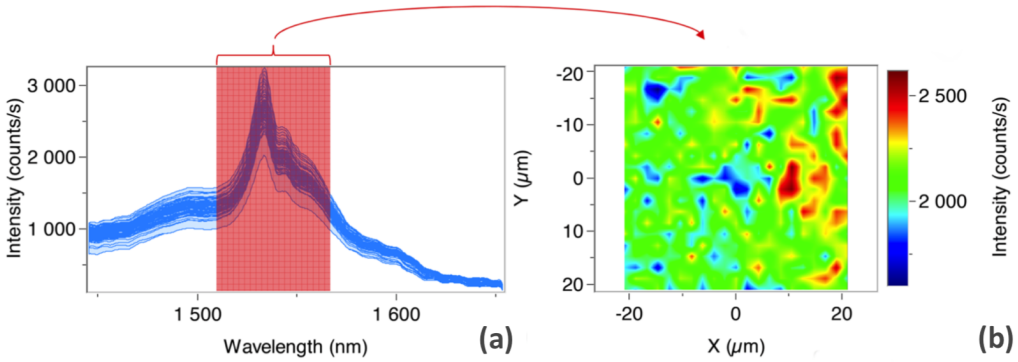

Figure 6.7: *(a) Micro-PL measurements of an annealed PSi sample with 8% Er; (b): bidimensional mapping of micro-PL results shown in (a): the intensity of each point on the map has been taken as the integrated intensity over the red area in the corresponding spectrum.*

map, with small intensity fluctuations compatible with small local Er content differences and little local surface asperities.

All the results of this work can be summarized in figure 6.8: the evolution of the electrochemical doping process is represented with the red curve, that is the voltage as a function of the Er content (using table 6.1 to convert doping time in erbium percentage); PL data are taken from figure 6.5 and are indicated as coloured rectangular bars, one for each analyzed doping level (vertical black lines). As already mentioned, the applied voltage is not constant during the Er doping, and the various transients are an indication of different doping regimes. The first double transient had been already studied [30, 83–85] and has been attributed to the formation of a surface layer of Er ethanolate gel, whose higher density facilitates the ions permanence inside the pores.

After the first double transient, the voltage remains approximately constant: the ET result on the 1.2% doped sample suggests that this is the phase where Er accumulates in the pores walls in form of small nanoclusters or thin film near the top surface. As the electrochemical doping process goes on, the Er filling starts from the pores walls and continues to their center. This was

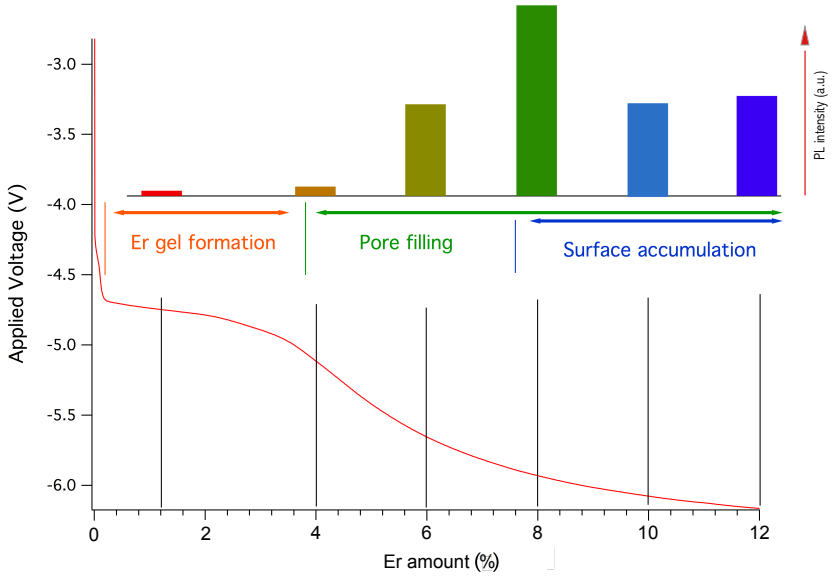

Figure 6.8: *Synoptic representation of the results about the Si pores filling with Er. The red curve represents the evolution of the applied voltage during the electrochemical doping in galvanostatic regime; the black lines across the curve indicate the Er doping levels that have been presented in the text. Immediately above them, the colored rectangles represent the PL intensity corresponding to the various doping levels. Finally, thanks to morphological characterization, it has been possible di identify the different phases of the doping process, whose labels are reported under the PL results.*

evident from ET (figure 6.3, panels (G) to (L)) of the 8% doped-sample, where the dark core of the filled pores was visible. In this phase, the increase of the voltage absolute value is due to the reduction of the pores effective diameter that progressively increases the voltage needed to move the Er ions inside them. From SEM-BSE analysis (figure 6.4) of the same sample, instead, the Er surface accumulation emerged, coherently with the results reported in reference [83], and it progressively continues as the doping level increases. Then, thee different regimes in the doping process can be identified: (A) Er gel formation, (B) pore filling and (C) a contemporaneous pore filling and superficial film accumulation. It is interesting to compare the three regimes with the corresponding PL results: when the amount of erbium is very low (1.2%) a weak PL emission is measured; when the Er content increases, so happens to PL emission. The maximum intensity is measured for the sample with 8% Er-level, which corresponds to the beginning of the superficial film deposition. This could be explained by the fact that the Er-rich material inside the pores is more efficient than the surface coverage in PL emission, which tends to decrease when the surface accumulation covers the entire sample. Another important information on these types of samples can be obtained by the measurements of the decay times of the PL emission (figure 6.6). The sample with 6% Er-doping showed two different decay times, one faster and one slower, and it had no surface Er layer since it is below the surface accumulation threshold. All the samples with a higher Er level, which also have a surface accumulation on top, exhibited one only short decay time. These observations can help to attribute a double origin to the PL emission: the thermal annealing produces an erbium silicate inside the pores near the walls, while erbium oxide is produced elsewhere. The first one is characterized by a slower decay time, while the second exhibits a faster emission and this hypothesis is supported by the two literature works [186, 187]. From this analysis, it is possible to hypothesize that the light emission from samples with Er-rich film coverage is mainly due to Er oxide, while the emission without the superficial layer mainly comes from Er silicate that is inside the PSi matrix.

6.3 Er-doping of large-pores samples

Since a more regular structure and a larger diameter have a great influence in solution mobility inside the pores, the modification of the porous matrix can bring a further improvement in the electrochemical impregnation with erbium. For this reason, we used the ENL protocol to fabricate PSi samples with larger pores, and we made some preliminary studies on the effect of the new porous matrix on the impregnation process with the erbium solution.

The technical parameters for PSi samples preparation using the ENL protocol are reported in section 4.1.1, while the electrochemical doping with Er has been performed in the same way as standard samples, according to the procedure explained in 4.2.2. Figure 6.9 shows the comparison between the applied voltage evolution measured during the electrochemical doping with Er of a PSi sample fabricated using ENL (a) with the analogous evolution obtained in case of a standard PSi doping (b). The two graphs refer to the same doping time, that is 300 s, and the evolution of the applied voltage is similar in both cases. In particular, the transients that indicate the various phases of the electrochemical doping are visible also for ENL samples. SEM characterizations using backscattered electrons (SEM-BSE) show that the Er penetration within the pores is significantly improved in case of ENL samples, since the images show a full filling in the whole pores length. Since the new pores are larger and less dendritic as compared with standard samples, this result can be explained with the improved mobility of the solution within the larger pores. Of course, this difference also reflects onto the specific transient shape. If, on one side, the presence of the different transient in both thin- and large-pore samples demonstrates that the process is the same in both cases, on the other side the details of the transients depend on the specific pores characteristics. For instance, larger pores do not imply higher porosity, that is larger volumes within the pores, but a better penetration of the pores may compensate a lower porosity: the position of the third transient, the one related to the pores filling process, will depend from the details of the fabricated pores. All these aspects require a detailed study

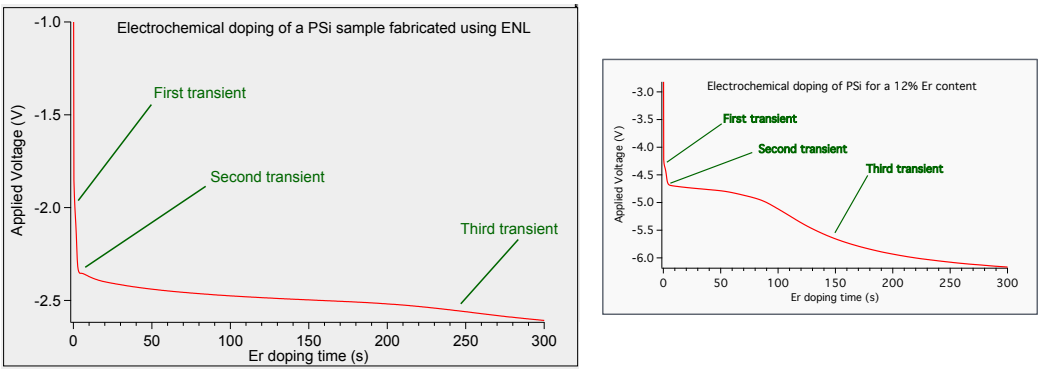

Figure 6.9: *Evolution of the applied voltage during the electrochemical doping with erbium of a PSi sample fabricated using ENL (a) and the analogous evolution obtained in case of a standard PSi doping (b). The transients that represent the various phases of the electrochemical impregnation process are visible in both cases.*

for a full understanding, but the main result of these preliminary tests is that an increase of the pores diameter by a simple factor of three lead to a significantly improved pores filling.

The SEM-BSE characterizations showing the improved filling have been done by A. Falqui and coworkers at KAUST (Saudi Arabia). Since the backscattering coefficients depend on the atomic number of the involved chemical species, in SEM-BSE of the PSi:Er samples the number of backscattered electrons is higher for the regions where the Er content is higher. As a consequence, a great contrast should be visible between Er and Si signals.

The analysis results of an ENL PSi sample doped for 200 s are shown in figure 6.10: a) is the cross section SEM-BSE image, while b) is the trend of O, Er and Si signals measured as a function of the distance from the top surface of the same sample of a). It is worth to note that the brighter areas of image 6.10 a) are the areas with higher Er content: looking at these bright areas, it is easy to note that the Er-rich material completely fills the pores shape. Since these are preliminary studies, there are still open

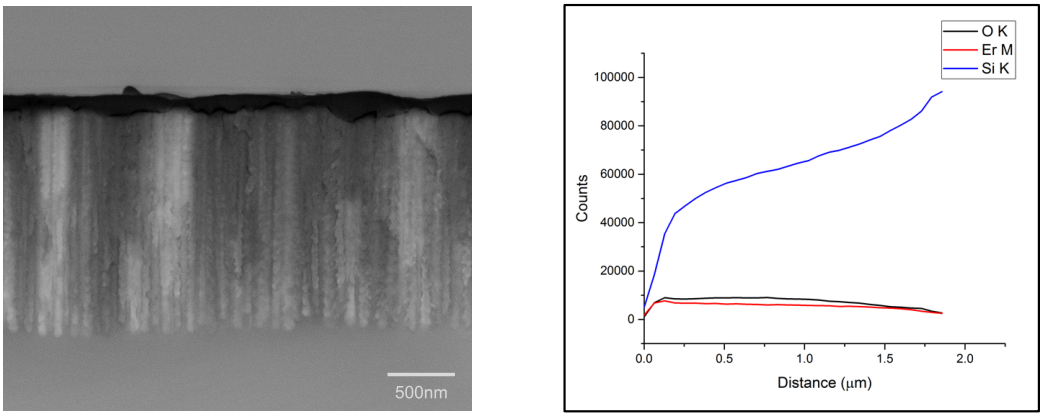

Figure 6.10: *a) SEM-BSE image of an Er-doped PSi sample. b) behaviour of O, Er and Si signals as a function of the distance from the top surface of the sample.*

questions on the apparent inhomogeneity of the filling that will require further investigations. These results indicate that filling of larger pores is, as expected, more effective for the homogeneous filling in the whole pore length, that is 1.7 nm in this case. If we compare these results with ET images of Er-doped standard PSi samples reported in section 6.2, we notice that the thin pores were filled up to a length of 800 nm, even if the thickness of the porous layer was about 1.3 µm. For standard samples, therefore, the highly dendritic structure and the small openings do not permit the solution to efficiently move within the pores and therefore to have a sufficient exchange with the external solution to keep the Er concentration constant in the whole pores length. Moreover, small Er accumulation within the thin pores will lead to significant reduction of the available pores diameter even with small deposits. Since the solution mobility depends on the square of the pores radius, the consequence is that the filling of the pores can be significantly improved by small increase in their diameter. In summary, the possibility to fill the pores depends strongly on the pore diameter and it appears that significant improvements in the pores filling can be achieved even with relatively small increases in the pore diameter. Although this strategy still needs further

studies, the full pores filling shown by the SEM-BSE images demonstrate that this approach is a very promising route towards high pores filling and therefore highly photoluminescent materials.

Chapter 7

Porous silicon impregnated with nickel

This last chapter is intended to present another application of the impregnation of PSi with a metallic material. This study has been possible thanks to the competencies that we acquired on PSi impregnation, in this case with electrochemical methods. In section 7.1, in fact, the results obtained on PSi samples electrochemically filled with nickel are proposed with the aim of obtaining a new protocol for analysis and accurate reconstruction of nanoporous materials by APT.

7.1 Nickel in porous silicon for a better atom probe tomography reconstruction

The aim of the work presented in reference [101] was to propose a new protocol for analysis and accurate reconstruction of nanoporous materials by APT. A study on this topic was then possible thanks to the collaboration with I. Mouton and coworkers from CEA-LETI and Université Grenoble Alpes; in fact, our expertise in pores filling, especially through electrochemical processes, has been put together with their expertise in reconstruction techniques to find a way to perform reliable APT reconstruction on porous materials. APT is a material analysis technique that allows the 3D reconstruction of a

specimen at the atomic scale, with around 0.1-0.3 nm in depth and 0.3-0.5 nm lateral resolutions. It is based on the field evaporation of atoms from the tip of a needle-shaped portion of a sample, and the current reconstruction algorithm is based on a geometric model that works as a point projection of ion position on a hemispherical surface [191]. What is critical in this process is the accurate evaluation of the reconstruction parameters, in order to obtain a reliable spatial reconstruction of the real specimen. This process is quite easy in case of metallic materials, since the calibration is based on lattice planes or desorption patterns [192], while it is complicated for semiconductors and multiphase materials, where the projection laws affect the reconstruction parameters, and the evaporation fields could be different from one phase to another [193, 194]. As a matter of fact, APT analysis and reconstruction with porous materials is quite a challenge: until now, the only way to make APT analysis possible is the filling of pores with 50 nm diameter with electron beam induced deposition [195, 196]. To solve these problems, several research groups have proposed to improve algorithm [197] or constrain reconstruction [198–200] using other characterization techniques to integrate complementary information. The most used technique is ET [201–203] because it allows discerning 3D nanoscale structure from a series of 2D projection images acquired at different tilt angles with a transmission electron microscope (TEM) [204].
In this study, ET has been used together with APT on the same needle, taken from a nickel-impregnated PSi sample, in order to implement a new model for APT reconstruction. The reason why the two analysis techniques have been used together is that they allow a direct comparison between the reconstructed volume of the same sample, so that one can immediately know how good the reconstruction is by checking the correspondence of the two results. The analysis criterion is based on the proportion of well-positioned atoms for one APT reconstruction when compared to the ET reference volume. This correlation algorithm has been applied to mesoporous Si samples for their singular form of dendritic pores.

The samples were 1 µm thick with pores of 10 nm diameter, and they have

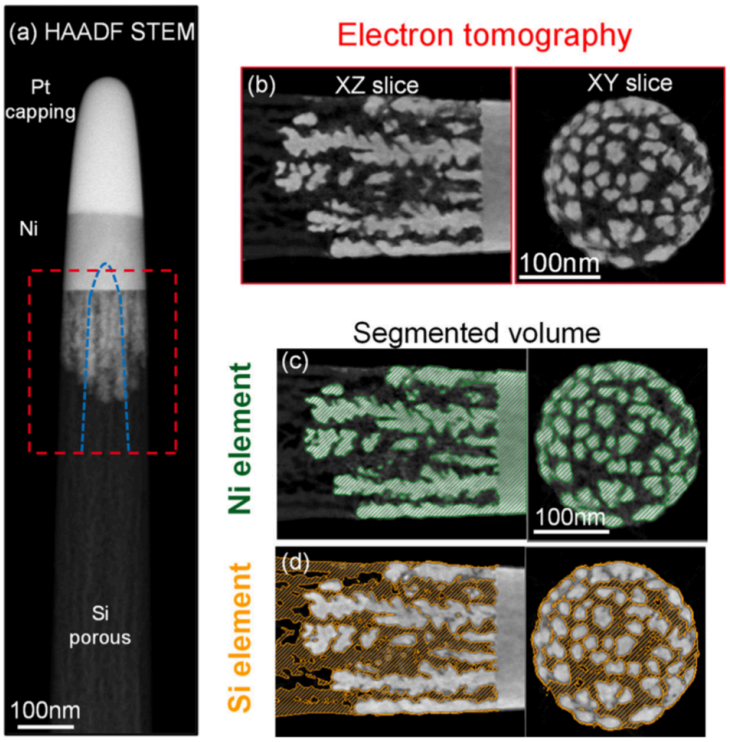

Figure 7.1: *(a) HAADF STEM image of the whole tip with corresponding ET and APT analyzed volume respectively in red and blue. Slices in XZ and XY direction from (b) the ET reconstruction with segmented volume for (c) nickel and (d) silicon element.*

been electrochemically filled with nickel since it has a similar evaporation field than silicon. The fabrication and impregnation of the samples have been performed at PoroSiLab in Cagliari (the details are reported in 4.1.1 and **??**, respectively), while all the analysis and their interpretation have been carried out by our collaborators in Grenoble. First of all, a check of the electrochemical filling and an observation of the microstructural features (pores size, morphology) has been done by using a FIB/SEM [205]. Then, to reduce electron beam damage and to have a large field of view, the analysis has been done on a needle of 200 nm diameter extracted from the porous sample. ET has been carried out on a FEI Titan Themis at 200 kV in High Annular Dark Field (HAADF) scanning electron transmission microscopy (STEM) using a 2050 Fishione holder with a tilt acquisition from $-90°$ to $90°$ with steps of $1°$. All the images have been denoised, aligned and reconstructed according to the procedures described by Printemps et al. in [104]. In figure 7.1 (a) a HAADF STEM image of the needle extracted from the sample is shown. Different layers are visible starting from the top: a platinum capping deposited for sample preparation, a nickel layer, nickel-filled silicon pores and empty silicon pores. Figure 7.1 (b), instead, shows a yz-slice and an xy-slice of the ET reconstruction, and the reconstructed volume is then segmented using global thresholding of the whole volume: in (c) nickel is evidenced in green, while silicon (d) in evidence in yellow. From ET reconstruction it is clear that pores are not damaged and are completely filled on 80 to 230 nm from the top surface, and this makes possible APT experiments. To do the APT analysis, the same needle has been afterwards reduced to achieve a sharp curvature (around 50 nm), using a Cameca-Flextap in UV-laser pulsing mode ($\lambda = 343$ nm). During the sample evaporation for reducing the needle dimensions it has emerged the good adhesion and quality of the pores filling with nickel, since no irregular variation of the detection flux (or applied voltage) has been observed. For APT data reconstruction, a cone angle reconstruction algorithm [206] has been used, while 3D visualization is carried out with Avizo software.

In figure 7.2 the APT reconstruction has been shown: the top nickel layer is represented in green and the filled silicon porous layer is represented both in

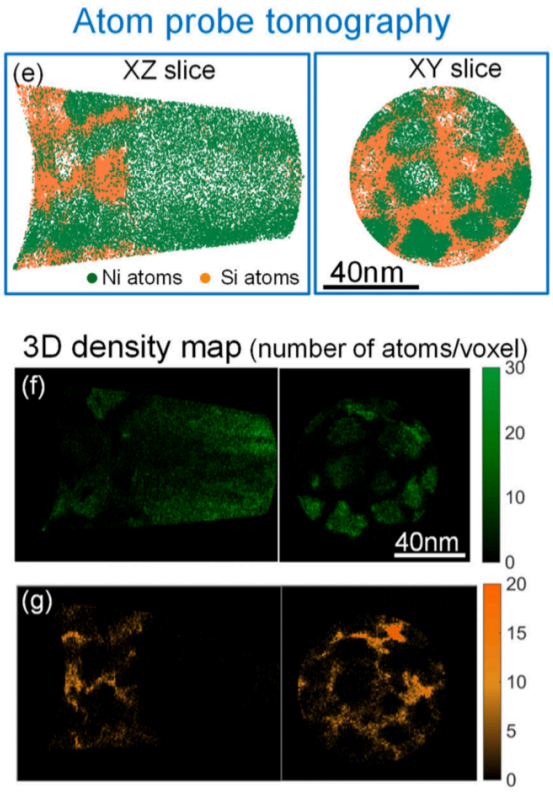

Figure 7.2: *APT reconstruction (e) of the nickel-filled porous sample with density map (in number of atoms) for (f) nickel and (g) silicon.*

orange (the Si part) and green (the Ni part). Since the sample broke, only a 50 nm thick portion of the nickel-filled porous layer has been observed with APT. In ET reconstruction, images were composed of intensity voxels, while 3D scatter plot has been collected for APT reconstruction, where each dot represents one reconstructed atom with a coordinates triad (x, y, z) and a different colour that means a different chemical nature. In order to make possible the comparison of the two datasets, APT reconstruction is converted into a density map for each element, using the same voxel size as the ET reconstruction.

The number of atoms of the different elements is counted in all voxels allowing to generate a 3D density map (in number of atoms per voxel) for each element: figure 7.2 (f) and (g) are the 3D maps for nickel and silicon, respectively.

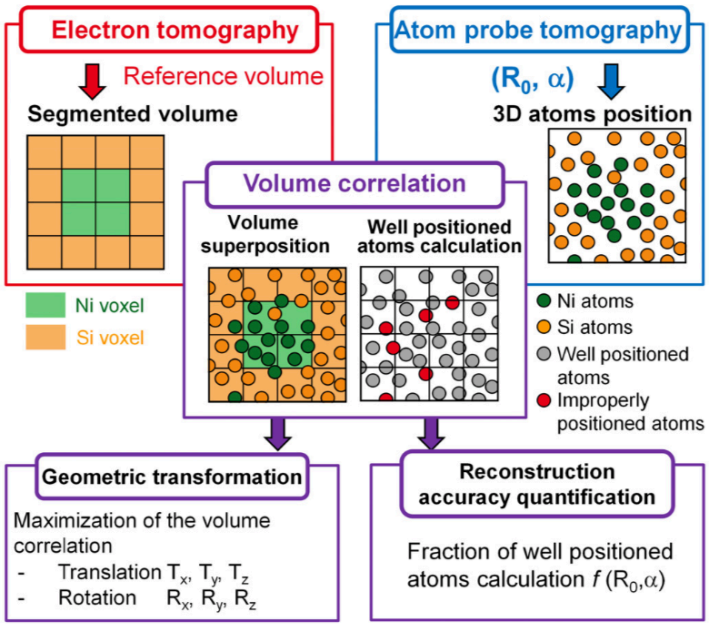

Figure 7.3: *Correlation procedure between ET and APT.*

This work aimed to find the best APT reconstruction parameters to fit the ET 3D information (interface position, object size and morphology), and a scheme of the correlation procedure between ET and APT is shown in figure 7.3. ET has been used to obtain a reference volume to force APT reconstruction parameters, indicated with $R_{0,\alpha}$. For each reconstruction parameter, a geometric transformation (rigid-body translations and/or rotations) must be applied to APT reconstruction in order to maximise the matching between APT and ET reconstructions. The optimization of the geometric transformation requires also a matching quantification between ET and APT volumes; for this reason, the criterion of the proportion of well positioned atoms in APT reconstruction as compared to the ET segmented volume has been adopted. If an atom is consistent with the corresponding segmented voxel of ET, then a reconstructed atom is considered well positioned. Extending this argumentation for each atom, it is possible to determine a fraction of well-positioned atoms for a set of reconstruction parameters $R_{0,\alpha}$. All the details about the optimization of the reconstruction algorithm can be found

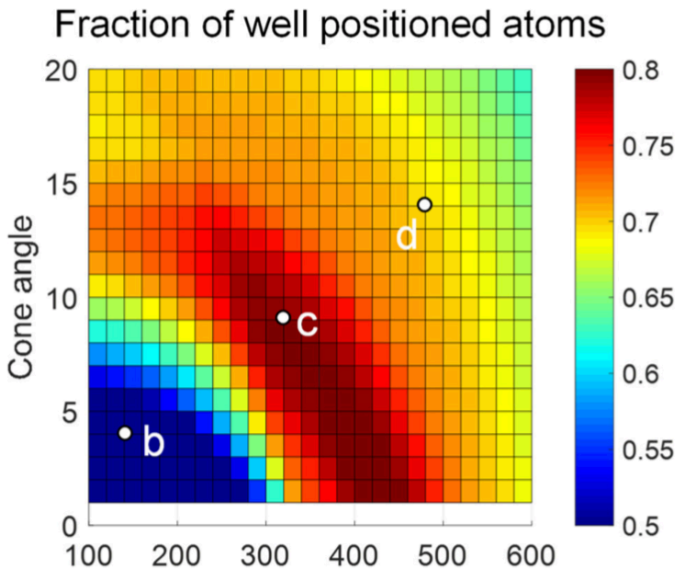

Figure 7.4: *Dependence of the APT reconstruction parameters $R_{0,\alpha}$ on the fraction of well positioned atoms.*

in reference [101], but it is worthy to underline is that the use of a well-filled PSi sample with mesopores of around 10 nm turned out to be successful for the aim of the research. In fact, the fraction of well positioned atoms has been calculated for a range of APT reconstruction parameters (cone angle algorithm); in figure 7.4 the results on fraction of well positioned atoms as a function of initial radius (R_0 from 100 Å to 600 Å) and cone angle (α from 1° to 20°) are presented.

To conclude, this correlation methods turned out to work well with porous and nanostructured materials because the 3D features of the sample have well distinctive shapes and the two elements Si and Ni have a quite different atomic number so that they can be clearly observed with the electron microscopes thanks to their chemical contrast.

Conclusion

The aim of this thesis was to study the impregnation of PSi matrices with different materials and different techniques so that a better understanding of the process could optimize the final properties of the composite systems.
The first part of the work was devoted to the study of PSi samples chemically filled with melanin. The interest on this junction was born for its photovoltaic properties, but the complexity of the materials involved required a more accurate comprehension of the two building materials themselves. In this sense, the photocurrent produced by the samples has been used in this dissertation more as a mean to investigate materials and junction's properties and stability. In chapter 5 the optimization of the samples impregnation in order to improve the organic-inorganic junction stability has been presented. The first parameters that have been investigated were expected to favour stronger chemical bonds between eumelanin and silicon. They were the modification of the composition of the monomer solution and the functionalization of the inner surface of the pores through a light electrochemical oxidation, but the results reported in section 5.1 showed that these had not a key role in the optimization of the samples properties. Enlarging the pores diameter of our samples of more than 50% (from 10-15 nm to 50-60 nm), it led to an increase of the junction lifetime from one to several weeks. To fabricate samples with 40-60 nm diameter pores that were also homogeneous in the size distribution and pores repartition, we developed a new electrochemical method for the lithography of the Si surface. The introduction of the ENL as a novel method to produce PSi matrices allowed us to understand that pores dimension turned out to be a fundamental parameter that highly affects the impregnation of a porous matrix.

In parallel with the chemical impregnation of PSi with melanin, we studied the electrochemical impregnation of PSi with metals. In chapter 6, the object of the study was the impregnation of PSi samples with erbium, whose main characteristic is light emission in the region of transparency for telecommunication transmission. The main issue of this composite system has always been erbium clustering, which limits PL emission, and it usually appears in the condition of "pore doping" with around 1-2% of Er. A careful study of the electrochemical impregnation process and a multidisciplinar analysis of samples filled with increasing amounts of Er led to propose a new strategy to overcome this problem. Different doping levels have been studied in order to compare the "pore doping" regime with a progressive filling of the pores with Er-rich material, and the morphological analysis permitted to characterize the various steps of the doping process. Electron tomography images of the samples showed a gradual evolution from erbium clusters, randomly distributed on pores walls, to a continuous erbium accumulation, as the doping level increased. Finally, a surface layer for high doping levels was also visible. Then, three important steps in the impregnation process have been identified: the Er gel formation, the pore filling and the surface accumulation of the Er-rich material. The understanding of the electrochemical filling permitted to understand which fabrication condition could optimize the PL emission from this type of samples. Luminescence analysis revealed that the more Er is put inside the pores, the higher is the light intensity; the maximum intensity has been measured in correspondence to the beginning of the surface accumulation on top of the samples. We also demonstrated that, as in case of chemical impregnation with melanin, also electrochemical impregnation with erbium is strongly affected by the morphology of the porous matrix. Er-filled ENL PSi samples have been studied through SEM-BSE and the results permitted to note that some of the pores are completely filled in all their length. This is a partial improvement in the pore filling process with respect to the past, since the previous morphological analysis on standard samples showed that the bottom of the pores remained always empty. We suppose that the more regular structure and the larger diameters of the pores made using ENL protocol permit an easier penetration of the Er solution,

differently from what happens in case of thin standard pores.
Chapter 7, instead, reports the results on the impregnation of PSi with nickel. The two elements Si and Ni have a similar evaporation field, and this was mandatory because the samples have been used to develop a new protocol for analysis and reconstruction of nanoporous material by atom probe tomography. The aim of this chapter was, in fact, to show another application of the impregnation of PSi with a metallic material, and it has been possible thanks to our ability in electrochemical impregnation of PSi matrices. The choice of the right impregnation technique and the optimization of the electrochemical parameters permitted to get the desired result: the use of electron tomography and of atom probe tomography on the same needle allowed to put together information on the sample volume from both the techniques and to perform an affordable 3D reconstruction of the analyzed sample. Thanks to this improvement in APT reconstruction it will be possible to gain reliable and accurate information of both structural and chemical properties of complex sample as porous materials or other multiphase materials.
In this dissertation we have demonstrated that the impregnation of a PSi matrix is affected by a huge number of parameters. Chemical and electrochemical impregnations are quite different processes, but in both cases the final sample properties depend on the optimization of the same details. Many variables must be taken into account when performing impregnation of such complex porous structures, since the possibility to control or not them can have delicate consequences on the final samples properties. Among all, the shape and the dimension of the pores turned out to have a significant role in the studies proposed in this dissertation. Changing the pores diameter from 10-15 nm to 50-60 nm modifies the fluidity of the solution and its capability to penetrate inside the pores; as a result, both the samples chemically and electrochemically filled showed an improvement in their properties and/or in their structural characteristics. Moreover, the relevance of the polymerization process itself and of the interface thickness has been put into evidence, underlying the unavoidable need of combined approaches for the understanding of complex nanostructured materials. Despite the great improvements that we obtain in controlling and understanding both the chemical and electro-

chemical impregnation methods, still more work has to be done in both cases with the aim to enhance the samples properties. A deep understanding of the impregnation process permits to be conscious of the many parameters that can affect the final results and their control is a compulsory aspect for the optimization of the samples in order to exploit them for technological applications.

Bibliography

[1] E. Washburn, "The dynamics of capillary flow," *Physical review*, vol. 17, no. 3, p. 273, 1921.

[2] B. Zhmud, F. Tiberg, and K. Hallstensson, "Dynamics of capillary rise," *Journal of colloid and interface science*, vol. 228, no. 2, pp. 263–269, 2000.

[3] D. Hillel and J. Hatfield, *Encyclopedia of soils in the environment*, vol. 3. Elsevier Amsterdam, 2005.

[4] A. Bsiesy, Y. Nicolau, A. Ermolieff, F. Muller, and F. Gaspard, "Electroluminescence from n+-type porous silicon contacted with layer-by-layer deposited polyaniline," *Thin Solid Films*, vol. 255, no. 1-2, pp. 43–48, 1995.

[5] R. Herino, M. Gros-Jean, L. Montes, and D. Lincot, "Electrochemical and chemical deposition of ii-vi semiconductors in porous silicon," *MRS Online Proceedings Library Archive*, vol. 452, 1996.

[6] H. Lopez, X. Chen, S. Jenekhe, and P. Fauchet, "Tunability of the photoluminescence in porous silicon due to different polymer dielectric environments," *Journal of luminescence*, vol. 80, no. 1-4, pp. 115–118, 1998.

[7] P. Kleimann, J. Linnros, C. Fröjdh, and C. Petersson, "An x-ray imaging pixel detector based on scintillator filled pores in a silicon matrix,"

Nuclear Instruments and Methods in Physics Research Section A: Accelerators, Spectrometers, Detectors and Associated Equipment, vol. 460, no. 1, pp. 15–19, 2001.

[8] F. Zacharatos and A. Nassiopoulou, "Copper-filled macroporous si and cavity underneath for microchannel heat sink technology," *Physica status solid (a)*, vol. 205, no. 11, pp. 2513–2517, 2008.

[9] P. Granitzer, K. Rumpf, P. Pölt, S. Šimič, and H. Krenn, "Three-dimensional quasi-regular arrays of ni nanostructures grown within the pores of a porous silicon layer–magnetic characteristics," *Physica status solid (c)*, vol. 5, no. 12, pp. 3580–3583, 2008.

[10] P. Granitzer, K. Rumpf, P. Pölt, A. Reichmann, and H. Krenn, "Self-assembled mesoporous silicon in the crossover between irregular and regular arrangement applicable for ni filling," *Physica E: Low-dimensional Systems and Nanostructures*, vol. 38, no. 1-2, pp. 205–210, 2007.

[11] K. Rumpf, P. Granitzer, P. Pölt, A. Reichmann, and H. Krenn, "Structural and magnetic characterization of ni-filled porous silicon," *Thin Solid Films*, vol. 515, no. 2, pp. 716–720, 2006.

[12] S. Prischepa, A. Dolgiy, H. Bandarenka, V. Bondarenko, K. Yanushkevich, V. Bayev, A. Maximenko, Y. A. Fedotova, A. Zarzycki, and Y. Zabila, "Synthesis and properties of ni nanowires in porous silicon templates," *Nanowires: Synthesis, Electrical Properties and Uses in Biological Systems (ed. Luke J. Wilson), Nova Science Publ. Inc*, pp. 89–128, 2014.

[13] K. Rumpf, P. Granitzer, N. Koshida, P. Poelt, and H. Michor, "Morphology controlled magnetic interactions of porous silicon embedded nanostructures," *ECS Transactions*, vol. 64, no. 47, pp. 9–14, 2015.

[14] P. Granitzer, K. Rumpf, P. Poelt, and M. Reissner, "Magnetic characteristics of ni-filled luminescent porous silicon," *Frontiers in chemistry*, vol. 7, 2019.

[15] N. Errien, P. Joubert, A. Chaillou, C. Mahric, C. Godon, G. Louarn, and G. Froyer, "Electrochemical growth of poly (3-dodecylthiophene) into porous silicon: a nanocomposite with tubes or wires?," *Materials Science and Engineering: B*, vol. 100, no. 3, pp. 259–262, 2003.

[16] T. Nguyen, P. Le Rendu, M. Lakehal, M. De Kok, D. Vanderzande, A. Bulou, J. Bardeau, and P. Joubert, "Filling porous silicon pores with poly (p phenylene vinylene)," *Physica status solidi (a)*, vol. 197, no. 1, pp. 232–235, 2003.

[17] N. Tokranova, I. Levitsky, B. Xu, J. Castracane, and W. Euler, "Hybrid solar cells based on organic material embedded into porous silicon," in *Organic Photonic Materials and Devices VII*, vol. 5724, pp. 183–190, International Society for Optics and Photonics, 2005.

[18] Y. Piryatinski, L. Dolgov, O. Yaroshchuk, and S. Lazarouk, "Fluorescence of porous silicon filled with liquid crystal 5cb," *Molecular Crystals and Liquid Crystals*, vol. 467, no. 1, pp. 195–202, 2007.

[19] L. Marsal, P. Formentín, R. Palacios, T. Trifonov, J. Ferré-Borrull, A. Rodriguez, J. Pallarés, and R. Alcubilla, "Polymer microfibers obtained using porous silicon templates," *Physica status solid (a)*, vol. 205, no. 10, pp. 2437–2440, 2008.

[20] F. Harraz, S. El-Sheikh, T. Sakka, and Y. Ogata, "Cylindrical pore arrays in silicon with intermediate nano-sizes: a template for nanofabrication and multilayer applications," *Electrochimica Acta*, vol. 53, no. 22, pp. 6444–6451, 2008.

[21] Y. Li, F. Cunin, M. Sailor, J. Link, and T. Gao, "Nanostructured casting of organic and bio-polymers in porous silicon templates," May 11 2010. US Patent 7,713,778.

[22] M. Chourou, K. Fukami, T. Sakka, and Y. Ogata, "Gold electrodeposition into porous silicon: Comparison between meso-and macroporous silicon," *Physica status solid (c)*, vol. 8, no. 6, pp. 1783–1786, 2011.

[23] L. Jin, E. Kondoh, T. Oya, and B. Gelloz, "Supercritical fluid deposition of copper into mesoporous silicon," *Thin Solid Films*, vol. 545, pp. 357–360, 2013.

[24] A. Kashyout, H. Soliman, M. Nabil, and A. Bishara, "Impact of congo red dye in nano-porous silicon as ph-sensor," *Sensors and Actuators B: Chemical*, vol. 216, pp. 279–285, 2015.

[25] L. Montes, F. Muller, and R. Hérino, "Localized photo-assisted electrodeposition of zinc selenide into p-type porous silicon," *Journal of Porous Materials*, vol. 7, no. 1-3, pp. 77–80, 2000.

[26] H. Elhouichet, A. Moadhen, M. Oueslati, S. Romdhane, J. Roger, and H. Bouchriha, "Structural, optical and electrical properties of porous silicon impregnated with SnO_2: Sb," *Physica status solid (c)*, vol. 2, no. 9, pp. 3349–3353, 2005.

[27] R. Hérino, "Nanocomposite materials from porous silicon," *Materials Science and Engineering: B*, vol. 69, pp. 70–76, 2000.

[28] L. Vellutini, N. Errien, G. Froyer, N. Lacoudre, S. Boileau, F. Tran-Van, and C. Chevrot, "Polymerization of supramolecular diacetylenic monomer embedded in porous silicon matrix," *Chemistry of materials*, vol. 19, no. 3, pp. 497–502, 2007.

[29] F. Ronkel, J. Schultze, and R. Arens-Fischer, "Electrical contact to porous silicon by electrodeposition of iron," *Thin Solid Films*, vol. 276, no. 1-2, pp. 40–43, 1996.

[30] G. Mula, E. Pinna, A. Falqui, R. Ruffilli, S. Palmas, and M. Mascia, "Electrochemical doping of mesoporous silicon with er: the effect of the current intensity," *Applied Surface Science*, vol. 311, pp. 252–257, 2014.

[31] P. Granitzer, K. Rumpf, P. Pölt, S. Šimić, and H. Krenn, "Formation of self-assembled metal/silicon nanocomposites," *Physica status solid (a)*, vol. 205, no. 6, pp. 1443–1446, 2008.

[32] A. Uhlir Jr, "Electrolytic shaping of germanium and silicon," *Bell System Technical Journal*, vol. 35, no. 2, pp. 333–347, 1956.

[33] A. Cullis, L. T. Canham, and P. Calcott, "The structural and luminescence properties of porous silicon," *Journal of applied physics*, vol. 82, no. 3, pp. 909–965, 1997.

[34] A. Bsiesy, J. Vial, F. Gaspard, R. Herino, M. Ligeon, F. Muller, R. Romestain, A. Wasiela, A. Halimaoui, and G. Bomchil, "Photoluminescence of high porosity and of electrochemically oxidized porous silicon layers," *Surface Science*, vol. 254, no. 1-3, pp. 195–200, 1991.

[35] A. Cullis and L. Canham, "Visible light emission due to quantum size effects in highly porous crystalline silicon," *Nature*, vol. 353, no. 6342, p. 335, 1991.

[36] E. Abramova, A. Khort, A. Yakovenko, M. Tsygankova, Y. V. Syrov, T. Sorokin, and V. Shvets, "Origin of porous silicon photoluminescence peaks in the wavelength range 460-700 nm," in *Doklady Chemistry*, vol. 481, pp. 166–169, Springer, 2018.

[37] F. Karbassian, "Porous silicon," in *Porosity-Process, Technologies and Applications*, IntechOpen, 2018.

[38] M. Sailor, *Porous silicon in practice: preparation, characterization and applications*. John Wiley & Sons, 2012.

[39] Z. Huang, N. Geyer, P. Werner, J. De Boor, and U. Gösele, "Metal-assisted chemical etching of silicon: a review: in memory of prof. ulrich gösele," *Advanced materials*, vol. 23, no. 2, pp. 285–308, 2011.

[40] L. Li, X. Zhao, and C. Wong, "Charge transport in uniform metal-assisted chemical etching for 3d high-aspect-ratio micro-and nanofabrication on silicon," *ECS Journal of Solid State Science and Technology*, vol. 4, no. 9, pp. P337–P346, 2015.

[41] C. Lai, H. Cheng, W. Choi, and C. Thompson, "Mechanics of catalyst motion during metal assisted chemical etching of silicon," *The Journal of Physical Chemistry C*, vol. 117, no. 40, pp. 20802–20809, 2013.

[42] N. Geyer, B. Fuhrmann, Z. Huang, J. de Boor, H. Leipner, and P. Werner, "Model for the mass transport during metal-assisted chemical etching with contiguous metal films as catalysts," *The journal of physical chemistry C*, vol. 116, no. 24, pp. 13446–13451, 2012.

[43] D. Wang, R. Ji, S. Du, A. Albrecht, and P. Schaaf, "Ordered arrays of nanoporous silicon nanopillars and silicon nanopillars with nanoporous shells," *Nanoscale research letters*, vol. 8, no. 1, p. 42, 2013.

[44] R. Lai, T. Hymel, V. Narasimhan, and Y. Cui, "Schottky barrier catalysis mechanism in metal-assisted chemical etching of silicon," *ACS applied materials & interfaces*, vol. 8, no. 14, pp. 8875–8879, 2016.

[45] J. Borovansky and P. Riley, *Melanins and melanosomes: biosynthesis, structure, physiological and pathological functions*. John Wiley & Sons, 2011.

[46] R. Nicolaus, M. Piattelli, and E. Fattorusso, "The structure of melanins and melanogenesis—iv: on some natural melanins," *Tetrahedron*, vol. 20, no. 5, pp. 1163–1172, 1964.

[47] G. Prota, "The chemistry of melanins and melanogenesis," in *Fortschritte der Chemie organischer Naturstoffe/Progress in the Chemistry of Organic Natural Products*, pp. 93–148, Springer, 1995.

[48] Y. Liu, L. Hong, K. Wakamatsu, S. Ito, B. Adhyaru, C. Cheng, C. Bowers, and J. Simon, "Comparison of structural and chemical properties of black and red human hair melanosomes," *Photochemistry and Photobiology*, vol. 81, no. 1, pp. 135–144, 2005.

[49] P. Meredith, B. J. Powell, J. Riesz, S. Nighswander-Rempel, M. Pederson, and E. Moore, "Towards structure-property-function relationships for eumelanin," *Soft Matter*, vol. 2, no. 1, pp. 37–44, 2006.

[50] E. Vahidzadeh, A. Kalra, and K. Shankar, "Melanin-based electronics: from proton conductors to photovoltaics and beyond," *Biosensors and Bioelectronics*, 2018.

[51] A. Pezzella, M. d'Ischia, A. Napolitano, A. Palumbo, and G. Prota, "An integrated approach to the structure of sepia melanin. evidence for a high proportion of degraded 5,6-dihydroxyindole-2-carboxylic acid units in the pigment backbone," *Tetrahedron*, vol. 53, no. 24, pp. 8281–8286, 1997.

[52] K. Wakamatsu and S. Ito, "Advanced chemical methods in melanin determination," *Pigment Cell Research*, vol. 15, no. 3, pp. 174–183, 2002.

[53] G. Zajac, J. Gallas, J. Cheng, M. Eisner, S. Moss, and A. Alvarado-Swaisgood, "The fundamental unit of synthetic melanin: a verification by tunneling microscopy of x-ray scattering results," *Biochimica et Biophysica Acta (BBA)-General Subjects*, vol. 1199, no. 3, pp. 271–278, 1994.

[54] P. Meredith and T. Sarna, "The physical and chemical properties of eumelanin," *Pigment cell research*, vol. 19, no. 6, pp. 572–594, 2006.

[55] M. Wolbarsht, A. Walsh, and G. George, "Melanin, a unique biological absorber," *Applied Optics*, vol. 20, no. 13, pp. 2184–2186, 1981.

[56] J. Riesz, J. Gilmore, and P. Meredith, "Quantitative scattering of melanin solutions," *Biophysical journal*, vol. 90, no. 11, pp. 4137–4144, 2006.

[57] M. Tran, B. Powell, and P. Meredith, "Chemical and structural disorder in eumelanins: a possible explanation for broadband absorbance," *Biophysical journal*, vol. 90, no. 3, pp. 743–752, 2006.

[58] J. Gallas, G. Zajac, T. Sarna, and P. Stotter, "Structural differences in unbleached and mildly-bleached synthetic tyrosine-derived melanins

identified by scanning probe microscopies," *Pigment cell research*, vol. 13, no. 2, pp. 99–108, 2000.

[59] J. Nofsinger, S. Forest, and J. Simon, "Explanation for the disparity among absorption and action spectra of eumelanin," *The Journal of Physical Chemistry B*, vol. 103, no. 51, pp. 11428–11432, 1999.

[60] E. Pinna, C. Melis, A. Antidormi, R. Cardia, E. Sechi, G. Cappellini, M. d'Ischia, L. Colombo, and G. Mula, "Deciphering molecular mechanisms of interface buildup and stability in porous si/eumelanin hybrids," *International journal of molecular sciences*, vol. 18, no. 7, p. 1567, 2017.

[61] A. Antidormi, G. Aprile, G. Cappellini, E. Cara, R. Cardia, L. Colombo, R. Farris, M. d'Ischia, M. Mehrabanian, C. Melis, *et al.*, "Physical and chemical control of interface stability in porous si-eumelanin hybrids," *The Journal of Physical Chemistry C*, vol. 122, no. 49, pp. 28405–28415, 2018.

[62] C. Preinfalk and G. Morteani, "The industrial applications of rare earth elements," in *Lanthanides, tantalum and niobium*, pp. 359–370, Springer, 1989.

[63] S. Kapil, "Nuclear reactor core having nuclear fuel and composite burnable absorber arranged for power peaking and moderator temperature coefficient control," Sept. 15 1992. US Patent 5,147,598.

[64] S. Rodica, "Coherent radiation generation and amplification in erbium doped systems," *Advances in Optical Amplifiers*, p. 255, 2011.

[65] C. Lin, W. Tseng, and M. Feng, "Formation and characteristics of silicon nanocrystals in plasma-enhanced chemical-vapor-deposited silicon-rich oxide," *Journal of Applied Physics*, vol. 87, no. 6, pp. 2808–2815, 2000.

[66] J. Tong, H. Hsiao, and H. Hwang, "Adjustable emissions from silicon-rich oxide films prepared by plasma-enhanced chemical-vapor deposition," *Applied physics letters*, vol. 74, no. 16, pp. 2316–2318, 1999.

[67] A. Morales-Sánchez, J. Barreto, C. Domínguez-Horna, M. Aceves-Mijares, and J. Luna-López, "Optical characterization of silicon rich oxide films," *Sensors and Actuators A: Physical*, vol. 142, no. 1, pp. 12–18, 2008.

[68] M. E. Castagna, S. Coffa, M. Monaco, A. Muscara, L. Caristia, S. Lorenti, and A. Messina, "High efficiency light emitting devices in silicon," *Materials Science and Engineering: B*, vol. 105, no. 1-3, pp. 83–90, 2003.

[69] K. Kim, M. Suh, T. S. Kim, C. Youn, E. Suh, Y. Shin, K. Lee, H. Lee, M. An, H. Lee, *et al.*, "Room-temperature visible photoluminescence from silicon-rich oxide layers deposited by an electron cyclotron resonance plasma source," *Applied physics letters*, vol. 69, no. 25, pp. 3908–3910, 1996.

[70] M. Fujii, M. Yoshida, S. Hayashi, and K. Yamamoto, "Photoluminescence from SiO_2 films containing si nanocrystals and er: effects of nanocrystalline size on the photoluminescence efficiency of Er^{3+}," *Journal of Applied Physics*, vol. 84, no. 8, pp. 4525–4531, 1998.

[71] G. Franzò, D. Pacifici, V. Vinciguerra, F. Priolo, and F. Iacona, "Er^{3+} ions-si nanocrystals interactions and their effects on the luminescence properties," *Applied Physics Letters*, vol. 76, no. 16, pp. 2167–2169, 2000.

[72] P. Kik and A. Polman, "Exciton-erbium interactions in si nanocrystal-doped SiO_2," *Journal of Applied Physics*, vol. 88, no. 4, pp. 1992–1998, 2000.

[73] A. Kenyon, C. Chryssou, and C. Pitt, "Indirect excitation of 1.5 μm emission from Er^{3+} in silicon-rich silica," *Applied Physics Letters*, vol. 76, no. 6, pp. 688–690, 2000.

[74] G. Qin, G. Qin, and S. Wang, "Theory for photoluminescence from SiO_2 films containing si nanocrystals and er ions," *Journal of applied physics*, vol. 85, no. 9, pp. 6738–6745, 1999.

[75] G. Franzo, V. Vinciguerra, and F. Priolo, "The excitation mechanism of rare-earth ions in silicon nanocrystals," *Applied Physics A*, vol. 69, no. 1, pp. 3–12, 1999.

[76] A. Kenyon, C. Chryssou, C. Pitt, T. Shimizu-Iwayama, D. Hole, N. Sharma, and C. Humphreys, "Luminescence from erbium-doped silicon nanocrystals in silica: excitation mechanisms," *Journal of Applied Physics*, vol. 91, no. 1, pp. 367–374, 2002.

[77] T. Kimura, A. Yokoi, H. Horiguchi, R. Saito, T. Ikoma, and A. Sato, "Electrochemical er doping of porous silicon and its room-temperature luminescence at 1.54 μm," *Applied physics letters*, vol. 65, no. 8, pp. 983–985, 1994.

[78] A. Dorofeev, N. Gaponenko, V. Bondarenko, E. Bachilo, N. Kazuchits, A. Leshok, G. Troyanova, N. Vorosov, V. Borisenko, H. Gnaser, *et al.*, "Erbium luminescence in porous silicon doped from spin-on films," *Journal of applied physics*, vol. 77, no. 6, pp. 2679–2683, 1995.

[79] H. Lopez and P. Fauchet, "Room-temperature electroluminescence from erbium-doped porous silicon," *Applied Physics Letters*, vol. 75, no. 25, pp. 3989–3991, 1999.

[80] W. Henley, Y. Koshka, J. Lagowski, and J. Siejka, "Infrared photoluminescence from er doped porous si," *Journal of Applied Physics*, vol. 87, no. 11, pp. 7848–7852, 2000.

[81] A. Najar, H. Elhouichet, N. Lorrain, and M. Oueslati, "Excitation mechanisms and localization sites of erbium-doped porous silicon," *Applied surface science*, vol. 252, no. 16, pp. 5808–5813, 2006.

[82] N. Prtljaga, D. Navarro-Urrios, A. Tengattini, A. Anopchenko, J. Ramírez, J. Rebled, S. Estradé, J. Colonna, J. Fedeli, B. Garrido, *et al.*, "Limit to the erbium ions emission in silicon-rich oxide films by erbium ion clustering," *Optical Materials Express*, vol. 2, no. 9, pp. 1278–1285, 2012.

[83] G. Mula, S. Setzu, G. Manunza, R. Ruffilli, and A. Falqui, "Optical, electrochemical, and structural properties of er-doped porous silicon," *The Journal of Physical Chemistry C*, vol. 116, no. 20, pp. 11256–11260, 2012.

[84] G. Mula, S. Setzu, G. Manunza, R. Ruffilli, and A. Falqui, "Characterization of er in porous si," *Nanoscale research letters*, vol. 7, no. 1, p. 376, 2012.

[85] G. Mula, L. Loddo, E. Pinna, M. Tiddia, M. Mascia, S. Palmas, R. Ruffilli, and A. Falqui, "Controlling the er content of porous silicon using the doping current intensity," *Nanoscale research letters*, vol. 9, no. 1, p. 332, 2014.

[86] G. Mula, L. Loddo, E. Pinna, M. Tiddia, M. Mascia, S. Palmas, R. Ruffilli, and A. Falqui, "Characterisation of the doping of porous si with er through electrochemical impedance spectroscopy," *CHEMICAL ENGINEERING*, vol. 41, 2014.

[87] G. Mula, T. Printemps, C. Licitra, E. Sogne, F. D'Acapito, N. Gambacorti, N. Sestu, M. Saba, E. Pinna, D. Chiriu, *et al.*, "Doping porous silicon with erbium: pores filling as a method to limit the er-clustering effects and increasing its light emission," *Scientific reports*, vol. 7, no. 1, p. 5957, 2017.

[88] G. Mallory and J. Hajdu, *Electroless plating: fundamentals and applications*. William Andrew, 1990.

[89] M. Gavrila, J. Millet, H. Mazille, D. Marchandise, and J. Cuntz, "Corrosion behaviour of zinc-nickel coatings, electrodeposited on steel," *Surface and Coatings Technology*, vol. 123, no. 2-3, pp. 164–172, 2000.

[90] C. Faust, "Electrolyte for the polishing of metal surfaces and method of use," Nov. 23 1943. US Patent 2,334,699.

[91] W. Keim, "Nickel: an element with wide application in industrial homogeneous catalysis," *Angewandte Chemie International Edition in English*, vol. 29, no. 3, pp. 235–244, 1990.

[92] C. Tsang, Z. Xu, and Y. Li, "Metal-based photonic coatings from electrochemical deposition," *Journal of The Electrochemical Society*, vol. 156, no. 11, pp. D508–D512, 2009.

[93] I. Herraiz-Cardona, E. Ortega, and V. Pérez-Herranz, "Impedance study of hydrogen evolution on ni/zn and ni-co/zn stainless steel based electrodeposits," *Electrochimica Acta*, vol. 56, no. 3, pp. 1308–1315, 2011.

[94] I. Herraiz-Cardona, E. Ortega, L. Vázquez-Gómez, and V. Pérez-Herranz, "Double-template fabrication of three-dimensional porous nickel electrodes for hydrogen evolution reaction," *international journal of hydrogen energy*, vol. 37, no. 3, pp. 2147–2156, 2012.

[95] K. Koboski, E. Nelsen, and J. Hampton, "Hydrogen evolution reaction measurements of dealloyed porous nicu," *Nanoscale research letters*, vol. 8, no. 1, p. 528, 2013.

[96] P. Los, A. Lasia, H. Ménard, and L. Brossard, "Impedance studies of porous lanthanum-phosphate-bonded nickel electrodes in concentrated sodium hydroxide solution," *Journal of Electroanalytical Chemistry*, vol. 360, no. 1-2, pp. 101–118, 1993.

[97] H. Ju, Z. Li, and Y. Xu, "Electro-catalytic activity of ni-co-based catalysts for oxygen evolution reaction," *Materials Research Bulletin*, vol. 64, pp. 171–174, 2015.

[98] M. Lyons and M. Brandon, "The oxygen evolution reaction on passive oxide covered transition metal electrodes in aqueous alkaline solution. part 1-nickel," *Int. J. Electrochem. Sci*, vol. 3, no. 12, pp. 1386–1424, 2008.

[99] M. Kibria and M. Mridha, "Electrochemical studies of the nickel electrode for the oxygen evolution reaction," *International journal of hydrogen energy*, vol. 21, no. 3, pp. 179–182, 1996.

[100] D. Bediako, Y. Surendranath, and D. Nocera, "Mechanistic studies of the oxygen evolution reaction mediated by a nickel-borate thin film electrocatalyst," *Journal of the American Chemical Society*, vol. 135, no. 9, pp. 3662–3674, 2013.

[101] I. Mouton, T. Printemps, A. Grenier, N. Gambacorti, E. Pinna, M. Tiddia, A. Vacca, and G. Mula, "Toward an accurate quantification in atom probe tomography reconstruction by correlative electron tomography approach on nanoporous materials," *Ultramicroscopy*, vol. 182, pp. 112–117, 2017.

[102] G. Mula, E. Pinna, M. Mehrabanian, E. Riva, and E. Cara, "Electrochemical nanolithography," 2018. IT Patent application n. 102,018,000,003,427.

[103] A. Pezzella, M. Barra, A. Musto, A. Navarra, M. Alfe, P. Manini, S. Parisi, A. Cassinese, V. Criscuolo, and M. d'Ischia, "Stem cell-compatible eumelanin biointerface fabricated by chemically controlled solid state polymerization," *Materials Horizons*, vol. 2, no. 2, pp. 212–220, 2015.

[104] T. Printemps, G. Mula, D. Sette, P. Bleuet, V. Delaye, N. Bernier, A. Grenier, G. Audoit, N. Gambacorti, and L. Hervé, "Self-adapting denoising, alignment and reconstruction in electron tomography in materials science," *Ultramicroscopy*, vol. 160, pp. 23–34, 2016.

[105] T. Printemps, N. Bernier, P. Bleuet, G. Mula, and L. Herve, "Non-rigid alignment in electron tomography in materials science," *Journal of microscopy*, vol. 263, no. 3, pp. 312–319, 2016.

[106] G. Mula, L. Manca, S. Setzu, and A. Pezzella, "Photovoltaic properties of psi impregnated with eumelanin," *Nanoscale research letters*, vol. 7, no. 1, p. 377, 2012.

[107] A. Pinna, F. Simbula, D. Marongiu, A. Pezzella, M. d'Ischia, and G. Mula, "Boosting, probing and switching-off visible light-induced photocurrents in eumelanin-porous silicon hybrids," *Rsc Advances*, vol. 5, no. 70, pp. 56704–56710, 2015.

[108] S. Schricker, "Composite resin polymerization and relevant parameters," in *Orthodontic Applications of Biomaterials*, pp. 153–170, Elsevier, 2017.

[109] S. Jo, J. Lee, M. Sim, M. Kim, J. Park, Y. Choi, Y. Kim, S. Ihn, and K. Cho, "High performance organic photovoltaic cells using polymer-hybridized ZnO nanocrystals as a cathode interlayer," *Advanced Energy Materials*, vol. 1, no. 4, pp. 690–698, 2011.

[110] J. He, P. Gao, Z. Ling, L. Ding, Z. Yang, J. Ye, and Y. Cui, "High-efficiency silicon/organic heterojunction solar cells with improved junction quality and interface passivation," *ACS nano*, vol. 10, no. 12, pp. 11525–11531, 2016.

[111] J. Sheng, K. Fan, D. Wang, C. Han, J. Fang, P. Gao, and J. Ye, "Improvement of the SiO_x passivation layer for high-efficiency si/pedot: Pss heterojunction solar cells," *ACS applied materials & interfaces*, vol. 6, no. 18, pp. 16027–16034, 2014.

[112] Y. Jia, A. Cao, F. Kang, P. Li, X. Gui, L. Zhang, E. Shi, J. Wei, K. Wang, H. Zhu, *et al.*, "Strong and reversible modulation of carbon nanotube-silicon heterojunction solar cells by an interfacial oxide layer," *Physical Chemistry Chemical Physics*, vol. 14, no. 23, pp. 8391–8396, 2012.

[113] F. Wang, D. Kozawa, Y. Miyauchi, K. Hiraoka, S. Mouri, Y. Ohno, and K. Matsuda, "Considerably improved photovoltaic performance of carbon nanotube-based solar cells using metal oxide layers," *Nature communications*, vol. 6, p. 6305, 2015.

[114] S. Matta, K. Kakiage, S. Makuta, A. Veamatahau, Y. Aoyama, T. Yano, M. Hanaya, and Y. Tachibana, "Dye-anchoring functional groups on the

performance of dye-sensitized solar cells: comparison between alkoxysilyl and carboxyl groups," *The Journal of Physical Chemistry C*, vol. 118, no. 49, pp. 28425–28434, 2014.

[115] S. Sharma, S. Wagh, and R. Govindarajan, "Melanosomal proteins-role in melanin polymerization," *Pigment cell research*, vol. 15, no. 2, pp. 127–133, 2002.

[116] K. Ju, Y. Lee, S. Lee, S. Park, and J. Lee, "Bioinspired polymerization of dopamine to generate melanin-like nanoparticles having an excellent free-radical-scavenging property," *Biomacromolecules*, vol. 12, no. 3, pp. 625–632, 2011.

[117] R. Sarangarajan and S. Apte, "The polymerization of melanin: a poorly understood phenomenon with egregious biological implications," *Melanoma research*, vol. 16, no. 1, pp. 3–10, 2006.

[118] A. Chakraborty, J. Platt, K. Kim, B. Se Kwon, D. Bennett, and J. Pawelek, "Polymerization of 5,6-dihydroxyindole-2-carboxylic acid to melanin by the pmel 17/silver locus protein," *European journal of biochemistry*, vol. 236, no. 1, pp. 180–188, 1996.

[119] M. d'Ischia, A. Napolitano, and G. Prota, "Peroxidase as an alternative to tyrosinase in the oxidative polymerization of 5,6-dihydroxyindoles to melanin (s)," *Biochimica et Biophysica Acta (BBA)-General Subjects*, vol. 1073, no. 2, pp. 423–430, 1991.

[120] R. Micillo, L. Panzella, M. Iacomino, G. Prampolini, I. Cacelli, A. Ferretti, O. Crescenzi, K. Koike, A. Napolitano, and M. d'Ischia, "Eumelanin broadband absorption develops from aggregation-modulated chromophore interactions under structural and redox control," *Scientific reports*, vol. 7, p. 41532, 2017.

[121] M. d'Ischia, A. Napolitano, V. Ball, C. Chen, and M. Buehler, "Polydopamine and eumelanin: from structure-property relationships to a unified tailoring strategy," *Accounts of chemical research*, vol. 47, no. 12, pp. 3541–3550, 2014.

[122] M. d'Ischia, A. Napolitano, A. Pezzella, P. Meredith, and T. Sarna, "Chemical and structural diversity in eumelanins: unexplored bio-optoelectronic materials," *Angewandte Chemie International Edition*, vol. 48, no. 22, pp. 3914–3921, 2009.

[123] G. Zonios, A. Dimou, I. Bassukas, D. Galaris, A. Tsolakidis, and E. Kaxiras, "Melanin absorption spectroscopy: new method for noninvasive skin investigation and melanoma detection," *Journal of biomedical optics*, vol. 13, no. 1, p. 014017, 2008.

[124] J. Perdew, K. Burke, and M. Ernzerhof, "Generalized gradient approximation made simple," *Physical review letters*, vol. 77, no. 18, p. 3865, 1996.

[125] J. Perdew, K. Burke, and M. Ernzerhof, "Perdew, burke, and ernzerhof reply," *Physical Review Letters*, vol. 80, no. 4, p. 891, 1998.

[126] E. Kaxiras, A. Tsolakidis, G. Zonios, and S. Meng, "Structural model of eumelanin," *Physical review letters*, vol. 97, no. 21, p. 218102, 2006.

[127] S. Meng and E. Kaxiras, "Theoretical models of eumelanin protomolecule and its photoprotection mechanism," *Biophysical Journal*, vol. 96, no. 3, p. 300a, 2009.

[128] L. Panzella, G. Gentile, G. D'Errico, N. Della Vecchia, M. Errico, A. Napolitano, C. Carfagna, and M. d'Ischia, "Atypical structural and π-electron features of a melanin polymer that lead to superior free-radical-scavenging properties," *Angewandte Chemie International Edition*, vol. 52, no. 48, pp. 12684–12687, 2013.

[129] C. Bettinger, J. Bruggeman, A. Misra, J. Borenstein, and R. Langer, "Biocompatibility of biodegradable semiconducting melanin films for nerve tissue engineering," *Biomaterials*, vol. 30, no. 17, pp. 3050–3057, 2009.

[130] J. Munoz-Munoz, F. García-Molina, R. Varón, J. Tudela, F. García-Cánovas, and J. Rodríguez-López, "Generation of hydrogen peroxide

in the melanin biosynthesis pathway," *Biochimica et Biophysica Acta (BBA)-Proteins and Proteomics*, vol. 1794, no. 7, pp. 1017–1029, 2009.

[131] W. Korytowski, B. Pilas, T. Sarna, and B. Kalyanaraman, "Photoinduced generation of hydrogen peroxide and hydroxyl radicals in melanins," *Photochemistry and photobiology*, vol. 45, no. 2, pp. 185–190, 1987.

[132] P. Granitzer and K. Rumpf, "Porous silicon—a versatile host material," *Materials*, vol. 3, no. 2, pp. 943–998, 2010.

[133] P. Tiberto, G. Barrera, L. Boarino, F. Celegato, M. Coïsson, N. De Leo, F. Albertini, F. Casoli, and P. Ranzieri, "Arrays of ordered nanostructures in fe-pt thin films by self-assembling of polystyrene nanospheres," *Journal of Applied Physics*, vol. 113, no. 17, p. 17B516, 2013.

[134] C. Bates, M. Maher, D. Janes, C. Ellison, and C. Willson, "Block copolymer lithography," *Macromolecules*, vol. 47, no. 1, pp. 2–12, 2013.

[135] X. Li, "Metal assisted chemical etching for high aspect ratio nanostructures: A review of characteristics and applications in photovoltaics," *Current Opinion in Solid State and Materials Science*, vol. 16, no. 2, pp. 71–81, 2012.

[136] V. Gianneta, A. Olziersky, and A. Nassiopoulou, "Si nanopatterning by reactive ion etching through an on-chip self-assembled porous anodic alumina mask," *Nanoscale research letters*, vol. 8, no. 1, p. 71, 2013.

[137] J. Yeom, Y. Wu, J. Selby, and M. Shannon, "Maximum achievable aspect ratio in deep reactive ion etching of silicon due to aspect ratio dependent transport and the microloading effect," *Journal of Vacuum Science & Technology B: Microelectronics and Nanometer Structures Processing, Measurement, and Phenomena*, vol. 23, no. 6, pp. 2319–2329, 2005.

[138] Y. Tang, A. Sandoughsaz, K. Owen, and K. Najafi, "Ultra deep reactive ion etching of high aspect-ratio and thick silicon using a ramped-

parameter process," *Journal of Microelectromechanical Systems*, vol. 27, no. 4, pp. 686–697, 2018.

[139] B. Miao, J. Zhang, X. Ding, D. Wu, Y. Wu, W. Lu, and J. Li, "Improved metal assisted chemical etching method for uniform, vertical and deep silicon structure," *Journal of Micromechanics and Microengineering*, vol. 27, no. 5, p. 055019, 2017.

[140] C. Lévy-Clément, "Porous silicon formation by metal nanoparticle-assisted etching," *Handbook of Porous Silicon*, pp. 49–66, 2014.

[141] H. Namatsu, M. Oda, A. Yokoo, M. Fukuda, K. Irisa, S. Tsurumi, and K. Komatsu, "Chemical nanoimprint lithography for step-and-repeat si patterning," *Journal of Vacuum Science & Technology B: Microelectronics and Nanometer Structures Processing, Measurement, and Phenomena*, vol. 25, no. 6, pp. 2321–2324, 2007.

[142] S. Chu, S. Inoue, K. Wada, S. Hishita, and K. Kurashima, "A new electrochemical lithography fabrication of self-organized titania nanostructures on glass by combined anodization," *Journal of The Electrochemical Society*, vol. 152, no. 3, pp. B116–B124, 2005.

[143] G. Barillaro and L. Strambini, "Controlling macropore formation in patterned n-type silicon: existence of a pitch-dependent etching current density lower bound," *Electrochemistry Communications*, vol. 12, no. 10, pp. 1314–1317, 2010.

[144] E. Pinna, M. Mehrabanian, E. Redolfi Riva, E. Cara, G. Aprile, L. Boarino, and G. Mula, "Electrochemical nanolithography on silicon: an easy and scalable method to control pore formation at the nanoscale," *Materials*, vol. 12, no. 18, p. 2891, 2019.

[145] G. Macias, J. Ferré-Borrull, J. Pallarès, and L. Marsal, "Effect of pore diameter in nanoporous anodic alumina optical biosensors," *Analyst*, vol. 140, no. 14, pp. 4848–4854, 2015.

[146] S. Gao, Y. Wang, X. Diao, G. Luo, and Y. Dai, "Effect of pore diameter and cross-linking method on the immobilization efficiency of candida rugosa lipase in sba-15," *Bioresource technology*, vol. 101, no. 11, pp. 3830–3837, 2010.

[147] S. Srivastava, D. Kumar, P. Singh, M. Kar, V. Kumar, and M. Husain, "Excellent antireflection properties of vertical silicon nanowire arrays," *Solar Energy Materials and Solar Cells*, vol. 94, no. 9, pp. 1506–1511, 2010.

[148] T. Yang, T. Huang, H. Lee, T. Lin, and T. Yen, "Applying silicon nanoholes with excellent antireflection for enhancing photovoltaic performance," *Journal of The Electrochemical Society*, vol. 159, no. 2, pp. B104–B108, 2011.

[149] X. Li, J. Li, T. Chen, B. Tay, J. Wang, and H. Yu, "Periodically aligned si nanopillar arrays as efficient antireflection layers for solar cell applications," *Nanoscale research letters*, vol. 5, no. 11, p. 1721, 2010.

[150] V. Iyengar, B. Nayak, and M. Gupta, "Optical properties of silicon light trapping structures for photovoltaics," *Solar Energy Materials and Solar Cells*, vol. 94, no. 12, pp. 2251–2257, 2010.

[151] C. Sun, P. Jiang, and B. Jiang, "Broadband moth-eye antireflection coatings on silicon," *Applied Physics Letters*, vol. 92, no. 6, p. 061112, 2008.

[152] M. Schubert, F. Mont, S. Chhajed, D. Poxson, J. Kim, and E. Schubert, "Design of multilayer antireflection coatings made from co-sputtered and low-refractive-index materials by genetic algorithm," *Optics express*, vol. 16, no. 8, pp. 5290–5298, 2008.

[153] S. Strehlke, S. Bastide, J. Guillet, and C. Levy-Clement, "Design of porous silicon antireflection coatings for silicon solar cells," *Materials Science and Engineering: B*, vol. 69, pp. 81–86, 2000.

[154] L. Remache, E. Fourmond, A. Mahdjoub, J. Dupuis, and M. Lemiti, "Design of porous silicon/pecvd SiO_x antireflection coatings for silicon solar cells," *Materials Science and Engineering: B*, vol. 176, no. 1, pp. 45–48, 2011.

[155] J. Selj, A. Thøgersen, S. Foss, and E. Marstein, "Optimization of multilayer porous silicon antireflection coatings for silicon solar cells," *Journal of Applied Physics*, vol. 107, no. 7, p. 074904, 2010.

[156] G. Masini, L. Colace, and G. Assanto, "Si based optoelectronics for communications," *Materials Science and Engineering: B*, vol. 89, no. 1-3, pp. 2–9, 2002.

[157] L. Khriachtchev, *Silicon nanophotonics: basic principles, current status and perspectives*. Jenny Stanford Publishing, 2016.

[158] D. Lockwood and L. Pavesi, "Silicon fundamentals for photonics applications," in *Silicon Photonics*, pp. 1–50, Springer, 2004.

[159] G. Reed and A. Kewell, "Erbium-doped silicon and porous silicon for optoelectronics," *Materials Science and Engineering: B*, vol. 40, no. 2-3, pp. 207–215, 1996.

[160] V. Bondarenko, N. Vorozov, L. Dolgii, A. Dorofeev, N. Kazyuchits, A. Leshok, and G. Troyanova, "Luminescence of erbium-doped porous silicon," *Technical Physics Letters*, vol. 23, no. 1, pp. 3–4, 1997.

[161] E. Marstein, J. Skjelnes, and T. Finstad, "Incorporation of erbium in porous silicon," *Physica Scripta*, vol. 2002, no. T101, p. 103, 2002.

[162] A. Kenyon, "Quantum confinement in rare-earth doped semiconductor systems," *Current Opinion in Solid State and Materials Science*, vol. 7, no. 2, pp. 143–149, 2003.

[163] A. Kenyon, "Erbium in silicon," *Semiconductor Science and Technology*, vol. 20, no. 12, p. R65, 2005.

[164] A. Najar, N. Lorrain, H. Ajlani, J. Charrier, M. Oueslati, and L. Haji, "Er^{3+} doping conditions of planar porous silicon waveguides," *Applied Surface Science*, vol. 256, no. 3, pp. 581–586, 2009.

[165] S. Sokolov, R. Rösslhuber, D. Zhigunov, N. Latukhina, and V. Timoshenko, "Photoluminescence of rare earth ions (Er^{3+}, Yb^{3+}) in a porous silicon matrix," *Thin Solid Films*, vol. 562, pp. 462–466, 2014.

[166] D. Goff, *Fiber optic reference guide*. Routledge, 2002.

[167] L. Fortes, M. Gonçalves, J. Pereira, and F. d'Acapito, "Exafs study of Er, Yb doped hollow and dense SiO_2 microspheres," *Journal of Non-Crystalline Solids*, vol. 402, pp. 244–251, 2014.

[168] P. Kik, M. De Dood, K. Kikoin, and A. Polman, "Excitation and deexcitation of Er^{3+} in crystalline silicon," *Applied physics letters*, vol. 70, no. 13, pp. 1721–1723, 1997.

[169] D. Adler, D. Jacobson, D. Eaglesham, M. Marcus, J. Benton, J. Poate, and P. Citrin, "Local structure of 1.54-μm-luminescence Er^{3+} implanted in Si," *Applied physics letters*, vol. 61, no. 18, pp. 2181–2183, 1992.

[170] L. Pavesi, L. Dal Negro, C. Mazzoleni, G. Franzo, and d. F. Priolo, "Optical gain in silicon nanocrystals," *Nature*, vol. 408, no. 6811, p. 440, 2000.

[171] S. Gaponenko, L. Pavesi, and L. Dal Negro, *Towards the first silicon laser*. Kluwer Academic Publishers, 2003.

[172] L. Luo, X. Zhang, K. Li, K. Cheah, M. Gong, J. Shi, and W. Wong, "Strong near-infrared photoluminescence in erbium/ytterbium codoped porous silicon," *Applied Physics Letters*, vol. 86, no. 21, p. 212505, 2005.

[173] A. Najar, J. Charrier, N. Lorrain, L. Haji, and M. Oueslati, "Optical gain measurements in porous silicon planar waveguides codoped by erbium and ytterbium ions at 1.53 μm," *Applied Physics Letters*, vol. 91, no. 12, p. 121120, 2007.

[174] M. Miritello, R. Savio, M. Galli, A. Irrera, F. Iacona, G. Franzò, L. Andreani, L. O'Faolain, T. Krauss, and F. Priolo, "Er doped-si nanostructures coupled with photonic crystals for high enhancement of light extraction," *ECS Transactions*, vol. 53, no. 4, pp. 71–80, 2013.

[175] E. Talbot, R. Lardé, P. Pareige, L. Khomenkova, K. Hijazi, and F. Gourbilleau, "Nanoscale evidence of erbium clustering in er-doped silicon-rich silica," *Nanoscale research letters*, vol. 8, no. 1, p. 39, 2013.

[176] J. Ramírez, F. Ferrarese Lupi, Y. Berencén, A. Anopchenko, J. Colonna, O. Jambois, J. Fedeli, L. Pavesi, N. Prtljaga, P. Rivallin, *et al.*, "Er-doped light emitting slot waveguides monolithically integrated in a silicon photonic chip," *Nanotechnology*, vol. 24, no. 11, p. 115202, 2013.

[177] F. Priolo, T. Gregorkiewicz, M. Galli, and T. Krauss, "Silicon nanostructures for photonics and photovoltaics," *Nature nanotechnology*, vol. 9, no. 1, p. 19, 2014.

[178] Y. Lu, C. Huang, J. Cheng, and A. Larsen, "High Er^{3+} luminescent efficiency in Er-doped SiO_x films containing amorphous Si nanodots," *Journal of Alloys and Compounds*, vol. 676, pp. 428–431, 2016.

[179] L. Jin, D. Li, L. Xiang, F. Wang, D. Yang, and D. Que, "Energy transfer from luminescent centers to Er^{3+} in erbium-doped silicon-rich oxide films," *Nanoscale research letters*, vol. 8, no. 1, p. 366, 2013.

[180] L. Rebohle, Y. Berencén, R. Wutzler, M. Braun, D. Hiller, J. Ramírez, B. Garrido, M. Helm, and W. Skorupa, "The electroluminescence mechanism of Er^{3+} in different silicon oxide and silicon nitride environments," *Journal of Applied Physics*, vol. 116, no. 12, p. 123104, 2014.

[181] L. Rebohle, Y. Berencén, M. Braun, B. Garrido, D. Hiller, B. Liu, J. Ramírez, J. Sun, R. Wutzler, M. Helm, *et al.*, "Rare earth doped metal-oxide-semiconductor structures: a promising material system or a dead end of optoelectronic evolution?," *ECS Transactions*, vol. 61, no. 5, pp. 175–185, 2014.

[182] A. Polman, G. Van den Hoven, J. Custer, J. Shin, R. Serna, and P. Alkemade, "Erbium in crystal silicon: optical activation, excitation, and concentration limits," *Journal of applied physics*, vol. 77, no. 3, pp. 1256–1262, 1995.

[183] A. Polman, "Erbium implanted thin film photonic materials," *Journal of applied physics*, vol. 82, no. 1, pp. 1–39, 1997.

[184] A. Kenyon, "Recent developments in rare-earth doped materials for optoelectronics," *Progress in Quantum Electronics*, vol. 26, no. 4-5, pp. 225–284, 2002.

[185] Y. Zhou, P. Snow, and P. Russell, "Strong modification of photoluminescence in erbium-doped porous silicon microcavities," *Applied Physics Letters*, vol. 77, no. 16, pp. 2440–2442, 2000.

[186] M. Miritello, R. Lo Savio, A. Piro, G. Franzò, F. Priolo, F. Iacona, and C. Bongiorno, "Optical and structural properties of Er_2O_3 films grown by magnetron sputtering," *Journal of applied physics*, vol. 100, no. 1, p. 013502, 2006.

[187] M. Miritello, R. Lo Savio, F. Iacona, G. Franzò, A. Irrera, A. Piro, C. Bongiorno, and F. Priolo, "Efficient luminescence and energy transfer in erbium silicate thin films," *Advanced Materials*, vol. 19, no. 12, pp. 1582–1588, 2007.

[188] J. Salonen, E. Mäkilä, J. Riikonen, T. Heikkilä, and V.-P. Lehto, "Controlled enlargement of pores by annealing of porous silicon," *Physica status solid (a)*, vol. 206, no. 6, pp. 1313–1317, 2009.

[189] K. Rumpf, P. Granitzer, P. Pölt, and M. Reissner, "Specific loading of porous silicon with iron oxide nanoparticles to achieve different blocking temperatures," *Thin Solid Films*, vol. 543, pp. 56–58, 2013.

[190] K. Rumpf, P. Granitzer, G. Hilscher, M. Albu, and P. Poelt, "Magnetically interacting low dimensional ni-nanostructures within porous silicon," *Microelectronic engineering*, vol. 90, pp. 83–87, 2012.

[191] P. Bas, A. Bostel, B. Deconihout, and D. Blavette, "A general protocol for the reconstruction of 3d atom probe data," *Applied Surface Science*, vol. 87, pp. 298–304, 1995.

[192] B. Gault, F. De Geuser, L. Stephenson, M. Moody, B. Muddle, and S. Ringer, "Estimation of the reconstruction parameters for atom probe tomography," *Microscopy and Microanalysis*, vol. 14, no. 4, pp. 296–305, 2008.

[193] E. Marquis, B. Geiser, T. Prosa, and D. Larson, "Evolution of tip shape during field evaporation of complex multilayer structures," *Journal of microscopy*, vol. 241, no. 3, pp. 225–233, 2011.

[194] C. Oberdorfer, S. Eich, and G. Schmitz, "A full-scale simulation approach for atom probe tomography," *Ultramicroscopy*, vol. 128, pp. 55–67, 2013.

[195] B. Pfeiffer, T. Erichsen, E. Epler, C. Volkert, P. Trompenaars, and C. Nowak, "Characterization of nanoporous materials with atom probe tomography," *Microscopy and Microanalysis*, vol. 21, no. 3, pp. 557–563, 2015.

[196] C. Barroo, N. Janvelyan, B. Zugic, J. Biener, A. Akey, C. Friend, and D. Bell, "The importance of nano-confinement in nanoporous catalysts: atom probe tomography and fib/sem study of surface segregation," in *European Microscopy Congress 2016: Proceedings*, pp. 906–907, Wiley Online Library, 2016.

[197] D. Haley, T. Petersen, S. Ringer, and G. Smith, "Atom probe trajectory mapping using experimental tip shape measurements," *Journal of microscopy*, vol. 244, no. 2, pp. 170–180, 2011.

[198] P. Felfer and J. Cairney, "A computational geometry framework for the optimisation of atom probe reconstructions," *Ultramicroscopy*, vol. 169, pp. 62–68, 2016.

[199] F. De Geuser, W. Lefebvre, F. Danoix, F. Vurpillot, B. Forbord, and D. Blavette, "An improved reconstruction procedure for the correction

of local magnification effects in three-dimensional atom-probe," *Surface and Interface Analysis*, vol. 39, no. 2-3, pp. 268–272, 2007.

[200] F. Vurpillot, M. Gruber, G. Da Costa, I. Martin, L. Renaud, and A. Bostel, "Pragmatic reconstruction methods in atom probe tomography," *Ultramicroscopy*, vol. 111, no. 8, pp. 1286–1294, 2011.

[201] W. Lefebvre, D. Hernandez-Maldonado, F. Moyon, F. Cuvilly, C. Vaudolon, D. Shinde, and F. Vurpillot, "Haadf-stem atom counting in atom probe tomography specimens: towards quantitative correlative microscopy," *Ultramicroscopy*, vol. 159, pp. 403–412, 2015.

[202] M. Herbig, P. Choi, and D. Raabe, "Combining structural and chemical information at the nanometer scale by correlative transmission electron microscopy and atom probe tomography," *Ultramicroscopy*, vol. 153, pp. 32–39, 2015.

[203] I. Arslan, E. Marquis, M. Homer, M. Hekmaty, and N. Bartelt, "Towards better 3-d reconstructions by combining electron tomography and atom-probe tomography," *Ultramicroscopy*, vol. 108, no. 12, pp. 1579–1585, 2008.

[204] P. Midgley and M. Weyland, "3d electron microscopy in the physical sciences: the development of z-contrast and eftem tomography," *Ultramicroscopy*, vol. 96, no. 3-4, pp. 413–431, 2003.

[205] K. Thompson, D. Lawrence, D. Larson, J. Olson, T. Kelly, and B. Gorman, "In situ site-specific specimen preparation for atom probe tomography," *Ultramicroscopy*, vol. 107, no. 2-3, pp. 131–139, 2007.

[206] W. Lefebvre, F. Vurpillot, and X. Sauvage, *Atom probe tomography: put theory into practice*. Academic Press, 2016.

Acknowledgements

This thesis has been carried out mostly at the Università degli Studi di Cagliari, in the PoroSiLab of the Physics department, under the supervision of Dr. Guido Mula. The research activity has been supported by RAS-Regione Autonoma della Sardegna (P.O.R. F.S.E. 2014-2020). Any part of this work is original and it has not been previously used for a thesis or a degree at this or any other university. I would like to acknowledge several people who were part of my everyday life and enriched my activity in the past three years:

- my supervisor Guido Mula, for having guided my professional and scientific growth, helping me to overcome my limits and my insecurities (that are many, but were even more some years ago);
- my supervisors during my periods abroad: Stéphane Bastide at CNRS and Nichola Spencer and Antonella Rossi at ETH. They have been a guide in my process of learning, leaving me the right independence to explore new aspects of my research. I cannot forget to thank also other people that have been fundamental in those periods: Encarni, Asma, Atim, Tohru, Jean Claude, Laura and Maria Giovanna for being my family during the beautiful period in Paris; all the LSST and ISA groups, but especially Efisio and Dodo for all the help and the company they offered me when in Zürich.
- my colleagues at PoroSiLab: Tiddy for the many years spent chatting and etching silicon always being careful to not find any drop of HF on our gloves; Eugenio and Mehran for the support, hints, advice during

the hardest year of my PhD; least but not last, Elisa and Simona from DIMCM.

- all the colleagues that I have met during the years spent studying physics: the "old ones" Stori, Ardu and Collu, who have been bearing my crazyness for more than ten years, and all the "new ones" that have been a constant presence during everyday lunches and coffee (or better ice-cream) breaks;

- a special thanks to Ele Cara for the precious scientific (and not) discussions especially through vocal messages, for being one of the best discoveries of this PhD and for the very dense one-day LateX lesson that allowed me to save months of hard work.

To be more professional I did not put them at the beginning of the page, but at the very top of my ancknowledgements list there should be Gabriele and my family. They were by my side every single moment, they shared with me all the successes and failures, they gave me the force to continue when I was about to give up, they helped me to find solutions when I was in trouble or doubt and they are my strongest fans. Without them I could not be the person I am, so I will not stop to say thank you to all of them.